Finite-size Anisotropic Particles in Two-dimensional Turbulent Flows

Jia Yang

A thesis submitted for the degree of

Doctor of Philosophy

of The Australian National University

Supervisory Panel:

Doctor Hua Xia, chair

Professor Michael Shats

Doctor Horst Punzmann

Doctor Nicolas Francois

Declaration

This thesis contains no material which has been accepted for the award of any degree or diploma in any university. To the best of the author's knowledge and belief, it contains no material previously published or written by another person, except where due reference is made in the text.

Jia Yang

27 January 2021

Acknowledgments

To begin, I would like to thank my supervisors, Dr Hua Xia and Prof Michael Shats, for taking me on as a PhD student. Their immense knowledge, motivation and patience have given me the power to excel in my research. Without their consistent support and guidance, this thesis would have been impossible to complete.

My sincere thanks also go to Dr Horst Punzmann and Dr Nicolas Francois for their valuable guidance, encouragement and insightful comments that have helped me in both my academic work and my daily life. Your assistance enabled me to concentrate on my research and brought my work to a higher level.

In addition, my gratitude goes to my lab mates in the Physics of Fluids Group: Jean-Baptiste Gorce, Mahdi Davoodianidalik, Dr Sunny (Sung Ha) Hong, and many students and faculty members in the Research School of Physics for their useful discussions and collaborations throughout my PhD journey. They are my most valuable friends.

Last but not least, I wish to give my greatest acknowledgements to my partner Yaxi Shen, for her endless encouragement during my bad times; to my parents Xianbo Yang and Yanmin Yang, for their all their support; and finally, to my fluffy friends, the Cavalier King Charles Spaniel 'Crab' and the Pomsky 'Nomi' for their companionship.

Abstract

Finite-size Anisotropic Particles in Two-dimensional Turbulent Flows

Dispersion in chaotic flows characterises the mechanisms of the transport of mass, heat or momentum in a fluid. It is related to random and chaotic time-dependent fluid motion. Dispersion of particles in fluids governs numerous processes in nature and in industrial flows, where particles vary in size and shape. This is a significant physics problem in which it is necessary to account for the interactions between particles and the structure of the flow. The main aim of this thesis is to study the dispersion of finite-size anisotropic particles in two-dimensional turbulent flows. This work focuses on the coupling between translational and rotational motion of finite-size particles, as well as on the impact of the inhomogeneity of turbulence on the particle motion.

By analysing the dispersion of ellipsoidal particles in 2D turbulence, we find that particles have preferential directions of motion, either transversely (perpendicular to the major axis) or longitudinally (along the major axis). This preferred direction can be changed by altering the ratio of the size of the ellipsoidal particle and the forcing scale of the underlying 2D turbulence. These features of the turbulent transport of ellipsoids are attributed here to the interaction of these anisotropic objects with the structure of 2D turbulent flows made of meandering coherent bundles. Large ellipsoids interact with many bundles and thus diffuse faster in the direction parallel to their major axes, a behavior reminiscent of the dynamics of an ellipsoid undergoing a Brownian motion. By contrast, small ellipsoids diffuse faster in the direction transverse to their major axes. We demonstrate that the coupling between translational and rotational diffusion arises as a result of the advection of the small ellipsoid by a

single coherent bundle.

We also study the motion of floating discs with a cut-out sector in 2D turbulent flows. Such model anisotropic particles are suitable for capturing the essential features of their interaction with underlying turbulence. In particular, we find that the discs modify the surrounding flow by converting turbulent eddies into persistent bundles of fluid particles, causing the 'rectification' of the turbulent fluctuations and generating unidirectional propulsion of the discs. The randomisation of such a motion is caused by the turbulent rotation of the anisotropic particle. It is found that translational and rotational motion of particles are coupled. This coupling depends on the particle's shape and size relative to the characteristic scale of the underlying turbulence. We also show that such a coupling can be effectively controlled by engineering the shape and size of the anisotropic particle to match the characteristic scale of turbulence.

The results offer a novel method of engineering the dispersion of anisotropic particles in chaotic and turbulent flows. Our conclusion will provide better understanding of the motion of anisotropic particles in applications including pollutant dispersion in the atmosphere, the motion of ocean buoys, the drift of sea ice and may also help in clarifying the mechanisms behind the enhanced swimming abilities of some aquatic organisms.

Contents

List of Figures

Introduction

1.1 Brownian motion

The most fundamental example of dispersion in fluids is the Brownian motion in thermal baths. Such motion is characterised by very small scales and is heavily dampened by viscosity. Thus, thermal agitation is balanced by viscous dissipation, leading to equilibrium. The effects of inertia in thermal baths are usually neglected. This process is named after the botanist Robert Brown, who first described the phenomenon in 1827. In the early 1900s, Albert Einstein contributed to a theoretical understanding of Brownian motion. He explained that the motion of a Brownian particle was caused by a large number of random bombardments by the surrounding fluid molecules and predicted that its diffusive motion should be observable [25]. An experimental validation of Einstein's theory was conducted by Jean Baptiste Perrin as part of his Nobel Prize winning work, 'On the discontinuous structure of matter' [82].

Einstein's microscopic description assumes that the displacements ($\Delta x = x(t + \Delta t) - x(t)$) of a Brownian particle within a time interval (Δt). The probability density function (PDF) $f(x, t)$ of the particle follows the diffusion equation in the one-dimensional case (equation (1.1)):

$$\frac{\partial f(x, t)}{\partial t} = D \frac{\partial^2 f(x, t)}{\partial x^2} \tag{1.1}$$

where D is the diffusion coefficient.

If a Brownian particle starts from the origin at the initial time $t = 0$, the solution of equation (1.1) is a Gaussian distribution with zero mean and its variance equals to $2Dt$:

$$f(x, t) = \frac{1}{\sqrt{4\pi Dt}} e^{-\frac{x^2}{4Dt}}. \tag{1.2}$$

Accordingly, the mean-squared displacement (MSD, $\langle x(t)^2 \rangle$) of the particle, which is the second moment of the PDF, is a linear function of time, as follows:

$$\langle \Delta x(t)^2 \rangle = 2Dt, \tag{1.3}$$

where $\Delta x(t) = x(t) - x(0)$ and the brackets $\langle \rangle$ denote the ensemble average over the equilibrium distribution [27].

The Stokes-Einstein equation of the diffusion of spherical particles through a liquid with a low Reynolds number is related to the diffusion coefficient D, the fluid viscosity μ_f and the particle radius r [25], and is expressed as follows:

$$D = \frac{k_B T}{6\pi \mu_f r}, \tag{1.4}$$

where k_B is the Boltzmann's constant and T is the temperature. The concept of Brownian dynamics was further extended by Einstein to rotational and other degrees of freedom [26].

In the diffusion model, the inertia of the particle is neglected. As a result, an infinite force is required to change the velocity or direction of the particle discontinuously to achieve a random walk at each step. An effective mean velocity is calculated as $\langle u \rangle = \sqrt{\Delta x^2}/\Delta t = \sqrt{2D}/\sqrt{\Delta t}$. As Δt approaches 0, this effective velocity diverges and becomes unable to represent the real velocity of the particle [8].

A remedy for the unphysical feature of Einstein's model at the short time-scale was proposed by Paul Langevin based on Newton's second law of motion. In his formula, the inertia of the particle was taken into consideration [55]. The relation can be described as follows:

$$m_p \frac{d^2 x}{dt^2} = -\xi \frac{dx}{dt} + \tilde{F}(t),$$ (1.5)

where m_p is the of the particle, ξ is the friction coefficient and $\tilde{F}(t)$ is the random force describing the rapidly fluctuating interactions between the particle and water molecules. Equation (1.5) is also referred to as the Langevin equation.

For a Brownian particle starting from the origin, a generalised expression for the MSD over the whole time range can be derived based on equation (1.5), as follows:

$$\langle \Delta x^2(t) \rangle = \frac{2k_B T}{\xi} (t - \frac{m}{\xi} + \frac{m}{\xi} e^{-\xi t/m}).$$ (1.6)

Through this equation, two regimes of MSD with asymptotic limits can be identified: the short and the long time-scale regimes [8]. These two regimes are separated by a relaxation time $\tau_B = m_p / \xi$.

(1) When $t \ll \tau_B$ (short time-scale), it is in a diffusive regime, where

$$\langle \Delta x^2(t) \rangle = \frac{k_B T}{m_p} t^2.$$ (1.7)

(2) When $t \gg \tau_B$ (long time-scale), it falls in a ballistic regime, where

$$\langle \Delta x^2(t) \rangle = \frac{2k_B T}{\xi} t = 2Dt.$$ (1.8)

With the development of advanced optical techniques in the recent decades, the instantaneous velocity of a Brownian particle and a transition from the ballistic ($\langle \Delta x^2(t) \rangle$

$\sim t^2$) to the diffusive regime ($\langle \Delta x^2(t) \rangle \sim t$) in MSD have been observed in both gas and liquid [57, 51, 46]. When a Brownian particle is suspended in a gas, the density of a gas is much smaller than the density of the Brownian particle ($\rho_f \ll \rho_p$), so the inertia of the gas is neglected. The dynamics of Brownian particles in a gas at short time-scales are governed by the momentum relaxation time of the particle τ_p, $\tau_p = m_p/\zeta$, which is identical to τ_B. When the Brownian particle is suspended in a liquid, in addition to the inertia of the particle itself, the inertia of the surrounding liquid also has an impact on the Brownian motion. This hydrodynamic memory effect dominates the dynamics of the particle at short time-scales [58]. This memory effect of liquid is characterised by the relaxation time of the liquid τ_f, $\tau_f = r^2 \rho_f/\nu$, where r is the radius of the particle, ρ_f is the density of the fluid and ν is the viscosity of the fluid. The comparison of τ_p and τ_f illustrates the differences of Brownian motion in gas and liquid at short time-scales.

Apart from the Brownian motion at short time-scales, studies of anisotropic Brownian motion and Brownian motion in non-equilibrium systems have also been carried out [58]. For example, the Brownian motion of isolated ellipsoidal particles in water confined to two dimensions has been studied [42]. The results showed a transition from anisotropic diffusion along the symmetric axes of the particles at short time-scales to isotropic diffusion at long time-scales. The differences in the diffusive coefficients at short-time scales is caused by the dissipative coupling between the translational and rotational motion. The study was further extended to non-equilibrium active suspensions, such as bacterial flows [79]. With the increase of bacterial concentration, the preferential diffusing direction of the ellipsoidal particles changed from the longitudinal axes to the transverse axes, which was attributed to the generic straining flow of swimming bacteria.

Brownian motion has played a central role in the development of both the foundations of thermodynamics and the dynamic interpretation of statistical physics. The subsequent study of Brownian motion and its generalisations has had a profound impact on physics, mathematics, chemistry, and biology [42], through applications including the generation of Brownian motors [43] and self-propelled particles [86].

1.2   Dispersion in turbulence

Dispersion in turbulence is one of the most enduring problems in hydrodynamics [69]. It describes the transport of mass, heat, or momentum within a system due to random and chaotic time-dependent motions. The dispersion process occurs when turbulent fluid systems reach critical conditions in response to shear flow, which results from a combination of steep concentration gradients, density gradients, and high velocities [62].

Turbulence is a state of a physical system with many degrees of freedom that deviates strongly from equilibrium. Although the governing equation of fluid motion in turbulence, the Navier-Stokes equation, has been known for more than a century, the nonlinearity makes it difficult to solve except for very few cases at low Reynolds numbers. The description of turbulent dispersion is even more complicated, since (1) it requires the knowledge of the characteristics of turbulent flows and the dynamics of different particles in the specific flow conditions, and (2) the Lagrangian frame of reference is required. Compared to the Eulerian statistics, Lagrangian statistics are more difficult to obtain both computationally and theoretically.

A fluid particle is often considered as an infinitesimal volume of a fluid element. Taylor was the first to study the dispersion of fluid particles in homogeneous stationary flows [99].

A sample trajectory of a fluid particle is shown in Figure 1.1. The mean-squared displacement of the particle ($\langle \Delta X^2 \rangle$) over a time interval ($\Delta t = t - t_0$) can be written as:

$$\frac{\partial}{\partial t}\langle \Delta X^2 \rangle = 2u(t) \cdot \int_{t_0}^{t} u(s)ds. \tag{1.9}$$
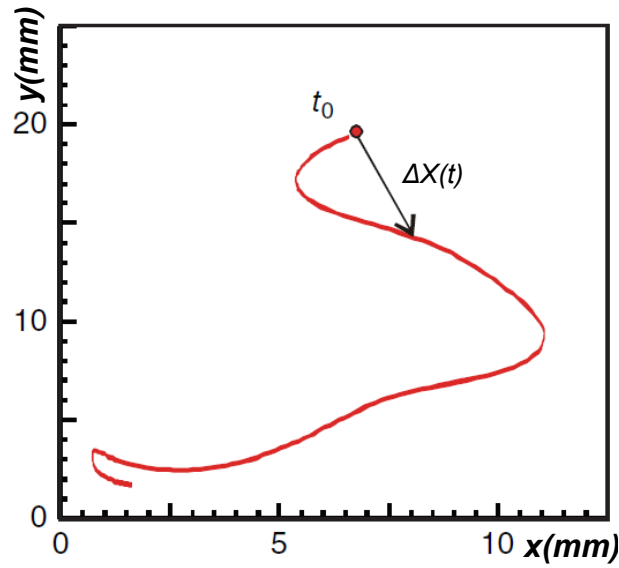
Figure 1.1: A sample trajectory of a fluid particle in fluid flow. The displacement of the particle within a time interval (t - t_0) is shown as $\Delta X(t)$

where the brackets $\langle\rangle$ denote statistical averaging, while u is the velocity of the fluid particle.

Assuming that the mean velocity $\langle u \rangle$ is zero, the second moment of the single particle displacement is expressed as:

$$\frac{\partial}{\partial t}\langle \Delta X^2 \rangle = 2\int_{t_0}^{t}\langle u(t_0)u(s)\rangle ds. \tag{1.10}$$

The behaviour of $\langle \Delta X^2 \rangle$ is dependent on the temporal correlation $\langle u(t_0)u(t)\rangle$ of the Lagrangian velocity $u(t)$. The corresponding characteristic time (Lagrangian velocity correlation time) can be computed as:

$$T_L = \int_{t_0}^{\infty} \rho_L(t)dt = \frac{1}{\langle u^2 \rangle}\int_{t_0}^{\infty}\langle u(t_0)u(t)\rangle dt \tag{1.11}$$

where $\langle u^2 \rangle$ is the variance of the velocity fluctuations, while $\rho(t)$ is the Lagrangian velocity autocorrelation function (ACF). The value of T_L provides a measure of the Lagrangian velocity memory.

Two limiting conditions are considered in Taylor's dispersion [69]: (1) When the observation time is longer than T_L ($t \gg T_L$), the MSD of particles is given by:

$$\langle \Delta X^2(t) \rangle = 2\langle u^2 \rangle T_L t. \tag{1.12}$$

(2) When the observation time is much shorter than T_L ($t \ll T_L$), the MSD is given by:

$$\langle \Delta X^2(t) \rangle = \langle u^2 \rangle t^2. \tag{1.13}$$

The diffusion coefficient can be expressed in the differential form of equations (1.12) and (1.13), as follows:

$$D_t = \frac{1}{2} \frac{d\langle \Delta X^2(t) \rangle}{dt} = \langle u^2 \rangle T_L \quad t \gg T_L. \tag{1.14}$$

$$D_t = \frac{d\langle \Delta X^2(t) \rangle}{dt} = \langle u^2 \rangle t \quad t \ll T_L. \tag{1.15}$$

At long time-scales, $t \gg T_L$, the diffusion coefficient is independent of the time and the variance of the particle displacement becomes proportional to time t. This is analogous to the basic law of Brownian motion [69].

Taylor's dispersion has also been extended to turbulent flows and active suspensions [101, 117, 47]. It has been shown that the dispersion of particles in laboratory two-dimensional (2D) turbulent flows shows good agreement with Taylor's dispersion, where the mean squared displacement (MSD) of the particle at long time-scales $\langle r^2 \rangle$ $\sim t$. This dispersion is governed by a well-defined Lagrangian scale related to the forcing scale of the flow (L_f) [117]. A transition to fully developed two-dimensional (2D) turbulence can also be characterised by analysing the fluid particle trajectories and the development of self-similar diffusion [118].

Taylor's dispersion is based on the Lagrangian frame of reference. During the process in which the particles are moving in the fluid flow, their motions are tracked. In laboratory experiments, tracer particles are used to represent the motion of fluid particles [70, 10, 11, 123]. When the size of these particles is relatively small compared to the characteristic scale of the flow, and their density is the same as that of the fluid, the particles (tracer particles) faithfully follow the motion the fluid flow. By seeding tracer particles in the fluid, one is able to visualise the fluid motion and measure the time/space resolved velocities by using particle image velocimetry (PIV) [113]. To study the Lagrangian trajectories of the particles, the particle tracking velocimetry (PTV) technique is used [102].

1.3 Particles in turbulence

The previous discussion on Taylor dispersion has largely been concerned with fluid particles. However, in many practical situations, the dispersed particles in turbulence can be solids, droplets, colloids, bubbles or active suspensions [102, 71, 29]. In order to characterise the dispersion of a specific type of dispersed particle in turbulence, one has to account for the properties of the turbulent flows and the particle itself, such as the fluid viscosity, the shape of the particle and the densities. Other factors, including the particle's translational and rotational diffusivity, gravitational acceleration, particle deformability, collisions, aggregation or fragmentation, non-Newtonian fluid rheology, and electrostatic forces, may also be important [111].

The theoretical description of a particle's motion in viscous fluid flows was initially presented by Stokes [98]. Here the size of the particle (d_p) was assumed to be very small (point-like) and the relative velocity of the particle to the fluid was also very small. The equation of motion is written as:

$$m_p \frac{d\boldsymbol{u_p}}{dt} = -3\pi d_p \nu \rho_f (\boldsymbol{u_p} - \boldsymbol{u_f}) \qquad (1.16)$$

where m_p is the mass of the particle, while $(u_p - u_f)$ is the relative velocity of particle to the fluid, ν is the kinematic viscosity of the fluid, and ρ_f is the fluid density.

On the right-hand side of equation (1.16) is the frictional force (the Stokes force) acting on the particle, $m_p = (1/6)\pi\rho_p d_p^3$, where ρ_p is the density of the particle. Equation (1.16) can also be written as

$$\frac{du_p}{dt} = (\frac{\rho_f}{\rho_p})\frac{18\nu}{d_p^2}(u_f - u_p) = \frac{1}{\tau_p}(u_f - u_p) \tag{1.17}$$

where τ_p is particle response time:

$$\tau_p = (\frac{\rho_p}{\rho_f})\frac{d_p^2}{18\nu} \tag{1.18}$$

Correspondingly, the characteristic time scale of the fluid flow (τ_f) is:

$$\tau_f = \frac{\eta^2}{\nu}, \tag{1.19}$$

In this equation, η is the characteristic length scale of the fluid flow.

A dimensionless parameter, the Stokes number (St) is often used to characterise the motion of particles. It is defined as the ratio of τ_p to τ_f as

$$St = \frac{\tau_p}{\tau_f} = \frac{1}{18}\frac{\rho_p}{\rho_f}(\frac{d_p}{\eta})^2 \tag{1.20}$$

The Stokes number captures both size and density effects on the particle's dynamics. If $St \ll 1$, such that the particle response time is shorter than the characteristic time scale of the flow ($\tau_p \ll \tau_f$), these particles will remain in velocity equilibrium, where the fluid and the particle disperse at the same rate. One good example is the tracer particle: its size is much smaller than the Kolmogorov scale in 3D turbulence

($d_p \ll \eta$), and its density is identical to that of the fluid ($\rho_p = \rho_f$) [102]. If $St \gg 1$, such that the particle response time is larger than the characteristic time scale of the flow ($\tau_p \gg \tau_f$), the particles cannot adopt the dynamics of the flow [21]. There are two reasons for this: (1) If the particle has a density different from the surrounding fluid ($\rho_p \ll \rho_f$ or $\rho_p \gg \rho_f$), it will take a finite time for the particle to respond to flow accelerations; (2) If the particle has a finite size that is much greater than the characteristic scale of the turbulent flow ($d_p \gg \eta$), the velocity field of the flow acting on the particle is not uniform, which may lead to complicated behaviours.

1.3.1 Point-like particles in turbulence

A model of the dynamics of point-like particles in a turbulent flow has been proposed. It is known as the Maxey-Riley-Gatignol (MRG) equation [65, 37].

$$m_p \frac{d\boldsymbol{u_p}}{dt} = m_f \frac{D\boldsymbol{u}_f}{Dt}(x_p, t) + 3\pi d_p \nu \rho_f (\boldsymbol{u}_f - \boldsymbol{u_p}) + \frac{1}{2} m_f \left(\frac{D\boldsymbol{u}_f}{Dt} - \frac{d\boldsymbol{u_p}}{dt} \right) \qquad (1.21)$$

where m_p is the mass of the particle, m_f is the mass of displaced fluid, while $\boldsymbol{u_p}$ and $\boldsymbol{u}_f$ are the velocities of particles and fluid respectively. Moreover, (x_p, t) represents the position x_p at time t, d_p is the particle diameter, and ν is the kinematic viscosity of the fluid. The first term on the right-hand side of equation (1.21) is the acceleration of the fluid element at the position of the particle that represents the force exerted on the particle by the undisturbed flow. The second term is the Stokes forces (the same as equation (1.17)). The third term describes the displacement of a fluid when the particle moves relative to the fluid, which is called the added-mass term.

A minimal model can be achieved by integrating the added mass factor ($\beta = 3\rho_f / (\rho_f + 2\rho_p)$) and the particle response time ($\tau_p = d_p^2 / 12\nu\beta$) into equation (1.21), which is written as:

$$\frac{d\boldsymbol{u_p}}{dt} = \beta\frac{D\boldsymbol{u_f}}{Dt} + \frac{1}{\tau_p}(\boldsymbol{u_f} - \boldsymbol{u_p}). \tag{1.22}$$

The MRG model is used for simulations of point-like particles in turbulent flows with inertial effects [108, 85, 7].

1.3.2   Finite-size particles in turbulence

A particle whose size is greater than the characteristic scale of the flow ($d_p > \eta$) is referred to as a finite-size particle. To capture the finite-size effect of a particle, Faxén modified the MRG equation by averaging the fluid velocity over the surface (S_p) and the fluid acceleration over the volume of the particle (V_p) [30]. This is known as the Faxén corrections, and can be expressed as follows:

$$\begin{aligned}
\langle\frac{D\boldsymbol{u_f}}{Dt}\rangle_{V_p} &= \frac{6}{\pi d_p^2}\int_V \frac{D\boldsymbol{u_f}}{Dt}dV, \\
\langle\boldsymbol{u_f}\rangle_{S_p} &= \frac{2}{\pi d_p^2}\int_S \boldsymbol{u_f}dS,
\end{aligned} \tag{1.23}$$

where the brackets $\langle\rangle$ denote the statistical averaging. The minimal model for MRG with Faxén corrections is given by:

$$\frac{d\boldsymbol{u_p}}{dt} = \beta\langle\frac{D\boldsymbol{u_f}}{Dt}\rangle_{V_p} + \frac{1}{\tau_p}(\langle\boldsymbol{u_f}\rangle_{S_p} - \boldsymbol{u_f}) \tag{1.24}$$

Validations of the Faxén corrections for the dynamics of finite-size particles in turbulence flows have been performed in simulations and compared to the experimental results [16]. When the particle size increases, the modified model (equation (1.24)) is able to capture both the reduction of acceleration fluctuations and the increase of the acceleration correlation time. However, the model does not show an invariant accel-

eration PDF as the experimental data does. To date, the description of the motion of finite-size particles in turbulent flows remains an open question which requires experimental studies to answer [102].

Experimental studies of finite-size particles have been carried out to assess various aspects of the particles' properties and behaviours, such as the velocity and acceleration statistics of the particle [110, 84, 122, 12, 107] as well as the dispersion and mixing in turbulent flows [64, 63, 2, 119]. In 2D turbulence, the dispersion of finite-size isotropic particles (discs) has been studied [119]. It was found that the dispersion law agrees with Taylor's dispersion (equation (1.12) and (1.13)) at short and long time-scales.

In another experiment, where neutrally buoyant finite-size particles ($\sim 600 \times$ Kolmogorov scale) were studied in a turbulent flow generated between counter-rotating discs in a cylindrical container, a lift force was reported to act on the particle and lead to a coupling between the translational and rotational degrees of freedom [129]. A strong alignment was found in the direction between the angular velocity and the trajectory of the particle (~ 45 degrees).

Studies of finite-size particles in turbulent flow also support research into the passive swimming of aquatic organisms [31]. Organisms of different sizes experience totally different flow conditions [114]. At the small scale of phytoplankton and bacteria, the surrounding flows experienced by these organisms only take the form of smooth changes in flow speed over space, as their sizes are smaller than the smallest whirls. In this situation, these small organisms can be treated as point-like particles and the fluid flows are always considered as simple shear flows. However, when the size of the aquatic organisms increases to the scale of a fish (finite-size), the flow conditions they experience are a set of whirls of different sizes. These whirls cause rapid changes in the direction and speed of flow. The interactions between the fluid flow and the finite-size fish are complicated and can lead to unexpected swimming behaviours.

1.3.3 Anisotropic particles in turbulence

So far, we have discussed the motion of isotropic particles in turbulence. However, many practical applications deal with non-spherical (non-circular) particles [111].

Studies on the motion of anisotropic particles can be dated back to the 1920s, with Jeffery's [48] and Taylor's [100] research on ellipsoidal particles in shear flows. The governing equations of the dynamics of these particles are expressed as:

$$\boldsymbol{F} = m\frac{d\boldsymbol{u}_p}{dt}, \tag{1.25}$$

$$\boldsymbol{N} = \frac{d(\boldsymbol{I}\cdot\boldsymbol{\Omega})}{dt} + \boldsymbol{\Omega} \times (\boldsymbol{I}\cdot\boldsymbol{\Omega}), \tag{1.26}$$

where $\boldsymbol{F}$ is the force acting on the particles, which is based on the lab frame of reference, while $\boldsymbol{N}$ is the torque based on the the body frame of reference. In this equation, $\boldsymbol{u}_p$ is the velocity of the particle and $\boldsymbol{I}$ is the rotational inertia tensor. $\boldsymbol{\Omega}$ is the rotation rate of the particle, which is a combination of the spinning and tumbling rate. Due to the imbalance of the torques in different directions, the orientation and rotation of the ellipsoids make it difficult to predict the particle dispersion in a fluid flow. When accounting for particles with arbitrary shapes, the dynamics becomes even more complicated.

For fibre-shaped particles with a high aspect ratio (where the length of the particle is much greater than its width, $l \gg b$), the slender-body theory (SBT) was developed. The SBT was first reported in Stokes flows [13] and has been further improved and developed by several researchers [103, 19, 20, 3]. The objective of SBT is to take advantage of the particle's slenderness in order to simplify the process of obtaining approximate solutions for the flow around such bodies. Consider a slender body particle with length l and typical diameter $2a$ ($l \gg a$) moving at a velocity u_p in a viscous fluid μ_f. SBT provides us with the drag force acting on the body either parallel ($\|$) or perpendicular ($\perp$) to its axis. The canonical results are written as:

$$F_\parallel \sim \frac{2\pi\mu_f l u_p}{ln(l/a)}$$

(1.27)

$$F_\perp \sim \frac{4\pi\mu_f l u_p}{ln(l/a)}$$

Equation 1.27 shows that the differences between $F_\parallel$ and $F_\perp$ is only a factor of 2.

It was not until 2005 that the SBT was extended to the dispersion of slender body particles in isotropic turbulence for a range of turbulence Reynolds numbers [91]. The translational dispersion of the particle can be described by a simple theory that neglects the coupling between the particle's orientation and the local direction of the fluid velocity. However, the rotational motion of the particle is significantly reduced by such coupling. Recently, great successes have been achieved by applying SBT to understand the transport of bacteria by flagellar activity [56], the motion of elastic fibres in fluid flows [59], and other complex systems [97].

The anisotropic shape of the particle is important for controlling the dynamics of the particles in turbulence. However, for anisotropic particles with an aspect ratio other than that of a sphere or a thin rod, there is still no clear model to characterise their behaviours in turbulence. Recent studies of anisotropic particles in turbulence concentrate on the orientation and alignment of the particles to the turbulent stretching direction [83, 73, 72, 127, 15] and rotational diffusivity, such as the rotation rate, spinning rate and tumbling rate [77, 61, 14].

As for small-sized and neutrally buoyant anisotropic particles, they follow Lagrangian trajectories of fluid motion and behave just like the tracer particles. At the same time, they also exhibit rich orientational dynamics due to the coupling of their rotation to the velocity gradients of the turbulence field [111]. For finite-size anisotropic particles, this coupling may lead to very different preferential alignments, orientations

and dispersing strategies in turbulence when compared to the small particles. This issue merits further investigation through experimental studies.

1.4   Objectives and thesis outlines

1.4.1   Objectives

In this thesis, we present experimental results on the dispersion of finite-size anisotropic particles in laboratory two-dimensional turbulence. Both the translational motion and rotational motion are studied. In particular, we are interested in:

(1) The coupling between the translational and rotational motion of particles in 2D turbulent flows. It has been reported that this coupling may lead to unexpected diffusion behaviours of particles. For example, anisotropic Brownian particles in water confined to two dimensions show anisotropic diffusion at short time-scales [42], and ellipsoidal particles travel transversely in high concentrations of bacterial suspensions [79]. It is of interests to study how the coupling of the finite-size anisotropic particle affects its dispersion in turbulence.

(2) The interaction of the inhomogeneity of the turbulent flow with the anisotropic particles. When approaching the boundary layer wall, the shear of the inhomogeneous turbulent flow has a significant effect on the Lagrangian acceleration of inertial particles (water droplets) [38]. As pointed out at the end of the review [111], 'careful attention needs to be given to the effects of inhomogeneity of the turbulent flow on nonspherical particle motion'. In most numerical and theoretical considerations of particle interaction with the turbulent flow, the asymptotic limit of fully developed (isotropic and homogeneous) turbulent flow at high Reynolds numbers is usually considered. In most natural and laboratory turbulent flows, the flow may be inhomogeneous and have anisotropic structures [116]. The interaction of the locally anisotropic turbulent flows with finite-size anisotropic particles will be investigated in this work.

1.4.2   Thesis outlines

The structure of this thesis is outlined below.

Chapter 1: The introduction of the thesis covers the background of Brownian motion, turbulent dispersion and the dynamics of different particles in turbulence.

Chapter 2: A brief description of laboratory 2D turbulence and recent experimental results. This is followed by the descriptions of the experimental setups for turbulence generation and the specifications of the finite-size anisotropic particles studied in this thesis.

Chapter 3: The results of experiments investigating the dispersion of ellipsoidal particles with different aspect ratios in 2D turbulent flows.

Chapter 4: The results of experiments investigating the interaction between pacman-shaped particles (circular discs with a cut-out sector) and the Lagrangian structure of 2D turbulent flows.

Chapter 5: A summary of the experimental results on the dispersion of finite-size anisotropic particles in 2D turbulence, along with some suggested directions for future research.

Two-dimensional turbulence and experimental protocols

In this thesis, the dispersion of finite-size particles is studied in two-dimensional turbulent flows, more specifically, the Faraday wave driven 2D turbulence. A general introduction to 2D turbulence, the laboratory modelling of 2D turbulence, and recent experimental developments are given in the first part of this chapter.

The second part addresses the experimental protocols. The setup for the generation of Faraday wave-driven turbulence (FWT) is presented. This is followed by a description of the finite-size anisotropic particles studied in these experiments.

2.1 Two-dimensional turbulence

Despite focused efforts for more than 100 years, understanding turbulence remains one of the most complex problems in physics. A turbulent flow is characterised by chaotic changes in pressure and velocities. While turbulence is known to occur in many industrial and environmental flows, there is no universal definition of turbulence. One definition is given in the Encyclopedia of Nonlinear Science [87]:

"Turbulence is a state of a nonlinear physical system that has energy distribution over many degrees of freedom strongly deviated from equilibrium. Turbulence is irregular both in time and in space. Turbulence can be maintained by some external influences or it can decay

on the way to relaxation to equilibrium. The term first appeared in fluid mechanics and was later generalised to include far-from-equilibrium states in solids and plasmas."

2.1.1 Introduction to two-dimensional turbulence

2D turbulence was originally considered to be a mathematical simplification of 3D turbulence. However, it later emerged that 2D turbulence actually has very different properties when compared with its 3D counterpart. Kraichnan predicted the existence of two inertial ranges for homogeneous 2D turbulence. In his seminar paper on 2D turbulence published in 1967, 'Inertial ranges in two-dimensional turbulence', Kraichnan showed that two-dimensional turbulence supports inverse energy cascade, transferring energy from smaller to larger scales in the process of turbulent self-organisation [52]. The concept of the inverse cascade dramatically changes the properties of turbulence and has remained an area of intense research focus since it was first proposed [28].

If turbulence is forced at some intermediate wave numbers k_f, energy flows towards smaller wave numbers at $k < k_f$, while enstrophy (defined as the square of vorticity) flows toward higher wave numbers at $k > k_f$. This leads to a dual cascade model, namely, the inverse energy cascade and the forward enstrophy cascade, as illustrated in Figure 2.1.

(1) In the inverse energy cascade range, $k < k_f$, the energy spectrum scales as $k^{-5/3}$:

$$E(k) = C\eta^{2/3}k^{-5/3}. \tag{2.1}$$

(2) In the forward enstrophy cascade range, $k_f < k < k_\nu$ (k_ν is the wave number of the dissipative scale), the energy spectrum is proportional to k^{-3}:

$$E(k) = C'\epsilon^{2/3}k^{-3}. \tag{2.2}$$
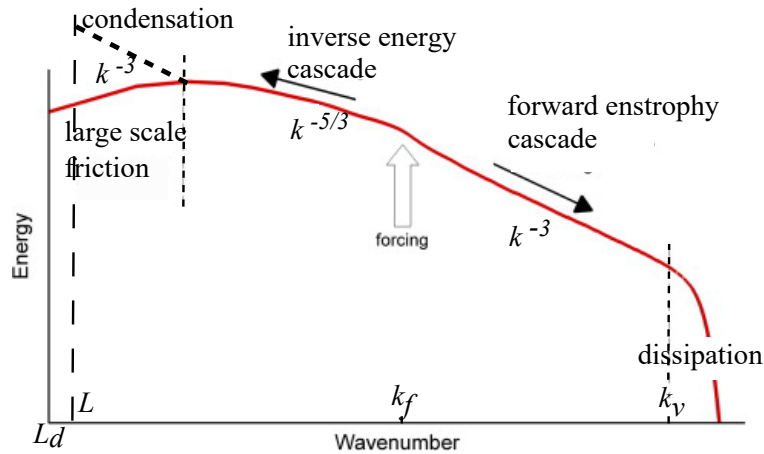
Figure 2.1: Schematic of kinetic energy spectrum of 2D turbulent flow predicted by Kraichnan. A double cascade of energy and enstrophy is illustrated. In a bounded domain, when the dissipation scale is greater than the bounded domain, $L_d > L$, spectral condensation with a steeper profile of the energy spectrum can be reached.

In equations (2.1) and (2.2), C and C' are dimensionless Kolmogorov constants, while η and ϵ are flux of the energy and the enstrophy, respectively.

One of the most important consequences of the inverse energy cascade is the accumulation of energy at the largest scale permitted by a boundary of the flow. The kinetic energy spectra in 2D turbulence are illustrated in Figure 2.1. In an infinite spatial domain, the energy delivered via the cascade will be dissipated in the presence of large-scale or uniform dissipation (e.g. bottom friction). The maximum of the spectrum in this case will stabilise at some dissipation scale L_d, which corresponds to a given wave number, $k_{a_v} \approx 2\pi (a_v^3/\epsilon)^{1/2}$, where a_v is the linear velocity dissipation rate. However, if no larger-scale energy dissipation is present, energy cascades to larger and larger scales with no possibility of reaching a steady state [121].

When the dissipation scale is greater than the size of the bounded domain, $L_d > L$, the spectral energy accumulates at the lowest wave number allowed by the system; this leads to a substantial increase of the spectral energy at the lowest wave number, as shown by the dashed line in Figure 2.1. This phenomenon is referred to as spectral condensation in 2D turbulence. In this case, a single large-scale coherent vortex is formed, resulting in a steeper spectrum, close to k^{-3}. In the review paper of

Kraichnan in 1980, he mentioned that the spectral condensation is a situation closely analogous to the Einstein-Bose condensation in an ideal boson gas at which point the atoms are almost locked together in the lowest quantum state of the system and behave like one giant super-particle [53]. The existence of of spectral condensation of turbulence energy has been confirmed. Numerical simulations showed the onset of a dipole structure [44, 93, 18], while in experiments, mostly monopoles or asymmetric vortices were observed [76, 88, 120, 115].

2.1.2   Laboratory modeling of 2D turbulence

By constraining the motion in one spatial direction, it is possible to generate fluid motion that is approximately 2D. There are two main types of constraints that are commonly used in experiments to obtain 2D turbulence: (1) flow stratification, rotation or magnetic fields; (2) geometrical constraint, in which the length scale in one direction is much smaller than in the other two [9].

In the laboratory, the electromagnetically driven flow (EMT) has long been used to model 2D turbulence [96, 76, 121]. In these experiments, turbulent flows are generated in thin electrically conducting layers driven by the Lorenz force generated by a spatially varying magnetic field, interacting with electric current flowing through the electrolyte. It has been shown the power spectrum of EMTs are consistent with Kraichnan's prediction with power-law scaling $\sim k^{-5/3}$ [17]. The observations of spectral condensation in experiments has also been reported in bounded quasi-2D turbulent flows [120, 121]. At different regimes (from weak to strong), the condensate strongly modifies both the turbulence level and its statistics. However, the forcing scale of EMT is determined by the spatial periodicity of the fixed array of magnets. In other words, once the underneath magnets array is chosen, the forcing scale of the flow is fixed which limits the flexibility of the experimental conditions.

Recently, it has been shown that the flow generated on the surface of Faraday wave turbulence (FWT) can reproduce the properties of 2D turbulence remarkably

well [109, 35]. Direct observations of the horizontal velocity field of tracer particles were performed on the surface flows produced by Faraday waves. The power spectrum of the horizontal flow driven by FWT showed scalings of the $k^{-5/3}$ law over a wide range of accelerations and frequencies with a double cascade (the inverse energy cascade and the forward enstrophy cascade), as shown in Figure 2.2 (a) and (b). The energy is injected into the system at half the wavelength of the Faraday waves, this is an appealing feature of FWT when compared to EMT. By altering the driving frequencies of the FWT, one can easily change the wavelength of the fluid flows and generate a series of 2D turbulence with different forcing scales. The physics of the 2D turbulence generation by Faraday waves, including the conversion of the energy of vertical fluid motion into horizontal vortices has been studied in detail [34]. It was shown that the generation of vortices in Faraday waves is caused by the lattice of oscillons who's mobility affects the horizontal flow.
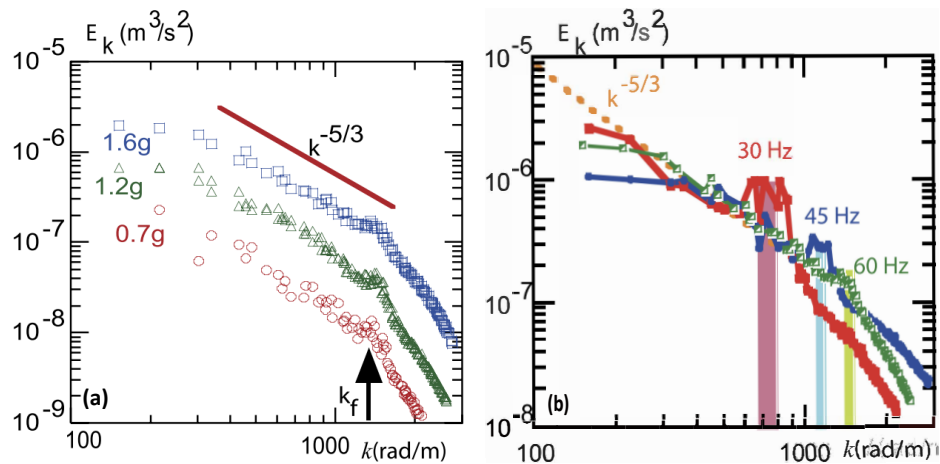
Figure 2.2: Wave number spectra of the kinetic energy of horizontal flow of FWT at (a) 0.7 g, 0.9 g and 1.2 g at 60 Hz; (b) 30 Hz, 60 Hz and 120 Hz [35]

Example trajectories of tracer particles on the surface flow in fully developed FWT are shown in Figure 2.3(a). The probability density function (PDF) of the velocity components u_x and u_y, normalised by the r.m.s. value of the velocity fluctuations ($\langle u \rangle$), are illustrated in Figure 2.3(b). The PDFs follow Gaussian distributions, which is as expected for isotropic 2D turbulent flows.
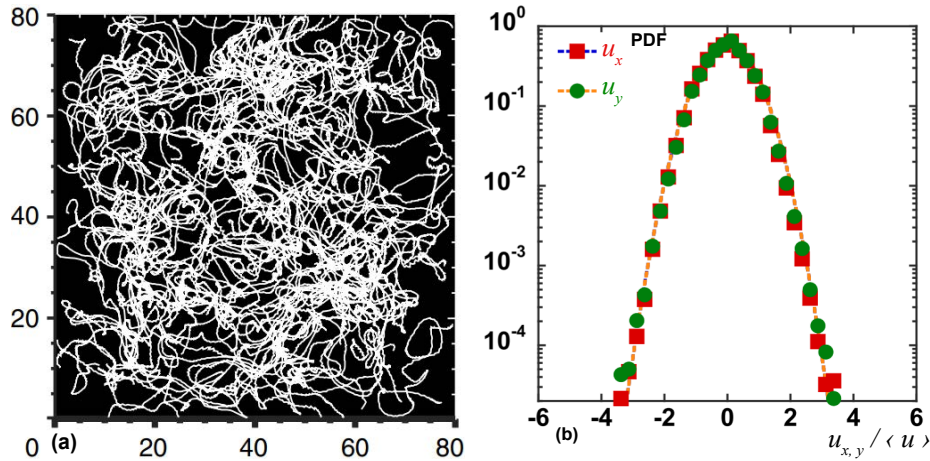
Figure 2.3: (a) Example trajectories of tracer particles on the surface flow in fully developed FWT; (b) Probability Density Function (PDF) of the velocity components of the fluid particles, u_x and u_y, in FWT. The velocities are normalised by the r.m.s. value of the velocity fluctuations. Experimental parameters: frequency f = 60 Hz, forcing scale of the flow L_f = 4.4 mm [117, 36].

The discovery of the Faraday wave-driven 2D turbulence has greatly improved the capacity of the experimental modelling of 2D turbulence. For instance, the complementation of the electromagnetically-driven turbulence by the Faraday wave-driven turbulent flows has widened the range of forcing scales and kinetic energies achievable in laboratory. Experiments have been performed to revisit the single-particle dispersion and explore topological aspects of 2D disordered and fully turbulent flows [117, 118].

2.1.3 Lagrangian scale and coherent structures in two-dimensional turbulence

As turbulence is a state of a flow dominated by a hierarchy of scales, it is important to understand which of these scales mostly affects particle dispersion. By seeding with tracer particles, it is possible to experimentally study the dispersion of fluid particles in turbulence. It has been shown that particle dispersion in 2D turbulence is determined by a single measurable Lagrangian scale, which is related to the forcing scale (L_f) [117]. By analysing the Lagrangian statistics of the fluid particles, the diffusion

coefficients D of these particles were derived for a wide range range of experimental conditions and could be described as $D = uL$. Here, u is the characteristic velocity of the particle, while L is the Lagrangian integral scale, which was shown to be close to $0.75\ L_f$ for all the experiments.

Experiments have been conducted to investigate the dispersion of finite-size particles with dimensions comparable to the forcing scale of the flow [119]. An abrupt change was observed in the diffusive transport of inertial objects in wave-driven turbulence as a function of the object size. The turbulent diffusion coefficient D of finite-size objects underwent a sharp change when the object size r_p approached the forcing scale of the flow L_f.

To understand the behaviour of the finite-size particles, the fluid motion was investigated using two types of Lagrangian correlation functions, computed using horizontal velocities $\boldsymbol{u}$ measured along tracer trajectories [119]. For a single particle, the auto-correlation function was calculated as $\rho_{11}(\tau) = \langle \boldsymbol{u_1}(t_0 + \tau)\boldsymbol{u_1}(t_0)\rangle/\sigma^2$, where $\langle\rangle$ denotes statistical averaging over different particles, $\boldsymbol{u_1}$ is the translational velocity of the particle, and σ^2 is the velocity variance. For particle pairs, the directional cross-correlation functions were also computed as $\rho_{12}(\tau, d_{12}(t_0)) = \langle \boldsymbol{u_1}(\tau)\boldsymbol{u_2}(\tau)\rangle/\sigma^2$ [106], where $\boldsymbol{u_1}$ and $\boldsymbol{u_2}$ denote the velocities for different fluid particles, while d_{12} is the initial distance between these two particles.

The correlation functions, ρ_{11} and ρ_{12}, provide different types of information about the memory of the flow, which can be characterised via the Lagrangian characteristic time scales T_L and T_{12}. The time scale T_L is given by the integral $T_L = \int_0^{T_m} \rho_{11}(\tau)d\tau$, while the cross-correlation scale can be obtained as $T_{12} = \int_0^{T_m} \rho_{12}(\tau)d\tau$, where $T_m \approx 20$ s is the typical time of a measurement. ρ_{11} underwent an exponential decay in the first several seconds and stayed around 0 afterwards, while ρ_{12} stayed close to 1 for a long time. Analysis of ρ_{11} and ρ_{12} suggested that a large number of pairs travelled together for a long time without separation, forming a coherent river-like bundle structure. In contrast, individual particles quickly (on a time scale T_L) forgot their initial direction.

The existence of coherent bundles of non-diverging particle has been confirmed in both EMT and FWT experiments [116]. These experiments have shown that the particle pair dispersion is a process that depends on both the forcing scale L_f and on the variance of the turbulent velocity fluctuations $\langle u^2 \rangle$. Such bundles have been also detected using a topological tool based on the concept of braids [116]. The structure of the coherent bundle in Figure 2.4 reveals a large number of entangled fluid particle trajectories. Groups of fluid particle pairs travel within coherent bundles for a long time before separating. The width of the bundle is related to the turbulence forcing scale L_f. Figure 2.4 (b) - (d) shows the evolution of a bundle over time. The coherent bundle consists of four segments. Each segment exists about 4 T_L. These coherent bundles may split into two bundles occasionally, yet most strands stay together, remain untangled and execute complex collective motions. The structure of a single bundle is illustrated in Figure 2.4 (e) for 16 T_L.

In locally anisotropic turbulence, the particle pair dispersion depends on the width of the bundles. The importance of non-diverging pairs of particles (coherent bundles) in the statistics of laboratory 2D turbulence has been discussed before. Evidence in support of the existence of clusters of non-diverging particle pairs has also been presented by Sokolov and Reigada [95]. By analysing experimental data produced via electromagnetically generated turbulence of thin layers of electrolytes [75], it was found that most of the initially close particles move close to each other, forming non-diverging pairs for a considerable period of time and then splitting into smaller clusters. The characteristic dimension of the clusters was found only slightly larger than λ and the mean squared separation between the particles was reported to be determined by the characteristic distance between the clusters. The authors conclude that the pair dispersion is connected with rare and extreme events and the majority of pairs in the flow belong to non-diverging clusters [95].

This local anisotropy, observed in laboratory 2D turbulence, dominates the pair separation, causing significant deviations from statistical properties predicted in isotropic
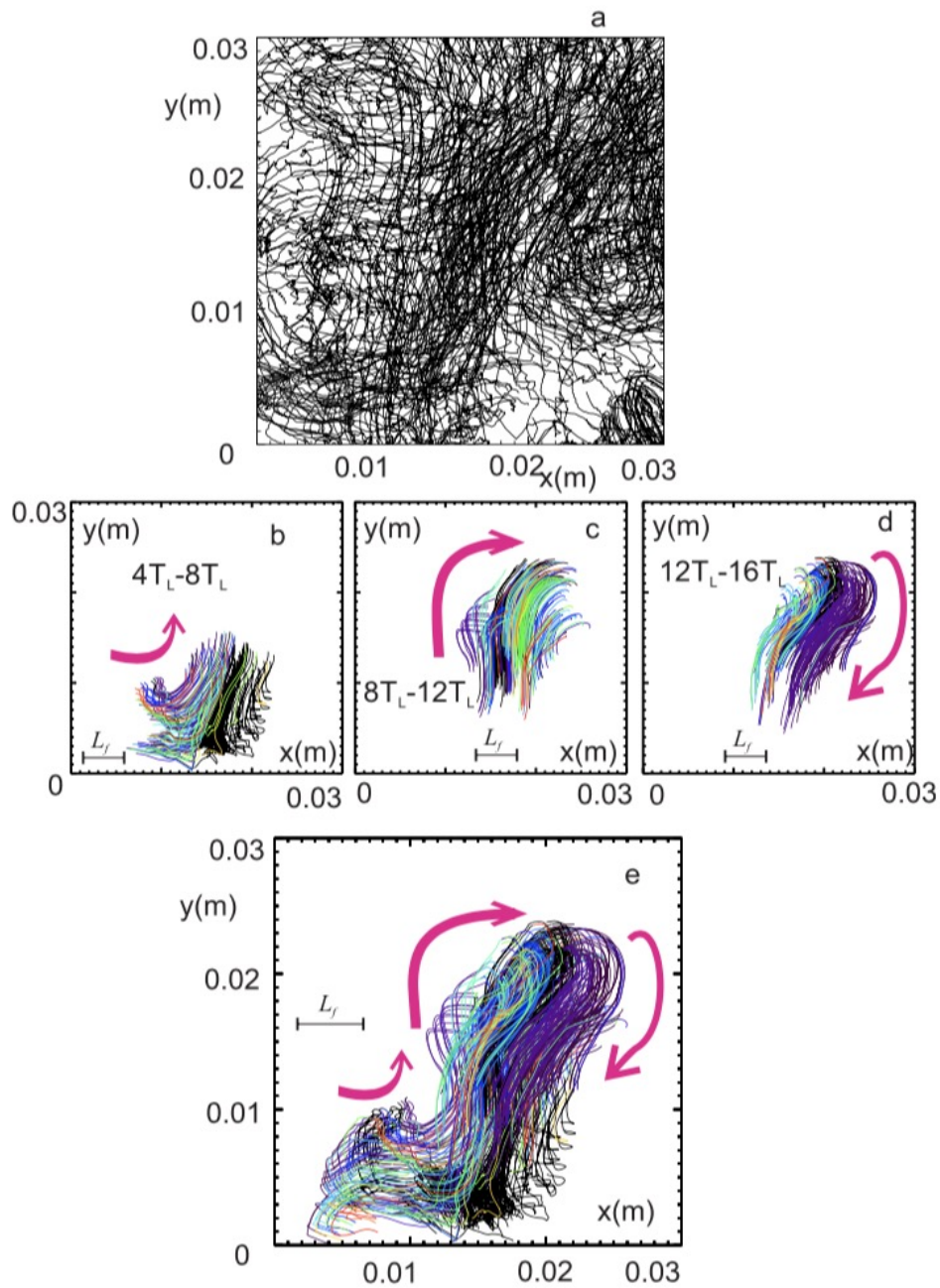
Figure 2.4: Analysis of Lagrangian trajectories in FWT driven at f = 60 Hz. The turbulence forcing scale, L_f = 4.4 mm. (a) A subset of Lagrangian trajectories (1 % of all trajectories are shown for clarity). Coherent bundles detected from (a) at different time intervals; (b) (4-8) T_L; (c) (8-12) T_L; and (d) (12-16) T_L; (e) A coherent bundle identified for the time interval (0-16) T_L by overlapping the coherent bundles of 4 T_L segments, (b)-(d). The scale bar in panels (b)-(e) shows the forcing scale [116].

turbulence [116]. These bundles strongly influence the transport of inertial particles [119] or can be utilised to design turbulence-driven rotors [36].

2.2   **Experimental setup**

Faraday waves are excited parametrically at the fluid surface in a container mounted on top of an electrodynamics shaker (TIRA TV 55240/LS-340, 4 kN, DC-4 kHz). Above a critical acceleration threshold (a_{th}), surface waves are generated at half of the shaker frequency. The dispersion relation of the surface wave is $\omega^2 = gk + (\sigma/\rho)k^3$, where ω is the angular frequency of linear waves, g is the gravity acceleration, σ is the surface tension, ρ is the density of the fluid, and k is the wave number [89]. The Faraday waves are modulationally unstable and quickly disintegrate into an ensemble of oscillating solitons or oscillons [34, 89]. It has been shown that the kinetic energy of turbulent flow at the water surface is proportional to the amplitude of the vertical acceleration [35].

The monochromatic forcing is varied within a frequency range f from 30 to 120 Hz, which results in Faraday wavelengths (λ) in the range of [6 - 15.4] mm. The corresponding forcing scale of the flow is defined as half of the wave number, $L_f = \lambda/2$. The peak-to-peak vertical acceleration a is controlled in the range of $a = [0.1 - 3]$ g, where g is the gravitational acceleration. The schematic of the experimental setup is illustrated in Figure 2.5. The circular container is 290 mm in diameter and with a depth of 87 mm. Water is filled into the container up to the brim. The contact line of the fluid along the brim of the container is kept wet in order to avoid the influence of the meniscus on the wave field. An Andor Neo sCMOS camera is used to record the particle motions on the water surface.

The velocity fields and particle trajectories are obtained using particle image velocimetry (PIV) and particle tracking velocimetry (PTV) by seeding tracer particles or finite-size particles on the surface flow. The recorded images are processed and analysed using FIJI /ImageJ. We use Matlab and Interactive Data Language (IDL) for further data analysis.
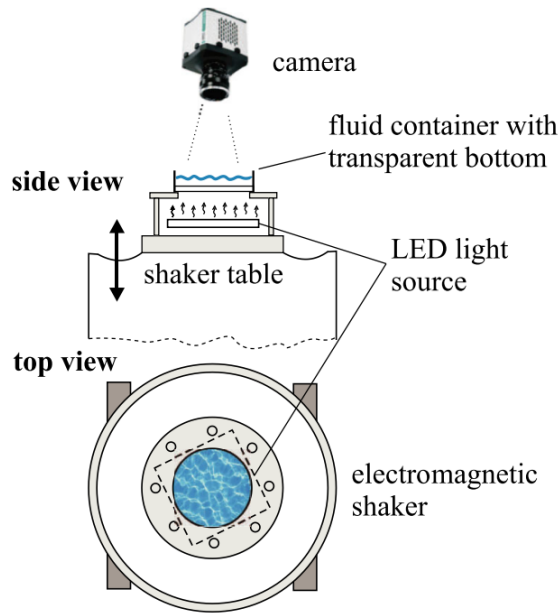
Figure 2.5: Experimental setup for Faraday wave-driven turbulence (FWT)

2.3   Finite-size anisotropic particles

Since the inverse energy cascade in 2D turbulence for which energy injected at an intermediate forcing scale L_f is transferred to larger scales [52], the Kolmogorov scale in 2D turbulence might not be as important as it is in the 3D context. Currently, most studies of finite-size particles in 2D turbulence are still restricted to particles with sizes around the Kolmogorov scale [74, 78]. Recently, it has been shown that the dispersion of either tracer particles or finite-size particles is determined by the forcing scale of the flow (L_f) [117, 119]. Thus, the sizes of the anisotropic particles studied in this thesis are selected based on the forcing scale of the 2D turbulence, ranging from $0.3\,L_f$ to $10\,L_f$.

All of these particles are designed using the cloud-based CAD/CAM software Fusion360 and printed using a 3D printer (Ultimaker 2+) with ABS polymers. The density of these particles is kept similar to water density ($\sim 1.0\,\mathrm{g/cm^3}$). After printing, all particles are rinsed and immersed in water for 24 hours to ensure the removal of any residual substances that could potentially pollute the air-water interface during the experiments. The experiments are conducted in 2D turbulence where all the particles are floating on the surface of the waves. The increase of the thickness of

the particle would only add mass and inertia to the particles' diffusion properties. Particles with thickness between 0.5 to 4 mm have been tested and no effect of the thickness is observed. For this reason, the thickness of all the particles used in this thesis were kept at 0.5mm for consistency.

For each experimental condition, more than 500 individual movies have been recorded for further analysis. Only a small number of particles are introduced into the flow for each measurement to avoid interactions and collisions between particles.

2.3.1 Ellipsoidal particles

Ellipsoidal particles (ellipsoids) of various sizes and aspect ratios are studied in this thesis. An illustration of the ellipsoidal particle is shown in Figure 2.6 (a). The major axis (*aa*) of the ellipsoidal particle varies from 3 mm to 40 mm. The aspect ratio $\gamma = bb/aa$, is in the range of 0.1 (thin ellipsoid) to 1 (circular disc). Anisotropic particles with aspect ratios in this range are not accounted for under the slender-body theory (SBT), meaning that experimental studies are required. All particles have thicknesses of 0.5 mm. The top of the particles are coated with Teflon in order to avoid droplet accumulation on the particle surface in conditions of steep waves. A circular disc (ellipsoidal particle with $\gamma = 1$) is used as a reference particle for studying the effect of anisotropic shapes. A grey bar is marked on each circular disc to track its orientation.

We track the position of each ellipsoidal particle from the centre of mass (COM) and the orientation (θ_{aa}) from the angle between its major axis and the XX axis in Cartesian coordinates, as shown in Figure 2.6 (b). Because ellipsoids have two axes of symmetry, θ_{aa} is in a range of -90 ° to 90 °. A 'fitting ellipsoid' function in ImageJ is used to obtain the COM position and θ_{aa} directly. For a circular disc, the tracking is based on the marker.
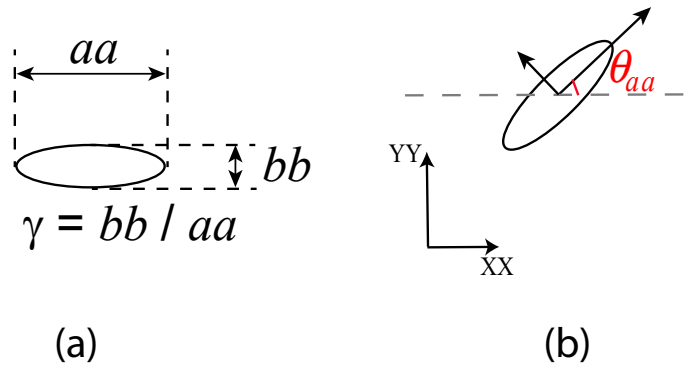
Figure 2.6: (a) Schematic of ellipsoidal particles with sizes of major axis (*aa*) and minor axis (*bb*). Aspect ratio (γ) is defined as bb/aa. *aa* varies from 3 mm to 40 mm and γ is within the range of 0.1 (thin ellipsoid) to 1 (circular disc); (b) The orientation of an ellipsoidal particle (θ_{aa}) is the angle differences between its major axis and the XX axis, $\theta_{aa} \in$ -90 ° to +90 °.

2.3.2 Pacman-shaped particles

The second type of anisotropic finite-size particle is a circular disc with a cut-out sector. The shape of this type of particle is reminiscent of the video game character "Pac-Man" [https://en.wikipedia.org/wiki/Pac-Man], thus we refer to them here as pacman-shaped particles. r_s is the radius of the circular disc, which is in the range of $r_s \in$ [2.5 mm, 40 mm], while α is the angle of the cut-out sector, where $\alpha \in$ [0°, 270°]. A schematic of a pacman-shaped particle is shown in Figure 2.7. The thicknesses of the particles are 0.5 mm. To avoid splashing of the water in the wavy turbulent flows, a side wall (hull) is added to the edge of the particle. The height of this wall is 3 mm. A circular disc is used as a reference particle. Here, a quarter of the circular disc is marked in grey so that its position and orientation can be tracked using the same algorithm as for the pacman-shaped particle.

The position of the pacman-shaped particle is tracked from the centre of mass (COM). The orientation of the particle (θ_p) is defined along the bisector, pointing opposite to the cut-out sector as shown in Figure 2.7, where $\theta_p \in$ [-180°, 180°]. A unit vector along the direction of θ_p is denoted as $\mathbf{n_p}$. Special attention is required to de-
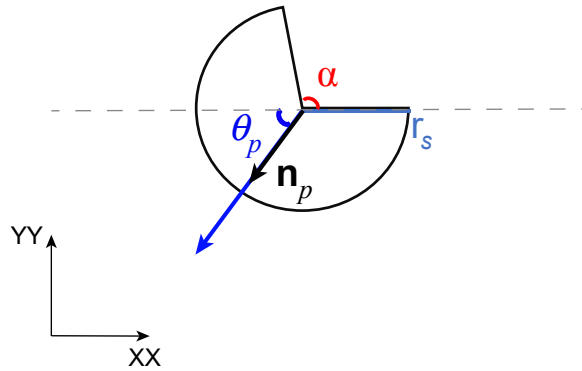
Figure 2.7: Schematics of pacman-shaped anisotropic particles. The size of this particle r_s varies from 2.5 mm to 40 mm. The cut-out sector is controlled by the angle α, where α ranges between $0°$ (circular disc) and $270°$ (a sector of a circular disc). The orientation of the particle is defined as θ_p with associated unit vector $\mathbf{n_p}$, where $\theta_p \in$ is in a range of -180 ° to +180 °.

termine the orientation of the pacman-shaped particle from the recorded images due to their irregular shapes. A detailed tracking procedure is listed in Appendix A.

2.4   Experimental limitations

The experimental limitations of this thesis ares listed as follows,

(1) The current driving frequencies of generating 2D turbulence are altered between 30Hz and 120Hz, which leads to the forcing scale varies from 7.7mm to 3mm. A wider forcing scale range may contribute to the consistency of the thesis.

(2) Due to the limitation of the container, the largest size of particles are $aa = 40$mm for ellipsoidal particle and $r_s = 40$mm for pacman-shaped particle. The diffusion properties of these larger particles are still unknown.

(3) New discoveries may arise if a wider range of size ratio (aa/L_f for ellipsoidal particle and r_s/L_f for pacman-shaped particle) is reached.

(4) The current experiment are conducted within 40 seconds. A longer investigation time may be required to discover the full movement of pacman-shaped particles.

(5) 500 individual movies are recorded for each experimental conditions. A large amount of statistics may be required.

Diffusion of ellipsoids in two-dimensional turbulence

This chapter reports the translational and rotational motion of ellipsoidal particles advected in wave-driven 2D turbulence (FWT).

We find that the ellipsoidal particles have preferential diffusing directions when transported in 2D turbulence. The preferred direction can be tuned by altering the ratio of the major size (aa) of the particle to the forcing scale of turbulent flow (L_f). When $aa > L_f$ (**large** particle), the preferential diffusing direction is along the longitudinal axis (major axis) of the ellipsoidal particle. When $aa < L_f$ (**small** particle), the particle prefers to move transversely (minor axis). The coupling between the translational and rotational motion of ellipsoidal particles is found to be dependent on the ratio aa/L_f. The features of the ellipsoidal particle's dispersion in turbulence can be understood by considering the interaction of the particle with the structure of the underlying coherent bundles in 2D turbulent flows.

The content of this chapter is based on the following journal article: Yang, J., Francois, N., Punzmann, H., Shats, M., and Xia, H. Diffusion of ellipsoids in laboratory two-dimensional turbulent flow, *Physics of Fluids* 31, 8 (2019), 085116 [125].

3.1   Particle displacements in the laboratory and body frames of reference

In this experiment, ellipsoidal particles as described in chapter 2 are studied. A schematic trajectory (red dashed line) of an ellipsoidal particle diffusing on the surface flow of FWT over four consecutive frames in the lab frame of reference is shown in Figure 3.1. Starting from time t_0, the ellipsoid has a location coordinate, labelled as (x_t, y_t), where t = 1, 2, 3... The displacements of ellipsoidal particles in the lab frame of reference can be computed as $\Delta r_x(t) = x_t - x_{t-1}$, $\Delta r_y(t) = y_t - y_{t-1}$ and the total squared displacement is equal to $\Delta r_t^2 = \Delta r_x(t)^2 + \Delta r_y(t)^2$. The translational velocities of the ellipsoid in the lab frame of reference can be derived as $v_j(t) = \Delta r_j(t)/\Delta t$, where $j = x$ or y. The corresponding orientation of velocity ($\theta_v(t)$) is a function of two velocity components as $\theta_v(t) = \arctan(\frac{v_y(t)}{v_x(t)})$. The range of θ_v is between -180° and +180°.

For the rotational motion, the orientation of the ellipsoidal particle is θ_{aa}, such that the angular velocity of the ellipsoid can be computed as a function of the angular displacement over the time interval as $\omega_t = \Delta\theta_{aa}(t)/\Delta t$, where $\Delta\theta_{aa}(t) = \theta_{aa}(t + \Delta t) - \theta_{aa}(t)$.

In order to characterise whether the particle is traveling longitudinally or transversely, new coordinates are created based on the major axis and minor axis of the ellipsoidal particle for each frame. This is referred to as the body frame of reference. The schematic of the same particle trajectory illustrated in Figure 3.1 is redrawn in Figure 3.2 (a) based on the body frame of reference. The new x axis is along the longitudinal direction (*aa*) of the ellipsoid and is denoted as X_{aa}; and the new y axis is along the latitudinal direction (*bb*) of the ellipsoid as X_{bb} for each frame. The corresponding displacements in the body frame of reference, $\Delta r_{aa}(t)$ and $\Delta r_{bb}(t)$, satisfy the relation that $\Delta r(t)^2 = \Delta r_{aa}(t)^2 + \Delta r_{bb}(t)^2$.

The calculations of $\Delta r_{aa}(t)$ and $\Delta r_{bb}(t)$ require a rotation matrix. For example,
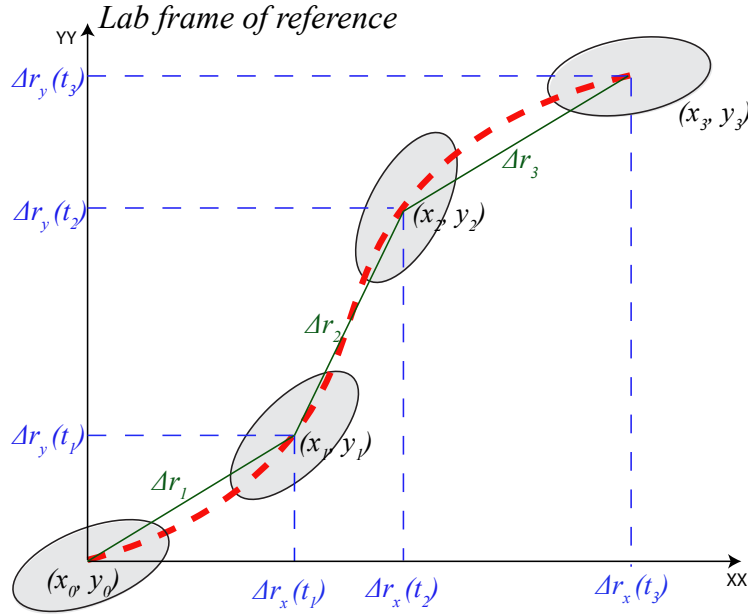
Figure 3.1: A schematic trajectory of an ellipsoidal particle in the lab frame of reference.

for $\Delta r_{aa}(t_2)$ in Figure 3.2 (b), $\Delta r_{aa}(t_2)$ is the sum of two parts, where $\Delta r_{aa}(t_2) = \Delta r_y(t_2) \times sin(\theta_{aa}(t_2)) + \Delta r_x(t_2) \times cos(\theta_{aa}(t_2))$. The general expression of the displacements in the body frame of reference is as follows:

$$
\begin{bmatrix} \Delta r_{aa}(t) \\ \Delta r_{bb}(t) \end{bmatrix} = \begin{bmatrix} \cos\theta_{aa}(t) & \sin\theta_{aa}(t) \\ -\sin\theta_{aa}(t) & \cos\theta_{aa}(t) \end{bmatrix} \times \begin{bmatrix} \Delta r_x(t) \\ \Delta r_y(t) \end{bmatrix}
$$

3.2   Translational diffusion of ellipsoids

We first compare the translational diffusion of the ellipsoids of different sizes. In the laboratory frame of reference, the statistically averaged MSD of the ellipsoids $\langle \Delta r^2 \rangle$ is shown in Figure 3.3 (a). Δr is the total displacement of a particle and $\langle \rangle$ denotes the ensemble average over many trajectories. A 4 mm and a 40 mm ellipsoid with the same aspect ratio ($\gamma = 0.25$) are tracked in FWT for more than 30 s. The flow are excited at a frequency $f = 60$ Hz with the corresponding forcing scale of this flow $L_f = 4.4$ mm. The MSDs of both ellipsoidal particles show a ballistic regime at short time-scale ($\langle \Delta r^2 \rangle \sim t^2$) and a diffusive regime at long time-scale ($\langle \Delta r^2 \rangle \sim t$). This
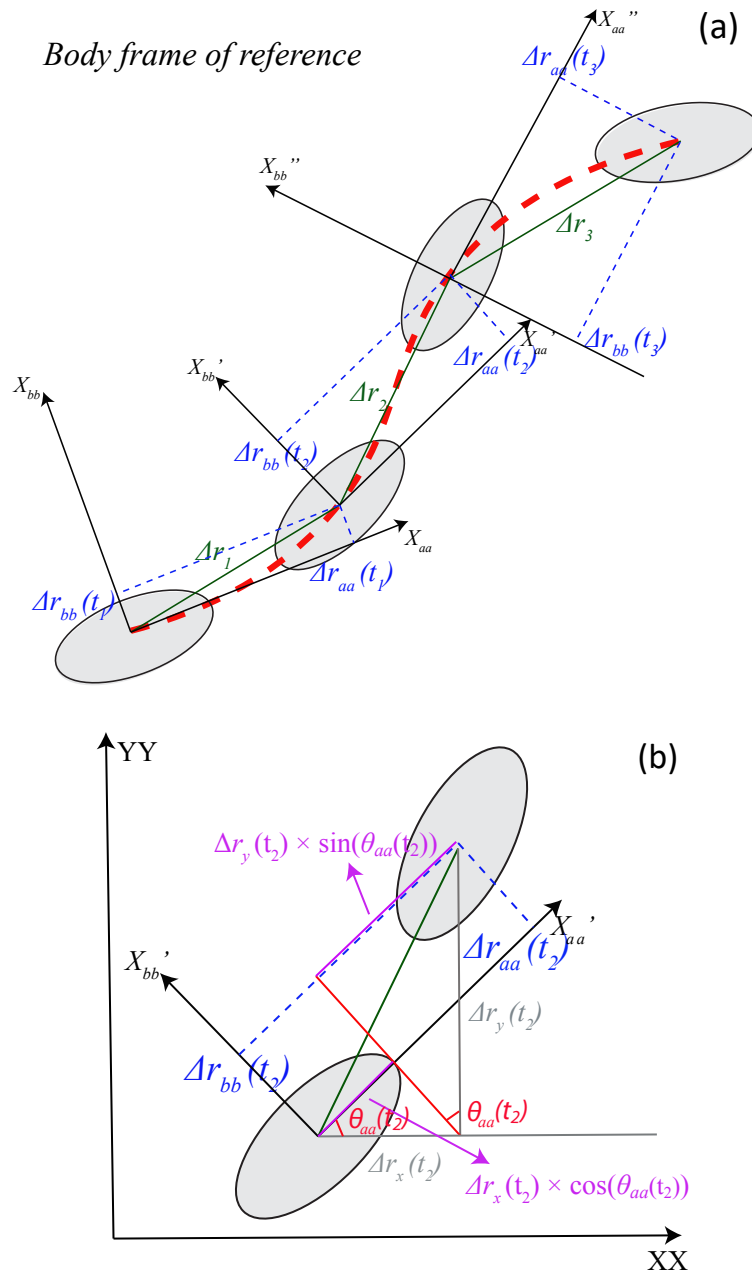
Figure 3.2: (a) A schematic trajectory of an ellipsoidal particle in the body frame of reference; (b) Calculation process of displacements in the body frame of reference

type of diffusive behaviour is seen for all particles with sizes *aa* varying from 3 mm to 40 mm and aspect ratios γ varying from 0.1 to 1. Due to the lighter weight and reduced inertia of small particles, the MSD values for 4mm ellipsoidal particles are consistently higher than that for the 40mm particles.

To test whether the anisotropic shape of the ellipsoids has any effect on the MSD,
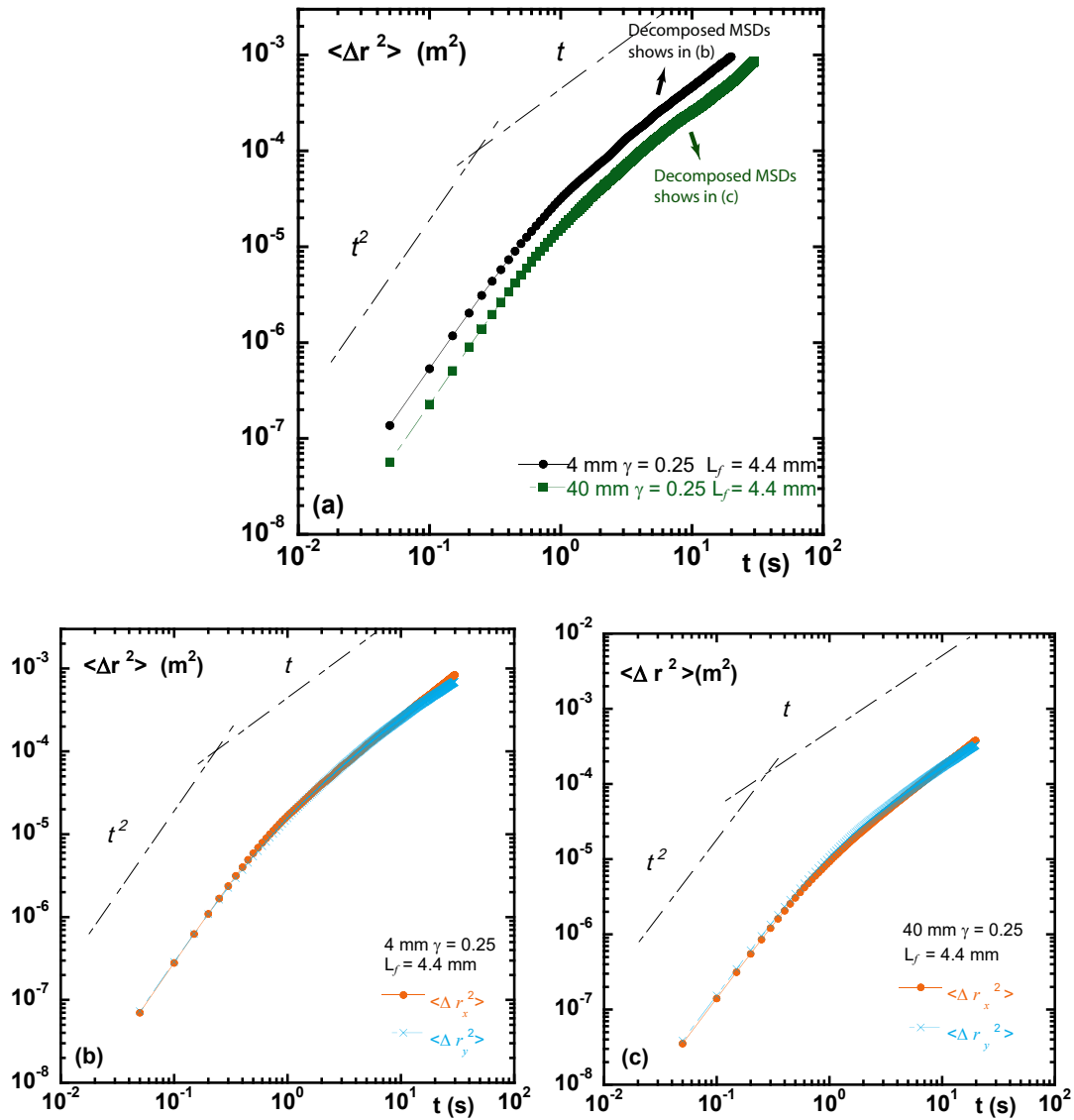
Figure 3.3: MSD of ellipsoids in the laboratory frame of reference: (a) *aa* = 4 mm and 40 mm, respectively; (b) Decomposed MSD components of ellipsoids in the laboratory frame of reference: *aa* = 4 mm; (c) Decomposed MSD components of ellipsoids in the laboratory frame of reference: *aa* = 40 mm. The flow conditions are the same for both experiments, where f = 60Hz, L_f = 4.4 mm, while the aspect ratios γ for both particles are 0.25.

the displacements of ellipsoids are decomposed along the XX and YY axes as Δr_x and Δr_y in the lab frame of reference. The decomposed MSDs of ellipsoids ($\langle \Delta r_x^2 \rangle$ and $\langle \Delta r_y^2 \rangle$) are shown in Figure 3.3 (b) for *aa* = 4 mm and Figure 3.3 (c) for *aa* = 40 mm, respectively. In the same flow condition (f = 60Hz and L_f = 4.4 mm), there is approximately no difference between $\langle \Delta r_x^2 \rangle$ and $\langle \Delta r_y^2 \rangle$ for the two different sizes of particles over the entire observation time. Similar to the total displacements, both $\langle \Delta r_x^2 \rangle$ and

$\langle \Delta r_y^2 \rangle$ present a transition from a ballistic regime to a diffusive regime with the increase in time. These results indicate the isotropic diffusion of ellipsoidal particles in the lab frame of reference.
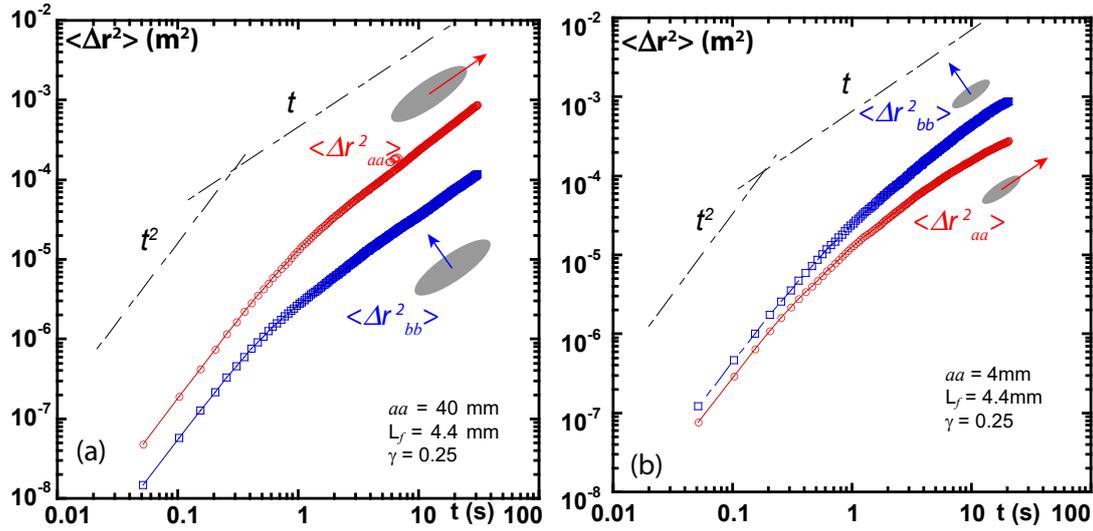
Figure 3.4: Decomposed MSD components in the body frame of reference for different sizes of ellipsoids in the same flow condition. (a) *aa* = 40 mm; (b) *aa* = 4 mm. The flows are excited at 60 Hz where L_f = 4.4 mm. The aspect ratios γ for all particles are kept at 0.25. $\langle \Delta r_{aa}^2 \rangle$ is in red, $\langle \Delta r_{bb}^2 \rangle$ is in blue.
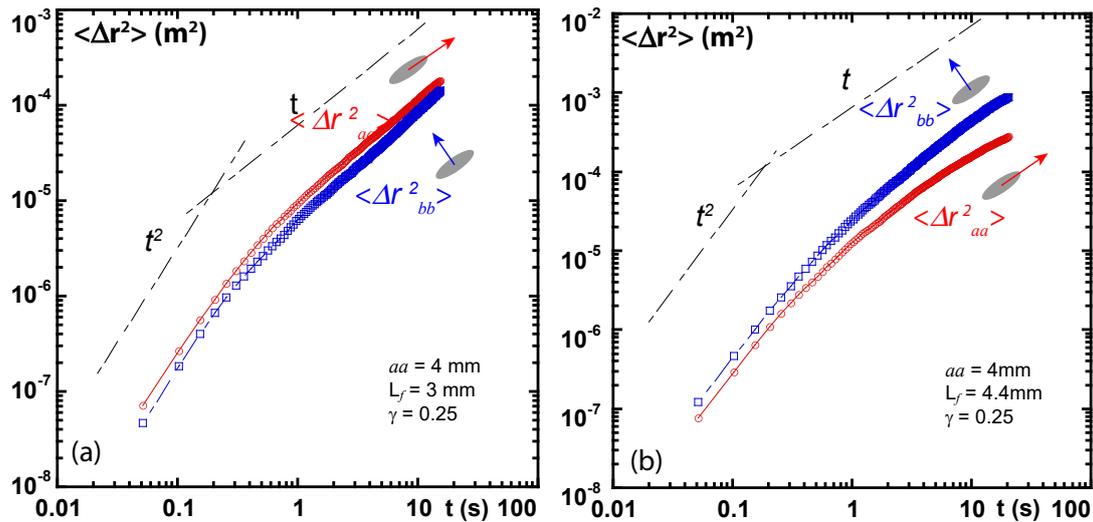
Figure 3.5: Decomposed MSD components in the body frame of reference for the same size of ellipsoid in different flow conditions. (a) f = 60 Hz, L_f = 4.4 mm; (b) f = 120Hz, L_f = 3 mm. The size of ellipsoids *aa* is equal to 4 mm, while the aspect ratios γ for all particles are kept at 0.25. $\langle \Delta r_{aa}^2 \rangle$ is in red, $\langle \Delta r_{bb}^2 \rangle$ is in blue.

By following the calculation process using the rotation matrix, we are able to obtain the displacements of the ellipsoids in the body frame of reference, Δr_{aa} and Δr_{bb}. The corresponding decomposed MSDs ($\langle \Delta r_{aa}^2 \rangle$ and $\langle \Delta r_{bb}^2 \rangle$) are shown in Figure 3.4, where Δr_{aa} is along the major axis of the ellipsoidal particle and Δr_{bb} is along the minor axis.

A clear difference between the MSDs along the two axes for particles in the body frame of reference can be found in Figure 3.4 (a) and (b). Here, the flow conditions are kept the same: a driving frequency f = 60 Hz with a forcing scale L_f = 4.4 mm. For the 40 mm ellipsoidal particle, $\langle \Delta r_{aa}^2 \rangle > \langle \Delta r_{bb}^2 \rangle$, which indicates that these ellipsoids tend to move along their major axes. For the 4 mm ellipsoids, $\langle \Delta r_{aa}^2 \rangle < \langle \Delta r_{bb}^2 \rangle$. This can be interpreted to suggest that these particles prefer to travel transversely (along the minor axis).

Similar results can also be achieved by diffusing the same ellipsoidal particle (aa = 4mm, γ =0.25) in different flow conditions, L_f = 3 mm and 4.4 mm, respectively. As shown in Figure 3.5 (a) and (b), the MSD of the 4 mm ellipsoid shows a slightly higher value along the major axis compared to that along the minor axis when the forcing scale L_f = 3 mm, $\langle \Delta r_{aa}^2 \rangle > \langle \Delta r_{bb}^2 \rangle$. However, when the forcing scale L_f = 4.4 mm, the opposite result is obtained, where $\langle \Delta r_{bb}^2 \rangle > \langle \Delta r_{aa}^2 \rangle$. This behaviour is shown in Figure 3.5 (b). The arrows in the inset illustrations of Figure 3.4 and Figure 3.5 indicate the specific component of the MSD being analysed in the body frame of reference. The above results clearly demonstrate that the anisotropic shape of ellipsoidal particles contribute to the anisotropic diffusion in the body frame of reference, suggesting that the particle has a preferential diffusing direction (either along its major or minor axis).

Several questions arise from these observations: (1) Which scale or parameter determines the dispersion of ellipsoids? (2) Why do larger ellipsoids diffuse faster along the major axes while the smaller ellipsoids diffuse faster in the direction of the minor axes? (3) Why do ellipsoids change their preferential diffusion direction in different turbulent flows?

In order to answer these questions, we conduct a detailed study of how the diffusion coefficients change under different experimental conditions. The diffusion along the major and minor axes are denoted as D_{aa} and D_{bb} respectively. The decomposed MSDs in the body frame of reference are also diffusive at long time-scale, satisfying the following relations:

$$\langle \Delta r_{aa}^2 \rangle \approx 2D_{aa}t, \qquad t \gg T_f, \tag{3.1}$$

$$\langle \Delta r_{bb}^2 \rangle \approx 2D_{bb}t, \qquad t \gg T_f, \tag{3.2}$$

where aa and bb denote the quantities along the major and minor axes respectively. T_f represents the characteristic time scale of the fluid flow, which is calculated as the integral of the auto-correlation function of the fluid particles.

The previous results on Δr_{aa}^2 and Δr_{bb}^2 indicate the importance of both the major size of the particle (aa) and the forcing scale of the flow (L_f). With this in mind, we introduce a new parameter, the size ratio. It is defined as the ratio of the major size of the ellipsoid to the forcing scale of the flow as aa/L_f.

The diffusion coefficients in the body frame of reference (D_{aa} and D_{bb}) are calculated based on equations (3.1) and (3.2). The relations of D_{aa} and D_{bb} as a function of the size ratio (aa/L_f) are shown in Figure 3.6 (a). The aspect ratios are kept to the same for all the particles, $\gamma = 0.5$. The results show that when size ratio $aa/L_f < 1$, D_{bb} is greater than D_{aa}, indicating higher diffusing rate along the minor axis. However, D_{bb} can exceed D_{aa} ($D_{aa} > D_{bb}$) when the size ratio is greater than 1 ($aa/L_f > 1$), which means that if the particle is relatively large, the preferential diffusing direction for the ellipsoids is towards its major axis.

The differences between D_{aa} and D_{bb} are characterised by computing the ratio of the decomposed diffusion coefficients, D_{aa}/D_{bb}. The relations of D_{aa}/D_{bb} to the par-

ticle aspect ratio are shown in Figure 3.6 (b). When $\gamma = 1$, which indicates an isotropic circular disc, D_{aa}/D_{bb} shows no bias in terms of diffusing directions in the body frame of reference. Here, $D_{aa}/D_{bb} \approx 1$, which is as expected for an isotropic particle. When $\gamma \neq 1$, aa/L_f becomes a critical parameter that controls the anisotropic dynamics of ellipsoidal particles. These results clearly demonstrate that if $aa/L_f > 1$, $D_{aa}/D_{bb} > 1$, which means the major axis of the ellipsoids is the preferential diffusing direction. If the size ratio is smaller than 1, $aa/L_f < 1$, and the ellipsoids prefer to travel transversely.

The effect of the aspect ratio (γ) can also be investigated by comparing three different ellipsoid aspect ratios ($\gamma = 0.25$, 0.5 and 0.75). Results are presented in Figure 3.6 (b). Although the degree of anisotropic diffusion, which is characterised by D_{aa}/D_{bb}, can definitely be affected by the aspect ratio. Ellipsoidal particles with $aa/L_f > 1$ always have the major axes as the preferential diffusing direction, while ellipsoidal particles with $aa/L_f < 1$ tend to travel along their minor axis statistically. Since aspect ratio γ is defined as bb/aa, the effect of the aspect ratio indicates that the size of the minor axis (bb) is not a parameter which controls the particle's preferential diffusing direction.

A summary of the relationship between D_{aa}/D_{aa} and aa/L_f is shown in Figure 3.7 for all experimental conditions. The dashed line is a reference for isotropic diffusion, where $D_{aa} = D_{bb}$. Two distinct regions of turbulent diffusion related to size ratio aa/L_f can be identified: (1) If $aa > L_f$, which is above the reference line, $D_{aa}/D_{bb} > 1$, ellipsoids are more likely to diffuse along the major axes. (2) If $aa < L_f$, which is below the reference line, $D_{aa}/D_{bb} < 1$, indicating that the ellipsoids prefer to travel along the minor axes. The effect of size ratio on the degree of anisotropy is consistent with the results shown in Figure 3.6 (b).

Unexpectedly, these findings also suggest that when $aa = L_f$ ($aa = 3$mm and $L_f = 3$mm in the Figure), the diffusion of ellipsoids with different aspect ratios ($\gamma = 0.25$, 0.5 and 1) is isotropic. All of these ellipsoidal particles diffuse like a circular disc for
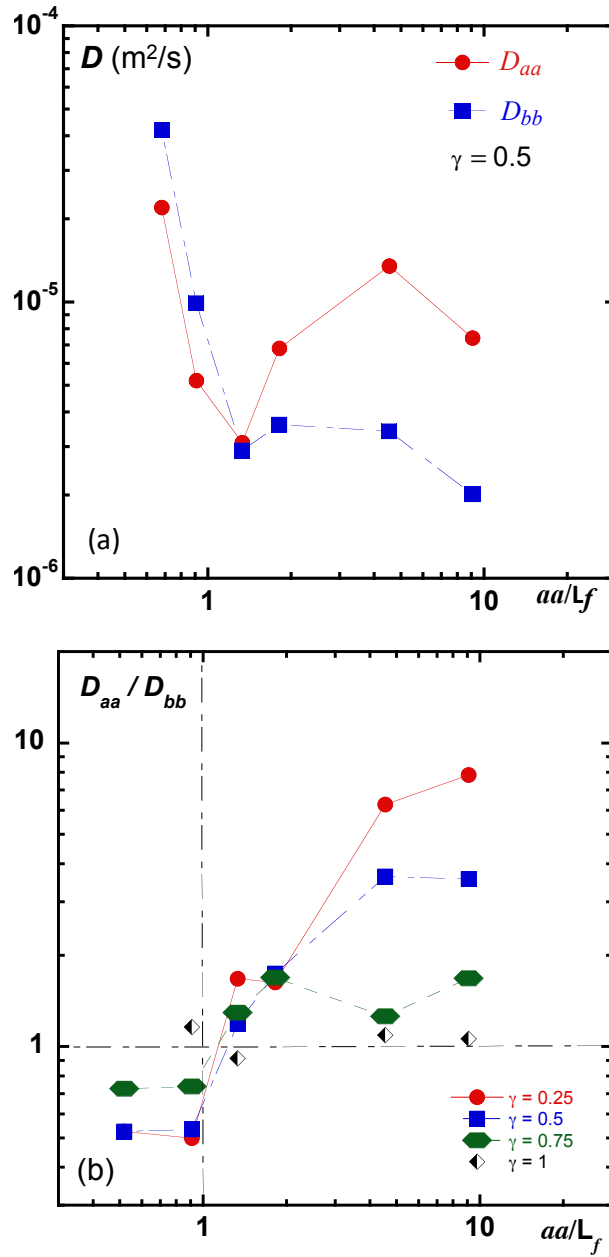
Figure 3.6: (a) The effect of size ratio on the decomposed diffusion coefficients in the body frame of reference D_{aa} and D_{bb}. $\gamma = 0.5$ for all particles; (b) The effect of size ratio on the ratio of the decomposed diffusion coefficient D_{aa}/D_{bb}, $\gamma = 0.25, 0.5, 0.75$ and 1.

which $D_{aa} \approx D_{bb}$. This result further emphasises the importance of size ratio aa/L_f.

The Green-Kubo relation is applied to study the decomposition diffusion coefficients in the body frame of reference [130, 40, 54]. The transport diffusion coefficient D is the integral of the Lagrangian velocity auto-correlation function.
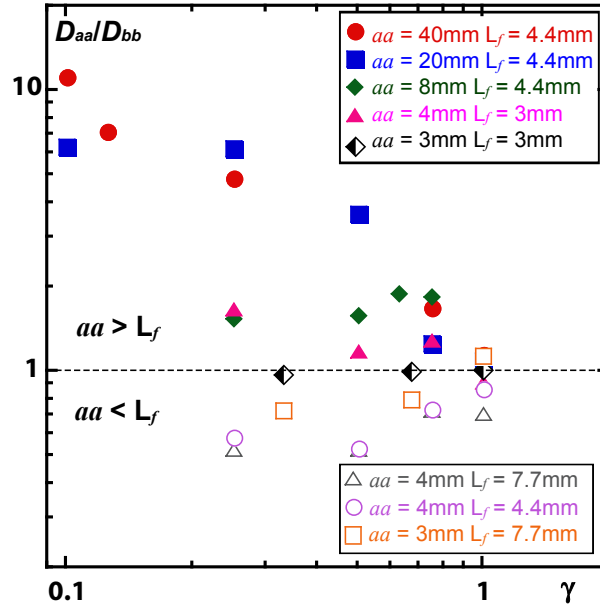
Figure 3.7: Summary of the D_{aa}/D_{bb} for all experimental conditions. The dashed line is the reference for which D_{aa}/D_{bb} = 1. The region above the reference shows $aa >$ L_f, while the region below the reference indicates $aa < L_f$.

$$D_{aa} = \int_0^\infty \langle v_{aa}(t_0)v_{aa}(t+t_0)\rangle dt = \langle v^2\rangle \int_0^\infty \langle cos(\beta(t_0))cos(\beta(t+t_0))\rangle dt, \qquad (3.3)$$

$$D_{bb} = \int_0^\infty \langle v_{bb}(t_0)v_{bb}(t+t_0)\rangle dt = \langle v^2\rangle \int_0^\infty \langle sin(\beta(t_0))sin(\beta(t+t_0))\rangle dt, \qquad (3.4)$$

where v_{aa} and v_{aa} represent the one-dimensional velocity vectors, $\langle v^2\rangle$ is the kinetic energy of the particle.

By taking the angle difference between the the velocity direction of the particle and its major axis as β, and assuming the correlation between velocity magnitudes and velocity directions is small [80], equation (3.3) and (3.4) can be rewritten as:

$$D_{aa} = \langle v^2 \rangle \int_0^\infty \langle \cos(\beta(t_0))\cos(\beta(t+t_0)) \rangle dt$$

$$= \langle v^2 \cos^2(\beta(t_0)) \rangle \int_0^\infty v^2 \cos(\beta(t_0))\cos(\beta(t)) dt$$

$$= \langle (v_{aa})^2 \rangle \int_0^\infty \boldsymbol{v_{aa}}(t_0)\boldsymbol{v_{aa}}(t) dt,$$

$$D_{bb} = \langle v^2 \rangle \int_0^\infty \langle \sin(\beta(t_0))\sin(\beta(t+t_0)) \rangle dt$$

$$= \langle v^2 \sin^2(\beta(t_0)) \rangle \int_0^\infty v^2 \sin(\beta(t_0))\sin(\beta(t)) dt$$

$$= \langle (v_{bb})^2 \rangle \int_0^\infty \boldsymbol{v_{bb}}(t_0)\boldsymbol{v_{bb}}(t) dt,$$

where $\int_0^\infty \boldsymbol{v_{aa}}(t_0)\boldsymbol{v_{aa}}(t)dt$ and $\int_0^\infty \boldsymbol{v_{bb}}(t_0)\boldsymbol{v_{bb}}(t)dt$ are the integral time scale of the auto-correlation function of the Lagrangian velocity components, T_{aa} and T_{bb}. If we take the ratio of the diffusion coefficients,

$$\frac{D_{aa}}{D_{bb}} = \frac{\langle v_{aa}^2 \rangle}{\langle v_{bb}^2 \rangle} \cdot \frac{T_{aa}}{T_{bb}}. \tag{3.5}$$

$\langle v_{aa}^2 \rangle / \langle v_{bb}^2 \rangle$ characterises the ratio of energy transfer from the turbulence flow to the ellipsoidal particles along the two axes. The ratio of the relation time, T_{aa}/T_{bb}, represents the rate at which energy dissipates in the body frame of reference.

To test whether there is a dominant influence of the anisotropic shape on the dissipation rate or on the energy transfer, we analyse the time scale of the dissipation and the kinetic energy of the particle in the body frame of reference at different size ratios of the ellipsoids, as shown in Figure 3.8 (a) and (b).

For a circular disc ($\gamma = 1$), T_{aa}/T_{bb} remains around 1, indicating that there is no anisotropy effect on the dissipation. For ellipsoidal particles whose aspect ratio $\gamma \neq$ 1, two regimes are identified. T_{aa}/T_{bb} for **small** ellipsoids are persistently lower than 1, which means it will take longer for the particle to dissipate its energy along the minor axis (bb) than the major one (aa). When $aa/L_f > 1$ for which the particles are considered to be **large**, $T_{aa}/T_{bb} > 1$. This latter type of particles spend more time
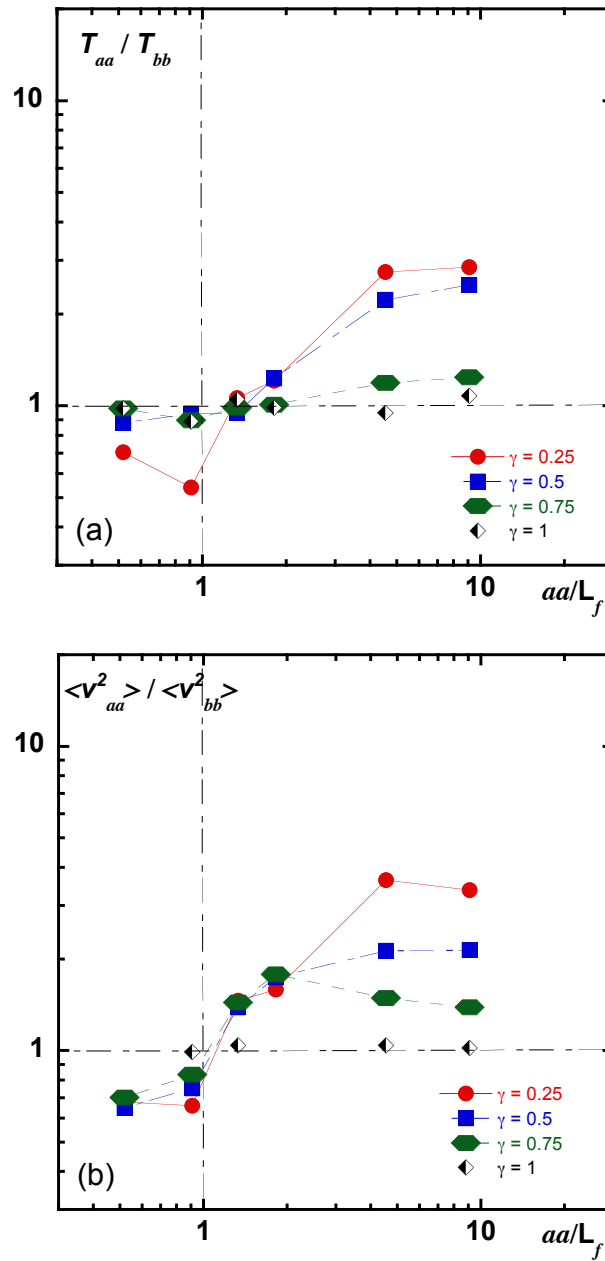
Figure 3.8: (a) The ratio of correlation time scales along the two axes in the body frame of reference T_{aa}/T_{bb}; (b) Energy transfer from the turbulent flow to the particle along the two axes in the body frame of reference $\langle v_{aa}^2 \rangle / \langle v_{bb}^2 \rangle$.

travelling in the direction parallel to their major axes.

Figure 3.8 (b) represents the effect of size ratio on $\langle v_{aa}^2 \rangle / \langle v_{bb}^2 \rangle$. More energy is accumulated along the major axis of the particle ($\langle v_{aa}^2 \rangle / \langle v_{bb}^2 \rangle > 1$) if the ellipsoids are *large*. On the other hand, $\langle v_{aa}^2 \rangle / \langle v_{bb}^2 \rangle < 1$ for all *small* ellipsoids. The analyses show that both the dissipation rate (T_{aa}/T_{bb}) and the energy transfer from the turbulence

to the particle (v_{aa}^2/v_{bb}^2) change similarly with the change of the size ratio of the ellipsoids.

From the results above, it can be seen that the size ratio aa/L_f is the parameter that determines the anisotropy of the diffusion or the preferential diffusing direction of ellipsoids in 2D turbulence. In the following contexts, an ellipsoid is classified as a *large* particle if $aa/\mathrm{L}_f > 1$; *large* particles prefer to move along their major axes. An ellipsoid with $aa/\mathrm{L}_f < 1$ is referred to as a *small* particle. The preferential diffusing direction of *small* ellipsoids is along its minor axis.

3.3   Orientational dynamics of ellipsoids

To further characterise the observed anisotropy of the diffusion coefficients, we turn to the orientational dynamics of the ellipsoids. We measure the orientation of the ellipsoid (θ_{aa}) and the direction of the instantaneous velocity (θ_v) of the ellipsoid in the lab frame of reference. The angular difference, $\Delta\theta = |\theta_{aa} - \theta_v|$, which is similar to the angle of attack (AOA) in aerodynamics, is used to characterise the preferential diffusion of the particles. Since an ellipsoidal particle has two axes of symmetry, the range of $|\theta_{aa} - \theta_v|$ is from $0°$ to $90°$. If an ellipsoid moves along the direction of the major axis, the relative orientation angle of the ellipsoid, $\Delta\theta = |\theta_{aa} - \theta_v| \approx 0°$, while $\Delta\theta = |\theta_{aa} - \theta_v| \approx 90°$ corresponds to the transverse motion of the ellipsoid.

As shown in the previous sections, *large* ellipsoids prefer to move along their major axes, while *small* ellipsoids have a tendency to diffuse along their minor axes. The probability density functions (PDFs) of the AOA are in good agreement with our previous findings. Initially, PDFs for particles of different sizes (aa = 4mm and 40mm) are shown in Figure 3.9 (a) with a turbulent flow forced at L_f = 4.4 mm. Here, a 4 mm ellipsoid is considered as *small* while a 40 mm one is *large*. For *large* ellipsoids, the PDF peaks at $\Delta\theta = |\theta_{aa} - \theta_v| = 0°$ and deceases gradually with the increase of the AOA. This indicates a higher probability that the orientation of the particle
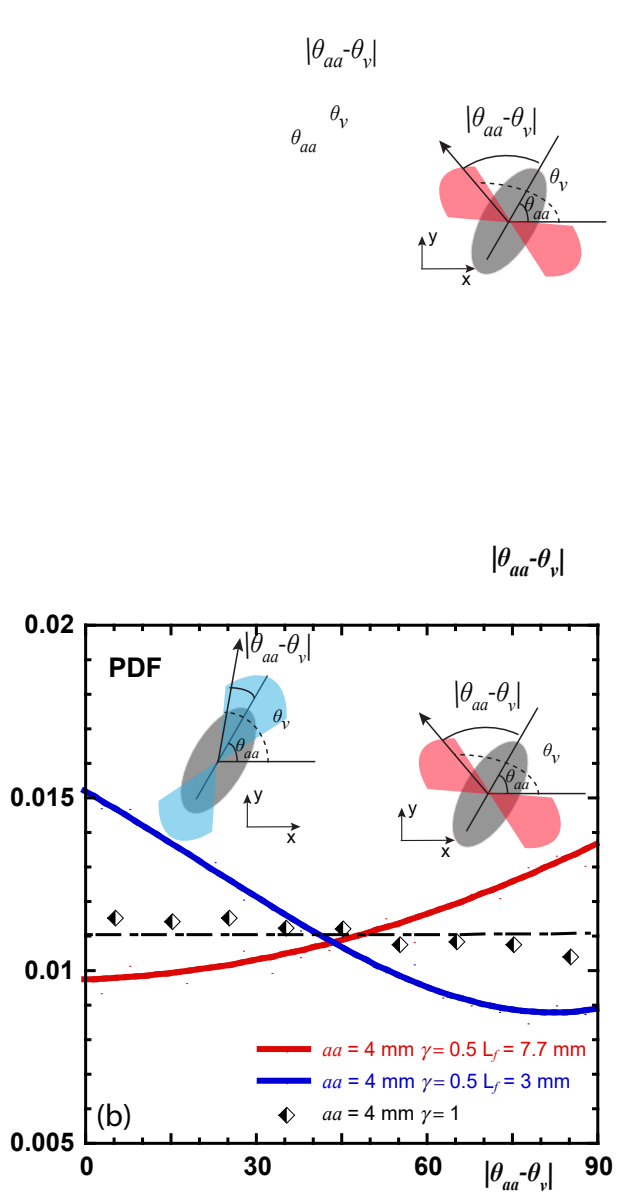
Figure 3.9: Probability Density Function of angle of attack ($|\theta_{aa} - \theta_v|$) (a) 4 mm ellipsoid and 40 mm ellipsoids with γ = 0.5 in flow with L_f = 4.4 mm; (b) 4 mm ellipsoid with γ = 0.5 in flows with L_f = 7.7 mm and L_f = 3 mm

will be aligned with the direction of the moving velocity, which is a reflection of the movement being predominantly in the direction of the major axes. The PDF of *small* ellipsoids peaks at $\Delta\theta = |\theta_{aa} - \theta_v| = 90°$, which means the ellipsoids prefer to move in the transverse direction of the major axes, see Figure 3.9(a). Similar results are are obtained for same size ellipsoid (aa = 4 mm) in different flow conditions, as shown in Figure 3.9(b). Here, the *small* particle is a 4 mm ellipsoid in the flow with forcing scale L_f = 7.7 mm, while the *large* particle is a 4 mm ellipsoid in the flow with forcing
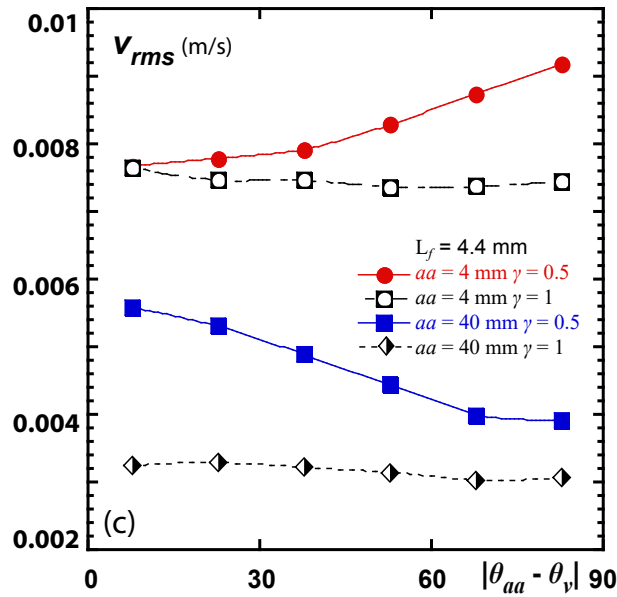
Figure 3.10: The r.m.s velocities of ellipsoids for different angles of attack $\Delta\theta = |\theta_{aa} - \theta_v|$, the flow is driven at f = 60 Hz , L_f = 4.4 mm

scale L_f = 3 mm. The insets in Figure 3.9 (a) and (b) show the predominant angular excursions of the diffusing direction of particles, where **large** particles are marked in blue and **small** particles are marked in red. As a reference, the PDFs of AOA for circular discs do not shown any peaks and the values remain flat within the range from 0° to 90°, showing no anisotropy of the diffusion coefficient.

Furthermore, the r.m.s of the translational velocities of ellipsoids with respect to the AOA is studied to characterise the relation between the translation and orientation of the particle. The results are shown in Figure 3.10. Similar to the PDFs of AOA, the r.m.s. velocity for the circular discs remains constant from AOA = 0° to AOA = 90°, as expected. For **small** particles (4 mm ellipsoid in the flow with L_f = 4.4 mm), v_{rms} continues to increase with the increase of AOA and peaks at AOA = 90°. This is a reflection of **small** ellipsoids having a higher velocity when diffusing transversely. However, for **large** particles (40 mm ellipsoid in the flow with L_f = 4.4 mm), v_{rms} shows a decreasing trend in the same range, which means this particle diffuses faster along its major axis.

Combining the results of PDF of AOA and v_{rms}, the statistical analysis on both

translational and rotational diffusion further suggests that (1) the ratio aa/L_f is the key parameter that determines the turbulent transport of ellipsoids; and (2) ellipsoids not only have preferential diffusing directions in turbulent flows, but also have correspondingly higher velocities when travelling in the preferred direction.

3.4 Interaction between ellipsoids and the underlying flow

To gain further insights into the dynamics of ellipsoids, we plot the trajectories of the ellipsoids with reference to both position and orientation. In the same flow condition where f = 60 Hz and L_f = 4.4 mm, the motions of a 4 mm and a 40 mm ellipsoid are tracked for 60 seconds. The particle trajectories are illustrated in Figure 3.11 (a) and (b), respectively. Both particles have the same aspect ratio γ = 0.5. The time intervals between two consecutive positions of ellipsoids are 0.05 s for Figure 3.11 (a), and 0.1 s for Figure 3.11 (b). The symbols are calibrated to represent the actual sizes and the orientations of the ellipsoids. The r.m.s. translational velocity of the particle (v_{rms}) is also taken into consideration. The trajectories are colour-coded according to the magnitude of the r.m.s velocity, where orange-red means higher velocity and black-blue is lower velocity.

For a ***small*** ellipsoidal particle (aa = 4 mm, forcing scale L_f = 4.4 mm), the trajectory exhibits a 'flight-trap' behaviour, as shown in Figure 3.11 (a). Particles 'fly' from one spot to another with higher velocity during the flight period. It is also clear that the ***small*** ellipsoid mostly travels transversely with higher v_{rms}, which forms straight sections in its trajectory. This 'flight' behaviour is always followed by 'trap' behaviour. During the 'trap' period, the ***small*** particle rotates erratically and its position fluctuates slowly, which results in a small value of the translational velocity v_{rms}, as seen in the black-blue areas. The observation of v_{rms} during the flight period, when the particle is travelling in the preferential diffusing direction, is consistent with the results
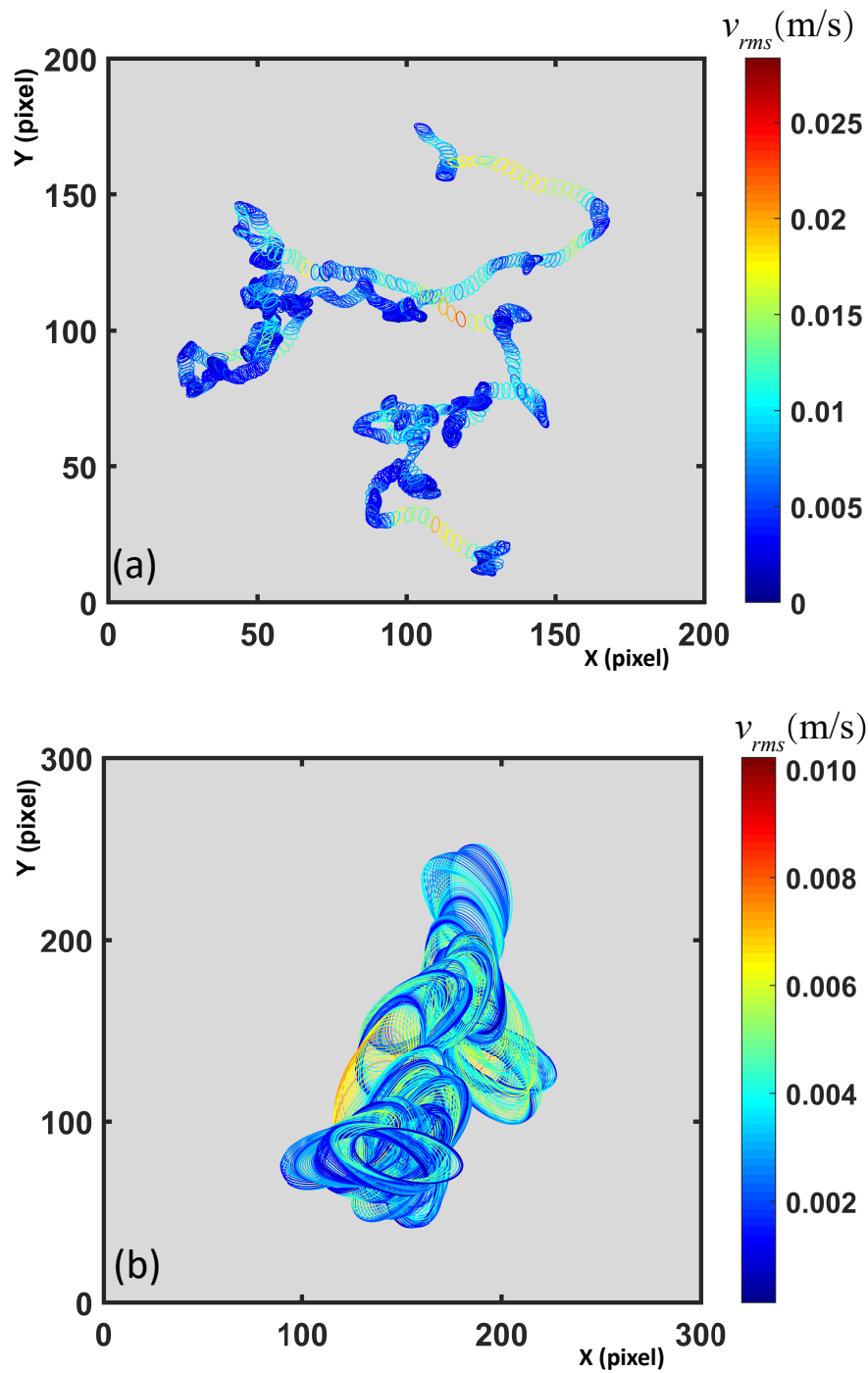
Figure 3.11: (a) A typical trajectory of a 4 mm ellipsoidal particle. The trajectory is recorded for a total time of 60 s with a time interval between adjacent images of 0.05s; (b) A typical trajectory of a 40 mm ellipsoidal particle. The trajectory is recorded for 60 s with time interval between adjacent images of 0.1 s. Both ellipsoids have the same aspect ratio $\gamma = 0.5$. Both trajectories are recorded in the flow forced at $L_f = 4.4$ mm.

shown in Figure 3.10.

The trajectory of a *large* ellipsoid is illustrated in Figure 3.11 (b), where the size of the ellipsoid aa = 40 mm and forcing scale L_f = 4.4 mm. Both the translation and rotation of the *large* particle show strong fluctuation, and its overall behaviour is reminiscent of the random walk of a Brownian ellipsoid.

To gain further insights into the particle dynamics, further attention is paid to the coupling between the flow and the particle. It is of interest to figure out why the *small* ellipsoidal particle exhibits the unexpected behaviours. We visualise the underlying flow structure by seeding 50 μm tracer particles in the fluid flow together with the ellipsoidal particle. Three time-averaged images of a 3mm ellipsoid diffusing in a flow forced at L_f = 4.4 mm are presented in Figure 3.12 (b) to (d). The corresponding relative orientation (AOA; red curve) and the r.m.s. velocity (v_{rms}; blue curve) are shown in Figure 3.12 (a). Two different regimes are identified, specifically (1) a flight regime (time interval marked as I and III; blue-shaded) and a trap regime (time interval II; pink-shaded).

During the flight events (time interval I and III), the ellipsoid's translational velocity is aligned along its minor axis and its AOA remains high, where $\Delta\theta \approx 90°$. In the same time period, the translational velocity gradually increases, as seen in the blue curve in Figure 3.12 (a) in the blue shaded areas. There is a delay in the increment of velocity, for the reason that the particles will be coupled with the flow and modify their relative orientation first. Both Figure 3.12 (b) and (d) show the identical temporal evolution of both particles and flow in the flight regime.

One distinct feature that can be observed from Figure 3.12 (b) and (d) is the coherent bundle, which has been described in previous studies [116, 36]. The time-averaged tracer particles travel together and form a bundle structure that can be clearly observed in the Figure (dashed line). The width of the bundle is close to the size of the forcing scale of the flow for which d = L_f = 4.4 mm. The arrows indicate the flowing direction of the corresponding bundle. It is seen that the *small* ellipsoids are transported within the bundle structure, and that the orientations of the ellipsoids are
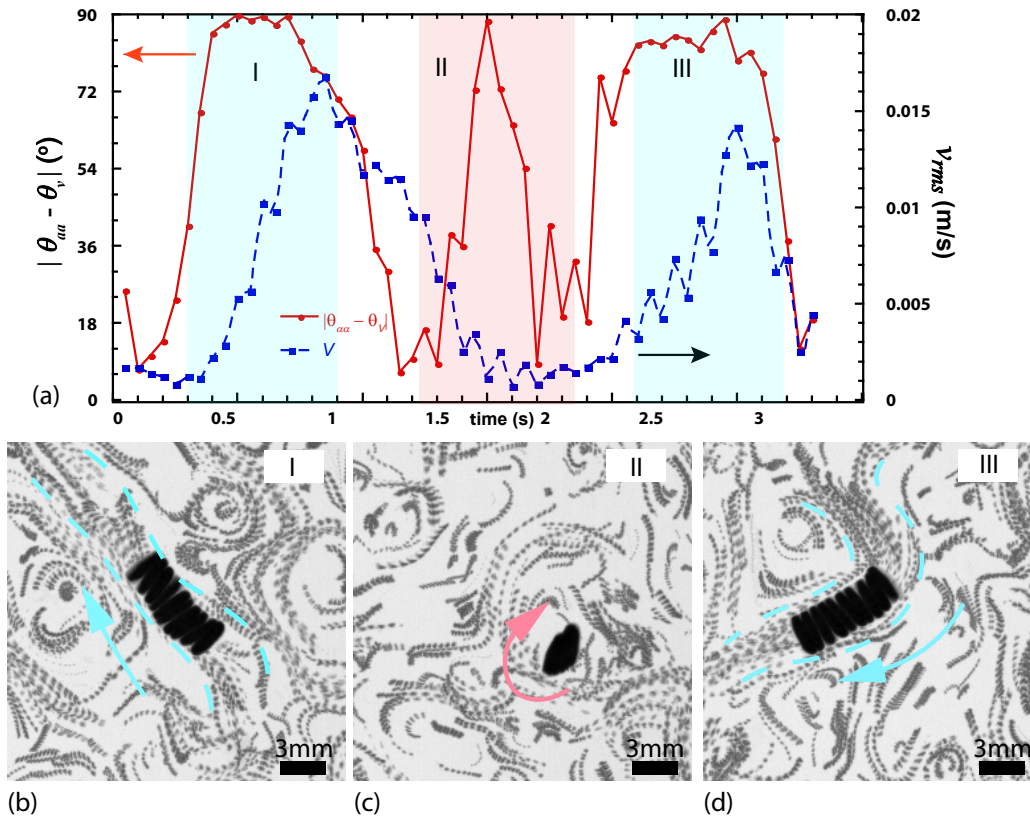
Figure 3.12: (a) Temporal evolution of the translational velocity (blue dashed line) and the relative orientation of the particle ($|\theta_{aa} - \theta_v|$) (red solid line) for the 3 mm ellipsoid with $\gamma = 0.33$, and flow is forced at $L_f = 4.4$ mm. The three images (overlapping images of the ellipsoid and the surrounding tracer particles) show the flight and trap events corresponding to the time intervals: (b) I; (c) II; and (d) III. The dashed blue lines in (b) and (d) highlights the contour of the river-like structure that carries the small ellipsoid.

always perpendicular to the bundles flow direction. This is because the ellipsoid is pushed along the minor axis by groups of fluid particles within the bundle structure.

As described in the references [116, 36], the coherent bundles have a finite life time due to their constant interaction with surrounding bundles. They may also split into smaller bundles occasionally. This means that an ellipsoid is only carried by the bundle for a finite time. After that, the ellipsoid stays trapped at a fixed location. An illustration of a trap event is shown in Figure 3.12(a) (pink-shaded area) and in Figure 3.12(c). The translational velocity of the ellipsoid decreases and stays low during the trap events, while the AOA fluctuates in the range of 0 ° to 90 ° due to the erratic rotation of the ellipsoid around the trapping point locally.

Since the flow consists of constantly interacting bundles, an ellipsoid in a trapping regime can escape the trap due to the impact of a coherent bundle. This de-trapping event leads to another flight event. The most efficient de-trapping events occur when a bundle impacts the ellipsoid transversely along its minor axis. This phenomenology of short trap - long flight events is consistent with the fact that *small* ellipsoids move principally along their minor axes.

3.5 Coupling between translational and rotational motion

The alignment of the ellipsoids with their velocity vectors is governed by a coupling between their translational and rotational motion. A dimensionless mixed cross-correlation function (MCC) C(t) [79] was proposed to characterise such coupling:

$$C(t) = \frac{\Delta r'_x(t) \Delta r'_y(t) \sin(2\theta'_{aa}(t))}{\langle \Delta r^2 \rangle}. \tag{3.6}$$

Here, $\Delta r'_x(t)$ and $\Delta r'_y(t)$ are the displacements of a particle from the initial position in the lab frame of reference at time t. $\theta'_{aa}(t)$ is the orientation of the ellipsoidal particle. $\langle \Delta r^2 \rangle$ is the total MSD. These parameters are marked with a "'" to distinguish them from the usual definition. Given this characterisation, all particles are set to diffuse from the origin position at $(0, 0)$ with an initial orientation $\theta'_{aa}(t_0) = 0°$. The schematics of the calibration for both translation and rotation diffusion are shown in Figure 3.13 (a) and (b).

In these Figures, a new lab coordinate is created based on the initial orientation of the ellipsoids at time t_0. The displacement components in the new reference $\Delta r'_x(t)$ and $\Delta r'_y(t)$ are calculated from the ellipsoidal particle's position at time t relative to
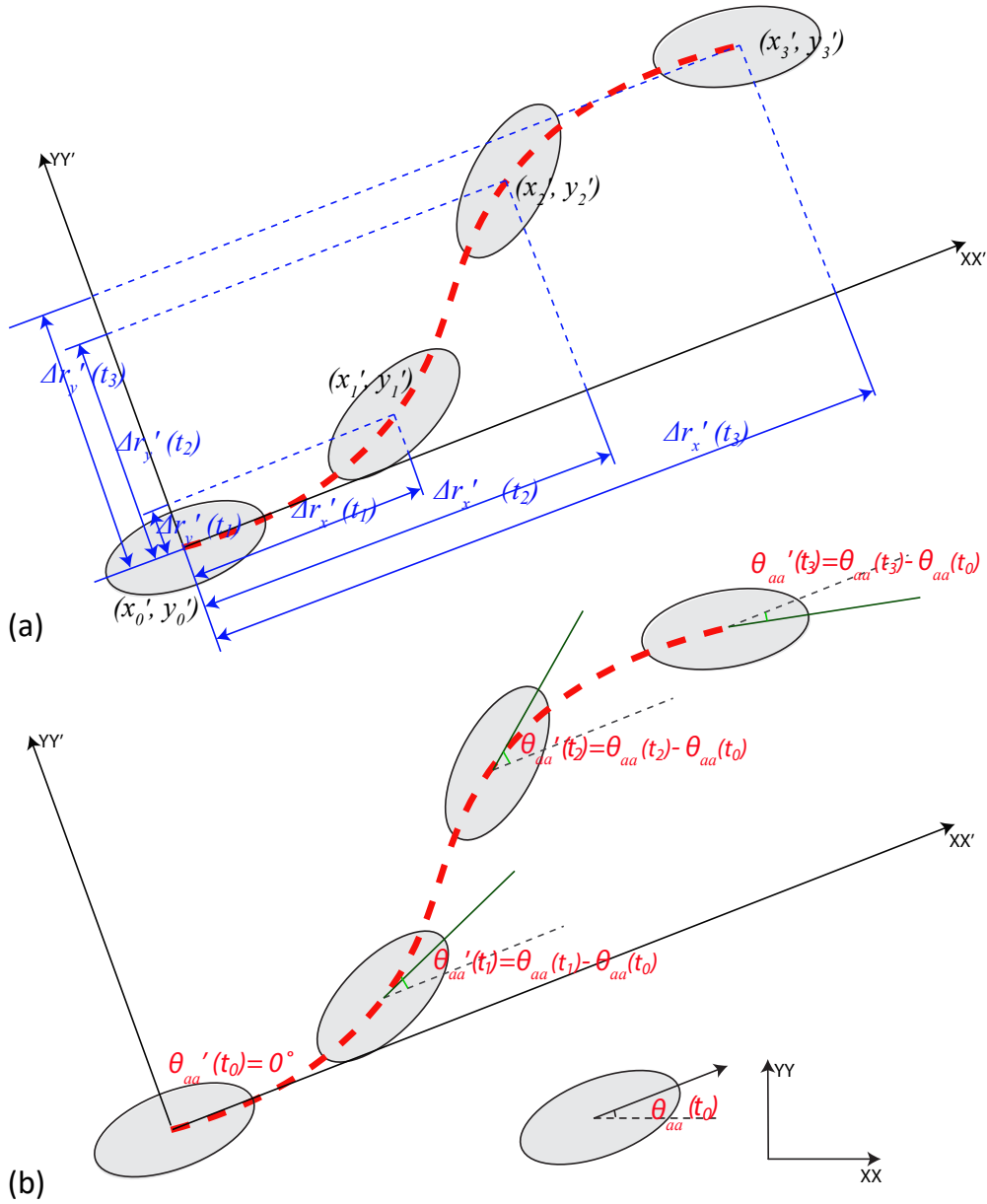
Figure 3.13: The schematics of calibration for both translational and rotational motion of ellipsoids. (a) Translational displacements of ellipsoids in the new lab frame of reference; (b) Rotational orientations of ellipsoids in the new lab frame of reference.

the origin of the coordinate, with the relation read as:

$$
\begin{bmatrix} \Delta r'_x(t) \\ \Delta r'_y(t) \end{bmatrix} = \begin{bmatrix} \cos\theta'_{aa}(t) & \sin\theta'_{aa}(t) \\ -\sin\theta'_{aa}(t) & \cos\theta'_{aa}(t) \end{bmatrix} \times \begin{bmatrix} x_t - x_0 \\ y_t - y_0 \end{bmatrix}
$$

where $\Delta r_x^2(t) + \Delta r_y^2(t) = \Delta r^2(t) = \Delta r'^2_x(t) + \Delta r'^2_y(t)$.

The corresponding rotational orientation of the ellipsoid in the new lab frame of reference is shown in Figure 3.13 (b). The inset illustrates the definition of the initial orientation at time t_0 as $\theta_{aa}(t_0)$ in the lab frame of reference. After calibration, the new initial orientation $\theta'_{aa}(t_0) = 0°$ and the consecutive orientations are calculated as $\theta'_{aa}(t) = \theta_{aa}(t) - \theta_{aa}(t_0)$ with range between -90° and +90°.

The mixed cross-correlation function (MCC) gives a statistical ensemble average of the coupling between the translational and rotational motion of the particle. When an ellipsoid diffuses along its major axis, it leads to a positive coupling $\langle \Delta r'_x(t) \Delta r'_y(t) \sin 2\theta'_{aa}(t) \rangle$ > 0 (see schematic trajectory shown in the inset of Figure 3.14 (a)). Alternatively, a negative mixed cross-correlation function, $\langle \Delta r'_x(t) \Delta r'_y(t) \sin 2\theta'_{aa}(t) \rangle < 0$, indicates that the ellipsoid translates along the minor axis (see schematic trajectory in the inset of Figure 3.14 (b)).

The MCCs for two ellipsoids (aa = 40 mm and 4 mm, γ = 0.5) and a circular disc (aa = 40 mm, γ = 1) under the same flow conditions (L_f = 4.4 mm) are shown in Figure 3.14 (a). In the case of a circular disc, $C(t)$ is close to neutral across the whole time range, as would be expected for a particle with independent translational and rotational degrees of freedom. For ellipsoids, although $C(t)$ deviates from zero for both ellipsoids at t_0 (which indicates no coupling initially), the non-zero values of $C(t)$ afterwards indicates some extent of coupling between the two degrees of freedom either positive or negative. *Large* ellipsoidal particles (aa = 40 mm, L_f = 4.4 mm and aa/L_f > 1) exhibit positive coupling $C(t) > 0$, which means these particles travel longitudinally along their major axes, while *small* ellipsoidal particles (aa = 4 mm, L_f = 4.4 mm and aa/L_f < 1) have a negative coupling $C(t) < 0$, since their motions are most often along the minor axes. A similar transition from positive to negative coupling can also be achieved with the change of aa/L_f, as shown in Figure 3.14 (b). In this Figure, the case of aa = 4 mm and L_f =3 mm represent for *large* particle, while aa = 4 mm and L_f =7.7 mm presents a *small* particle.
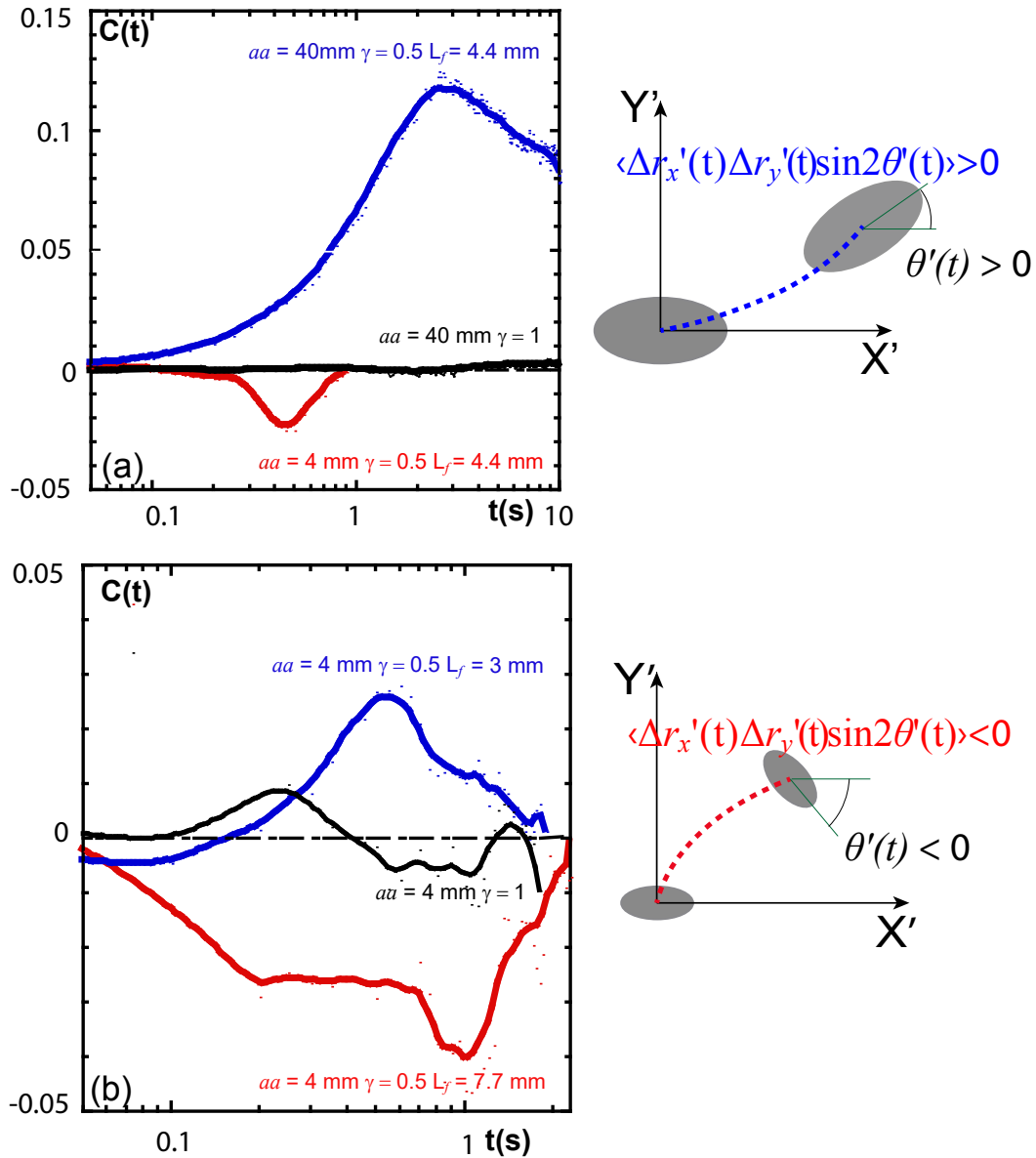
Figure 3.14: Mixed cross-correlation function (MCC) for ellipsoidal particles and circular discs at different experimental conditions. (a) 4 mm ellipsoid and 40 mm ellipsoid with $\gamma = 0.5$ at $f = 60$ Hz; (b) 4 mm ellipsoid with $\gamma = 0.5$ at $f = 30$ Hz and $f = 120$ Hz. Circular discs are shown as references

The negative coupling is considered to be *anomalous*, as described in the experiments that used bacterial suspensions [79], since the coupling is always positive for Brownian ellipsoid [42]. Our observations on the MCCs of the ellipsoids constitute further evidence that a **small** ellipsoid is advected by turbulence that moves principally along a direction parallel to its minor axis.

3.6   Discussion

In our experiments, we study the dispersion of ellipsoidal particles of finite size, from 0.3 L_f to 10 L_f, in 2D turbulence. As mentioned in the introduction, the motion of finite-size particles in this range and the anisotropic shape make this problem very difficult to solve numerically. In the experiments that have been performed, we discovered a transition from positive to negative coupling of the translational and rotational dynamics of ellipsoids by altering the size ratio, aa/L_f. This behaviour can be attributed to the interaction of the finite-size ellipsoids with the underlying coherent structures that exist in the underlying turbulent flow. The aspect ratio γ of the particle is not a critical parameter in controlling the preferential diffusing direction.

The results of this study allow interesting analogies to be drawn between the turbulent transport of ellipsoids and the behaviour of microscopic ellipsoids placed in a thermal bath or in bacterial turbulence.

3.6.1   *Large* ellipsoidal particles

Particles tend to diffuse in the direction parallel to their major axes when the size of the major axis is greater than the size of the forcing scale of the flow, $aa > L_f$. In a fluid flow with coherent bundles of width close to L_f, these *large* particles interact with multiple underlying coherent bundles. It has been shown that large circular discs exhibit a Brownian-like motion when interacting with multiple bundles [119]. This interaction with many degrees of freedom might be the source of the Brownian-like ellipsoid behaviour.

The Brownian motion of a particle in a thermal bath has been investigated extensively [48, 81]. The motion of ellipsoidal tracer particles is considered to be governed by two friction factors: ξ_{aa} along the major axis (aa) and ξ_{bb} along the minor axis. In theory, ξ_{bb} is significantly larger than ξ_{aa} due to anisotropic shapes, which results in a higher diffusion coefficient along the major axis ($D_{aa} > D_{bb}$) [42, 41, 128]. The preferential

diffusion direction of such ellipsoidal particles in fluids is along their major axis. The anisotropic diffusion of ellipsoidal particles has also been confirmed in experiments of quasi-two-dimensional confinement in a 1μm thin sheet of water. At short time-scale, it was found that $D_{aa} > D_{bb}$ [42].

In our experiments, as shown in Figure 3.8 (a) and (b), the anisotropic diffusion of ellipsoidal particles in 2D turbulence ($D_{aa}/D_{bb} > 1$) is a result of the anisotropy in both the energy transfer from the flow to the ellipsoids ($\langle v_{aa}^2\rangle/\langle v_{bb}^2\rangle$) and the Lagrangian time scale (T_{aa}/T_{bb}), which is related to the friction time scale.

3.6.2 *Small* ellipsoidal particles

Ellipsoids with the major sizes smaller than the forcing scale ($aa < \mathrm{L}_f$) travel mostly along their minor axes (transverse) in wave-driven turbulence. A ***small*** ellipsoid exhibits a flight-trap behaviour. When the ellipsoid is trapped, it rotates erratically and its position slowly fluctuates. The most efficient de-trapping events occur when a bundle impacts with it transversely along its minor axis. Indeed, the most effective momentum transfer occurs when the minor axis of the ellipsoid is aligned with the velocity vector of the coherent bundle. The traps are followed by long flights events during which the ellipsoid is carried by the fluid bundle. During such flight, the ellipsoid moves transversely and gains a substantial amount of kinetic energy. The flight event is followed by another trap event due to the finite lifetime of the bundle. This sequential phenomenon is consistent with the statistical description of the turbulent transport of small ellipsoids. In this experiment, the Brownian effect is negligible because the size of our ellipsoids exceed the sub-micrometer scale for Brownian motion.

Our observation of the *anomalous* diffusion of ***small*** ellipsoids is similar to what has been reported when an isolated ellipsoidal particle diffuses in bacterial flows [79, 126]. If the bacterial density is above a certain threshold, a negative coupling of the translational and orientational dynamics arises: the microscopic ellipsoid moves principally along its minor axis. These unusual diffusion dynamics are attributed to the

dipole flow feature generated by pusher-type active bacteria. For dense suspensions of bacterial flows, the collective behaviour of bacteria resembles a swarming motion, which is caused by small-scale interactions when bacteria swim together [67, 23, 112, 94, 24]. This property of bacterial suspensions may be similar to the Lagrangian bundle structure found in the laboratory 2D turbulent flows. Further studies of this comparison would need to be conducted in future experiments to positively confirm such analogy.

Passive propulsion in turbulent flows

Harvesting energy from chaotic flows is always a challenging problem due to the unpredictable and disordered fluid motion. It has recently been demonstrated in the context of wave-driven turbulence that asymmetric floating rotors can tap into the energy of ambient fluctuations to fuel directed rotation [36].

In this chapter, we report experimental results on the dynamics of various asymmetric floating particles capable of passively propelling themselves in biased translational movement in wave-driven 2D turbulence (FWT). We demonstrate experimentally how the shape of a particle and its rotational dynamics conspire to convert the energy of turbulent fluctuations into directional motion. The translation and rotation of the particles are shown to be strongly coupled. This coupling can also be understood with reference to the interactions between the anisotropic particles and the underlying structures of the flow. The propulsion velocity and the rotational motion time-scale depend on the relative size of the particles with respect to the forcing scale of the turbulent flow. The effect of the geometry of the particles on the propulsion has also been investigated and an optimal shape with the strongest propulsion is identified.

The content in this chapter is based on the following journal article: Yang, J.; Davoodianidalik, M.; Xia, H.; Punzmann H.; Shats, M.; and Francois, N., Passive propulsion in turbulent flows, *Physical Review Fluids* 4, 10 (2019), 104608 [124].

4.1   Particle displacements of translation and rotation

Pacman-shaped particles, as described in chapter 2, are studied in this experiment. The pacman-shaped particles are tracked to obtain their positions and orientations. A sample trajectory of a pacman-shaped particle diffusing in 2D turbulence is shown in Figure 4.1 over two consecutive frames. The position of the particle in each frame is marked as $(x(t_i), y(t_i))$, $i = 1$ and 2. The displacements are calculated as $\Delta r_x(t_1) = x(t_2)$ - $x(t_1)$ and $\Delta r_y(t_1) = y(t_2) - y(t_1)$ with corresponding translational velocities of $v_i(t_1)$ = $\Delta r_i(t_1)/\Delta t$, $i = x$ or y. The direction of the velocity $\theta_v(t)$ is along the direction of the total displacement and derived as $\theta_v(t) = \arctan(v_y(t)/v_x(t))$, $\theta_v \in [-180°, 180°]$. The unit vector in the direction of $\theta_v(t)$ is denoted as $\mathbf{n_v}(t)$.
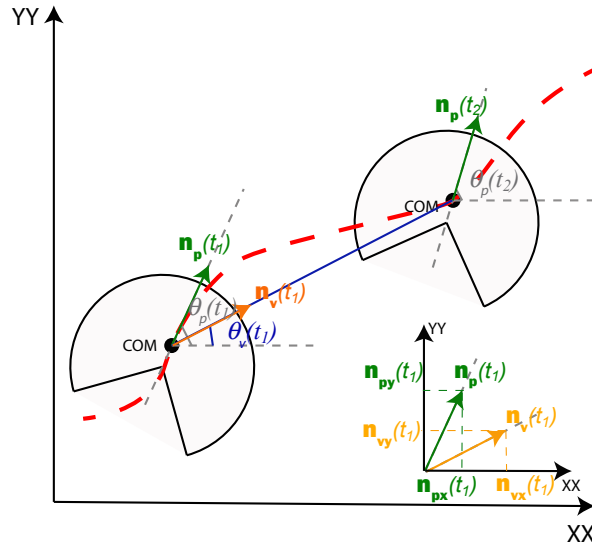
Figure 4.1: A sample trajectory of a pacman-shaped particle in 2D turbulence with two consecutive frames at time t_1 and t_2. The orientation of the pacman-shaped particle θ_p and the direction of the velocity θ_v are shown for each frame. Inset shows the decomposition of the unit vectors in the laboratory frame of reference.

The orientation of the pacman-shaped particle θ_p is along the bisector of the particle (see Figure 4.1). The angular velocity of the pacman-shaped particle is calculated as $\omega_t = \Delta\theta_p(t)/\Delta t$, where $\Delta\theta_p(t) = \theta_p(t_2) - \theta_p(t_1)$ is the angular displacement within this time interval. The unit vector along the orientation of the particle $\theta_p(t)$ is denoted as $\mathbf{n_p}(t)$.

4.2 Translational motion of the pacman-shaped particles

First, a comparison of the translational motion of circular discs and pacman-shaped particles is conducted to demonstrate the effect of anisotropic shapes. The sizes of the circular discs and pacman-shaped particles are in a range of 0.3 L_f to 10 L_f. The cut-out sectors of these pacman-shaped particles are kept at $\alpha = 90°$.

Trajectories of a 20 mm circular disc and a 20 mm pacman-shaped particle in 2D turbulent flows are plotted in Figure 4.2 (a) and (b), respectively. The flow is generated with a forcing scale $L_f = 3$ mm ($f = 120$ Hz). It can be seen that the motion of the circular disc is erratic, similar to the random walk of Brownian particles. However, the motion of a pacman-shaped particle is very different due to its anisotropic shapes. The pacman-shaped particle travels along a trajectory that is almost straight. Moreover, the direction of motion is strongly biased and oriented along the initial orientation of the particle $\mathbf{n_p}(\mathbf{t_0})$, as shown by the arrow in Figure 4.2 (b). As the pacman-shaped particle travels along ballistically, small erratic agitation under the action of the surrounding turbulence can be discovered along the trajectory. The motion of the pacman-shaped particle acts as though it has the ability to propel itself on the wavy surface flow.

By cutting out a 90° sector from a circular disc, the dynamic of a pacman-shaped particle in turbulent wavy flows becomes dramatically different. In order to characterise the trajectories, we calculated the mean-squared displacement (MSD) for both the circular discs and pacman-shaped particles. As shown in Figure 4.3 (a), the MSD of circular discs undergoes a transition from a ballistic regime at short time-scale, where

$$\langle \Delta r^2 \rangle \sim t^2, \quad t \ll T_{disc}, \tag{4.1}$$
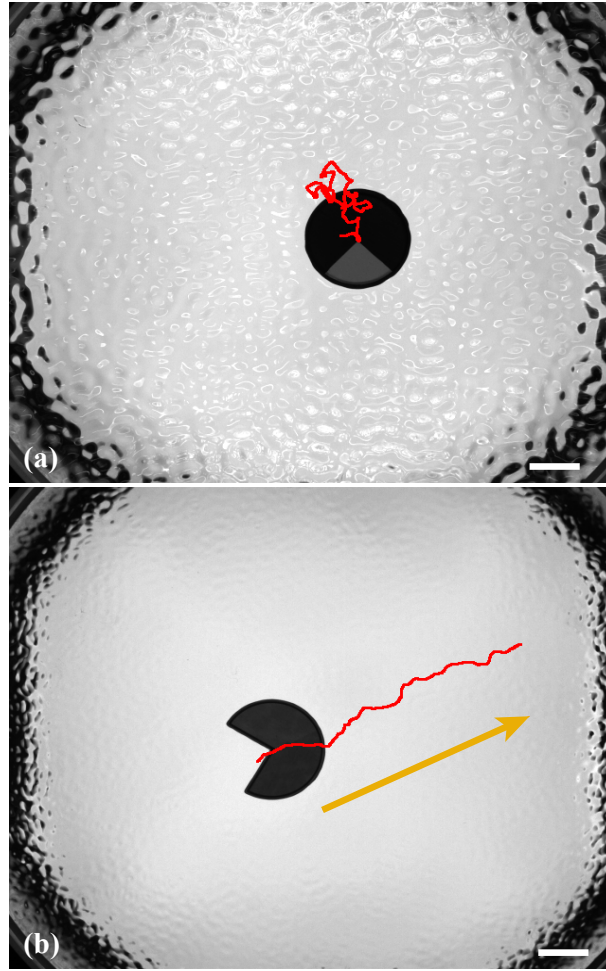
Figure 4.2: Trajectories of particles' locomotion powered by FWT. (a) Trajectory of a circular disc (with a 90° sector painted in grey). The motion of the disc is tracked for 50 s; (b) Trajectory of a pacman-shaped particle. The arrow indicates the direction of movement. The motion of the pacman-shaped particle is tracked for 25 s. The sizes of the particles are kept the same, where r_s = r = 20 mm. The parameters of the turbulent flow are: L_f = 3 mm, f = 120 Hz and r.m.s velocity of fluid particles $\langle u \rangle$ = 2.3 $\times 10^2$ ms^{-1}. Scale bars equal to 20 mm.

to a diffusive regime at longer time-scale, where

$$\langle \Delta r^2 \rangle \sim t, \quad t \gg T_{disc}. \tag{4.2}$$

Here, T_{disc} is the characteristic time obtained by integrating the Lagrangian velocity auto-correlation function (ACF, $\rho(t)$) of a circular disc $\rho(t) = \langle \boldsymbol{u}(t_0 + \Delta t)\boldsymbol{u}(t_0) \rangle / \langle u^2 \rangle$, where $\boldsymbol{u}$ is the velocity vector of the particle and $\langle u \rangle$ is the r.m.s velocity of fluid particles. The turbulent dispersion of a finite-size circular disc in 2D turbulence shows a good agreement with Taylor's dispersion form, which has been discussed earlier [119].
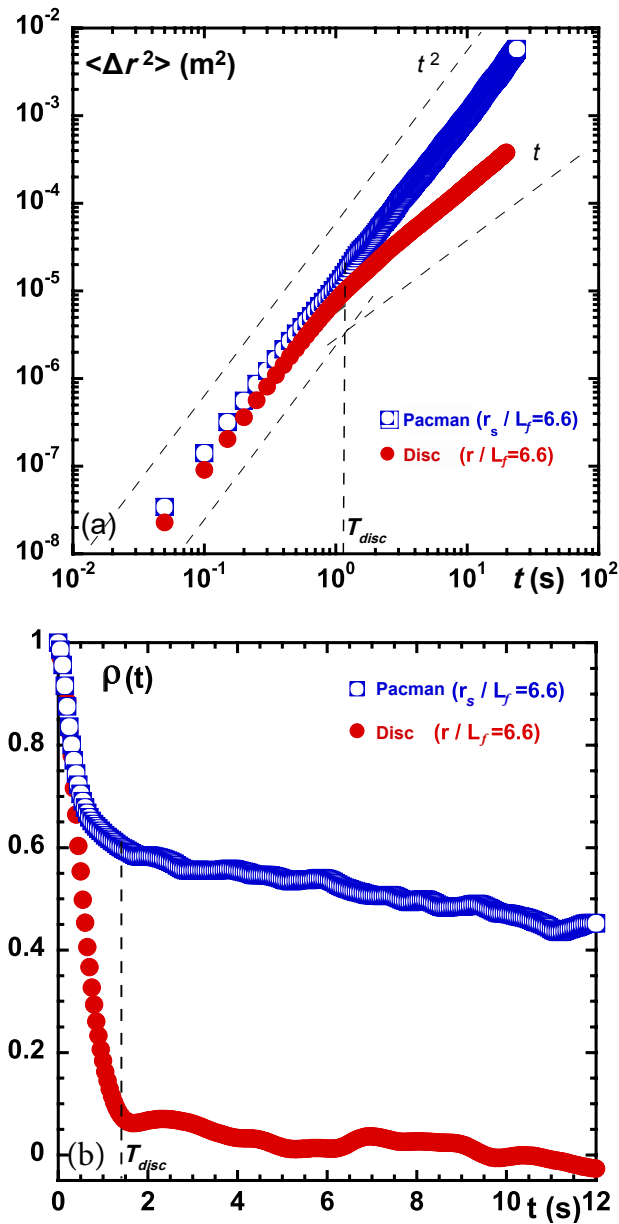
Figure 4.3: (a) Mean-squared displacement (MSD) of circular discs and pacman-shaped particles in FWT. The grey dotted lines indicate the scaling expected for the ballistic and diffusive regimes; (b) Auto-correlation functions ($\rho(t)$) of circular discs and pacman-shaped particles in FWT. The characteristic times for circular discs T_{disc} are shown in both of the plots. Experimental parameters: $r_s = r = 20$ mm for both the circular disc and the pacman-shaped particle, $L_f = 3$ mm, $r_s/L_f = 6.6$.

The corresponding ACF for the circular disc is shown in Figure 4.3 (b), which characterises the process of memory loss during the locomotion of a circular disc. This function decays rapidly as the observation time increases. A sharp decrease is ob-

served in $\rho(t)$ for the first 2 s, after which it fluctuates around 0, which results in T_{disc} being in the order of a second. This behaviour of the MSD and $\rho(t)$ for a circular disc is found to be independent of the forcing scale of the flows. This has been confirmed by altering the driving frequency to change the forcing scale L_f from 3 to 7.7 mm.

In comparison, the MSD of the pacman-shaped particle exhibits only ballistic behaviour ($\langle \Delta r^2 \rangle \sim t^2$) throughout the entire observation period, which constitutes statistical evidence of the strong directional propulsive effect. The dynamics of the pacman-shaped particle are reflected in the ACF $\rho(t)$ as shown in Figure 4.3 (b). Two regimes can be identified: (1) a fast decrease of ρ(t) at short time-scales ($t < T_{disc}$) which is similar to the one observed for a disc. This rapid decrease is followed by (2) a much slower decrease related to the propulsion phenomenon at long time-scales ($t > T_{disc}$), while the value of ACF is higher than 0. Overall, the rapid decrease regime might be related to the turbulent fluctuations and the long slow decay regime is considered to be caused by the propulsion. Competition between these two components determines the motion of pacman-shaped particles in 2D turbulence.

Unlike the circular discs, for which the translational motion is independent of the forcing scale of the flow, the directional motion of the 20 mm pacman-shaped particles can be altered by controlling the flow conditions. Trajectories of same-sized pacman-shaped particles (radius r_s = 20 mm) in flows driven at different forcing scales are shown in Figure 4.4. From (a) to (d), the trajectories of the pacman-shaped particles start with a directional motion when L_f = 3 mm, then become more and more erratic with the increase of L_f. When L_f = 7.7mm, the trajectory of the 20mm pacman-shaped particle is completely random.

The trajectories of pacman-shaped particles can also be controlled by changing the sizes of the particles (r_s) in a fixed fluid flow (L_f = 4.4 mm forced at f = 60 Hz), as shown in Figure 4.5. From (a) to (c), the sizes of the particle (r_s) increase from 20 mm to 40mm, while the corresponding trajectories become more and more directional.
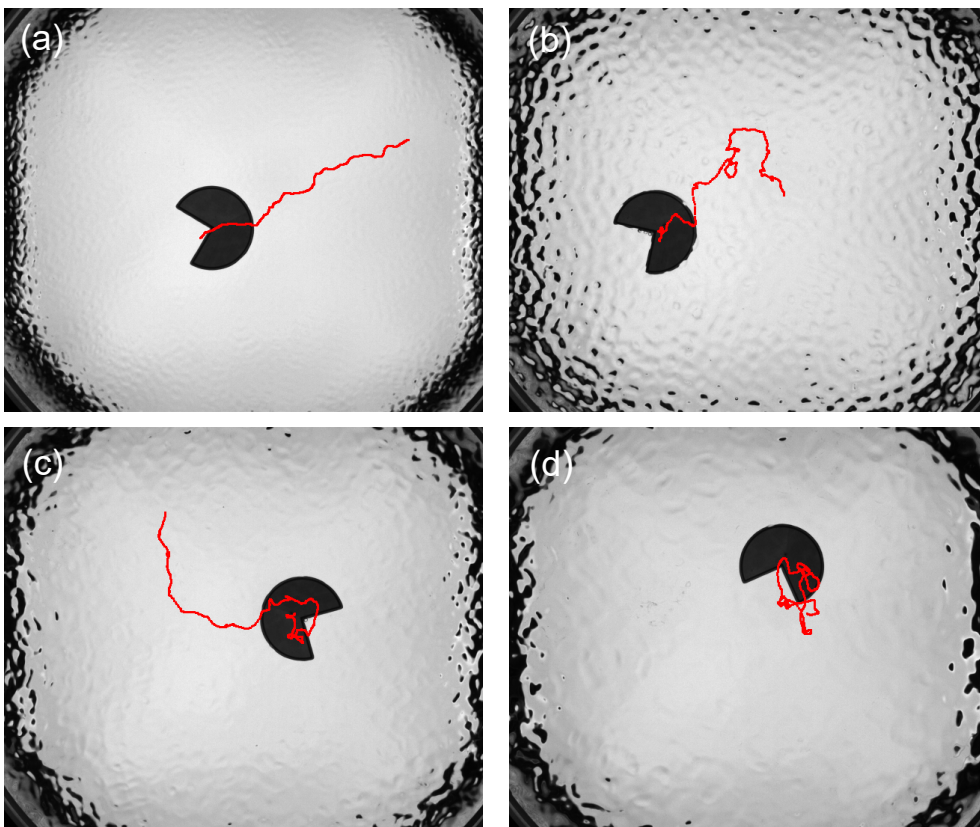
Figure 4.4: Trajectories (red lines) of the pacman-shaped particles (r_s = 20 mm) in turbulent flows with different forcing scales. (a) L_f = 3 mm, r_s/L_f = 6.6; (b) L_f = 4.4 mm, r_s/L_f = 4.55; (c) L_f = 6 mm, r_s/L_f = 3.3; (d) L_f = 7.7 mm, r_s/L_f = 2.5.
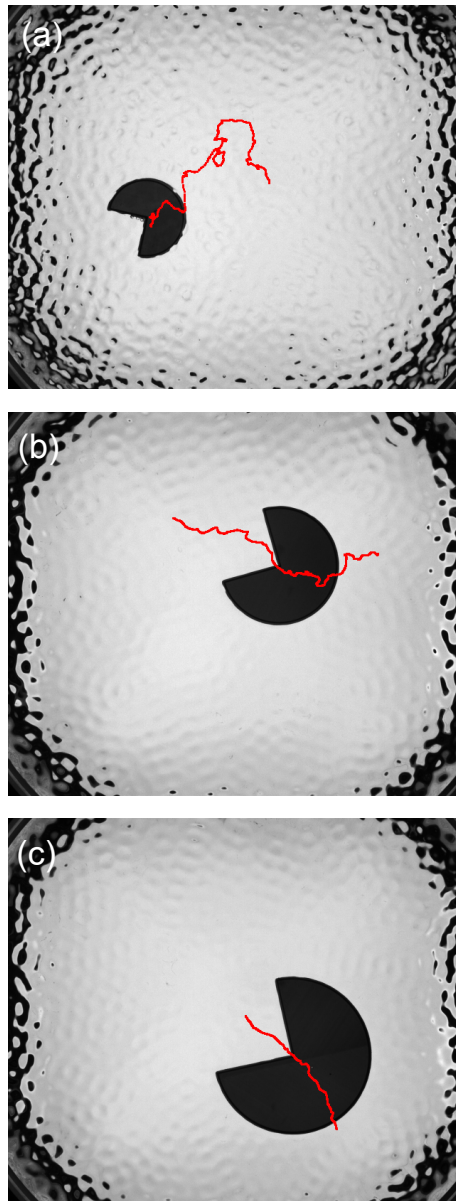
Figure 4.5: Trajectories of pacman-shaped particles in a turbulent flow forced at 60 Hz, L_f = 4.4 mm (a) r_s= 20 mm, r_s/L_f = 4.54; (b) r_s = 30 mm, r_s/L_f = 6.81; (c) r_s = 40 mm, r_s/L_f = 9.09. Turbulent flows parameters: L_f = 4.4 mm forced at f = 60Hz.

The results above indicate a link between the size of the particle (r_s) and the forcing scale of the flow (L_f). These two parameters provide the ability to control the dynamics of a pacman-shaped particle in 2D turbulence. A change of the particle size (r_s) with respect to the flow scale (L_f) substantially alters the translational behaviours of the pacman-shaped particle. To better understand and quantify this effect, we next introduce the size ratio parameter, which is defined as the ratio of the size of the particle to the forcing scale of the flow, i.e. r_s/L_f.

In our experiments, we cover the range of size ratios r_s/L_f from 0.3 to 10. The translational motion of the pacman-shaped particles of large size ratios are mostly dominated by directional propulsion. The data shown in 4.5 (c) corresponds to a size ratio $r_s/L_f = 9.09$, which exhibits a directional motion. Although the particles are impacted by the turbulent component, no erratic motions are observed. On the other hand, the pacman-shaped particles with small size ratios behave like an isotropic circular disc. For example, in Figure 4.4 (d), where $r_s/L_f = 2.5$, the trajectory of the pacman-shaped particle is random, and the motion is mostly governed by the turbulent component of the turbulent flows.

By altering the size ratio r_s/L_f, we can control the trajectories of the pacman-shaped particles in turbulent flows. With this in mind, we study the impact of r_s/L_f on the statistical characteristics of these trajectories, such as the mean-squared displacement (MSD, $\langle r^2 \rangle$) and the auto-correlation function (ACF, $\rho(t)$). Comparisons of the MSDs and ACFs for two pacman-shaped particles, with $r_s/L_f = 2.5$ and 6.6, are shown in Figure 4.6 (a) and (b), respectively. For pacman-shaped particles with small size ratios, both ballistic and diffusive regimes can be seen in the MSDs. The Lagrangian velocity ACFs ($\rho(t)$) of small size ratio particles are identical to those of the circular discs, as shown in Figure 4.3 (b). The corresponding trajectories are random and erratic. However, for the pacman-shaped particles with large size ratios, the MSDs only show a superdiffusive regime, where $\langle \Delta r^2 \rangle \sim t^2$. The Lagrangian velocity ACFs ($\rho(t)$) are affected by both the turbulent and propulsive components. The trajectories of the corresponding pacman-shaped particles are almost straight.
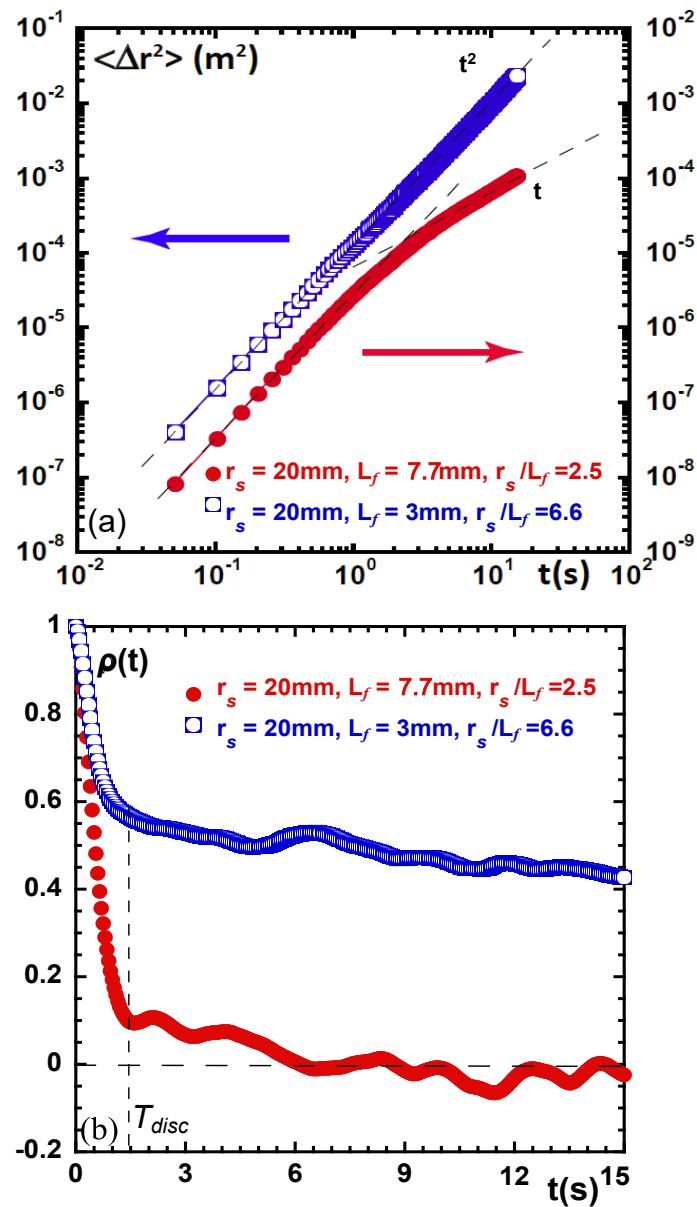
Figure 4.6: (a) Mean-squared displacements (MSDs) and (b) Lagrangian velocity auto-correlation functions (ACFs) of pacman-shaped particles with size ratios of $r_s/L_f =$ 2.5 and 6.6.

We show that the size ratio (r_s/L_f) of the pacman-shaped particle is the key parameter determining the translational dynamics of the particle. Its dispersion can be changed from a directional motion to a random walk by changing the size ratio.

4.3 Rotational motion of pacman-shaped particles

In this section, we investigate the rotational dynamics of the pacman-shaped particles in detail. These dynamics can be characterised by two orientations, specifically the orientation of the particle θ_p and the direction of the moving velocity θ_v. The associated unit vectors are referred to as $\mathbf{n_p}$ and $\mathbf{n_v}$.

The mean-squared angular displacement (MSAD, $\langle \Delta\theta^2 \rangle$) is calculated based on the orientation of the particle θ_p. Figure 4.7 presents the results for pacman-shaped particles with r_s/L_f = 3.33, 6.81 and 9.09. All of the MSADs present a transition from a ballistic regime at short time-scale ($\langle \Delta\theta^2 \rangle \sim t^2$) to a diffusive regime at long time-scale ($\langle \Delta\theta^2 \rangle \sim t$). This transition indicates that the particle's rotation is initially unidirectional and then undergoes random fluctuations. The rotational diffusion coefficient D_θ can be calculated as $D_\theta = \langle \Delta\theta^2 \rangle / 2t$. Under the action of turbulence, the pacman-shaped particles undergo random rotational motion at long time-scale.
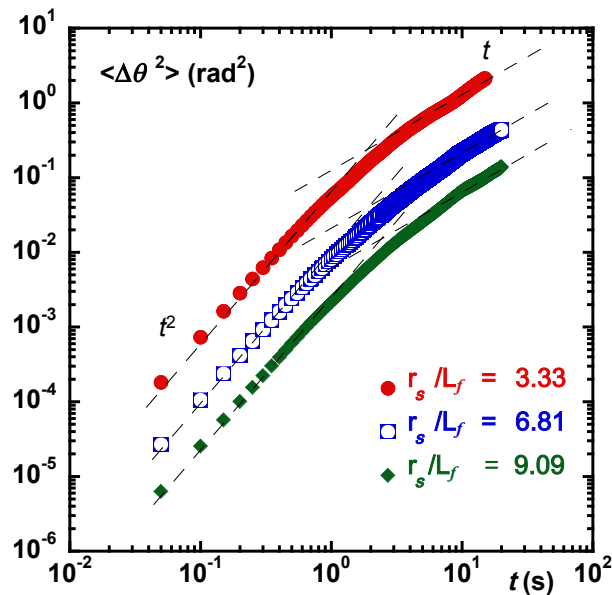
Figure 4.7: Mean-squared angular displacement (MSAD) $\langle \Delta\theta^2 \rangle(t)$ for r_s/L_f = 3.33, 6.81 and 9.09. The dashed lines indicate fittings for ballistic regime ($\sim t^2$) and diffusive regime ($\sim t$).

There are two rotational characteristic times that govern the rotational dynamics

of pacman-shaped particles. The first one is T_ω, which is defined as the integral of the auto-correlation function of angular velocity ($\rho(\omega)$), where $\rho(\omega) = \langle \boldsymbol{\omega}(t_0 + \Delta t)\boldsymbol{\omega}(t_0)\rangle$. T_ω characterises the memory effect of the particle's rotation based on its angular velocity. T_ω can also be estimated from the time scale of the transition from ballistic to diffusive regime in the MSADs. The second rotational characteristic time (T_θ) is based on the auto-correlation function of the orientational unit vector of the pacman-shaped particle ($\rho(n_p)$), where $\rho(n_p) = \langle \mathbf{n_p}(t_0 + \Delta t)\mathbf{n_p}(t_0)\rangle$. T_θ represents the time scale for which the particle travels along one direction. When the trajectory of the particle is straight, the value of T_θ is high. However, due to the jiggling motion of the particle under the effect of turbulent flow, the angular velocity fluctuates, which leads to a low value of T_ω.

In these experiments, T_θ is a better characteristic time that covers both the rotational dynamics of the particle and the time scale that the particle spends on directed translational motion. Figure 4.8(a) presents the results of $\rho(n_p)$ for particles with different size ratios. T_θ can be estimated by exponential fittings to RACFs as $\rho(n_p) = e^{(-\Delta t/T_\theta)}$. This shows that T_θ is strongly dependent on the ratio r_s/L_f. The relation between T_θ and r_s/L_f is shown in Figure 4.8(b) with an exponential function of $T_\theta \approx e^{\,\epsilon\, r_s/L_f}$. Among all experiments, the range of T_θ covers almost two orders of magnitude. Moreover, the exponential rate of growth ϵ is around 0.5, which points to L_f as the characteristic length scale governs the rotational dynamics of particles.

A schematic to illustrate how the translational and rotational diffusivity control the dynamics of a pacman-shaped particle in 2D turbulence is shown in Figure 4.9. In this scenario, the particle's initial translational dynamics is governed by the passive directional propulsion. When time $t < T_\theta$, the particle travels along the direction of the initial orientation $\mathbf{n_p(t_0)}$ while experiencing small erratic agitations due to the rotational dynamics. With the increase in time, the semi-balanced state breaks up because of the competition between the translational and rotational dynamics, leading to the angular differences between $\mathbf{n_v}$ and $\mathbf{n_p}$. Eventually, when $t > T_\theta$, the particle's orientation are steered away from its initial orientation due to the randomisation of
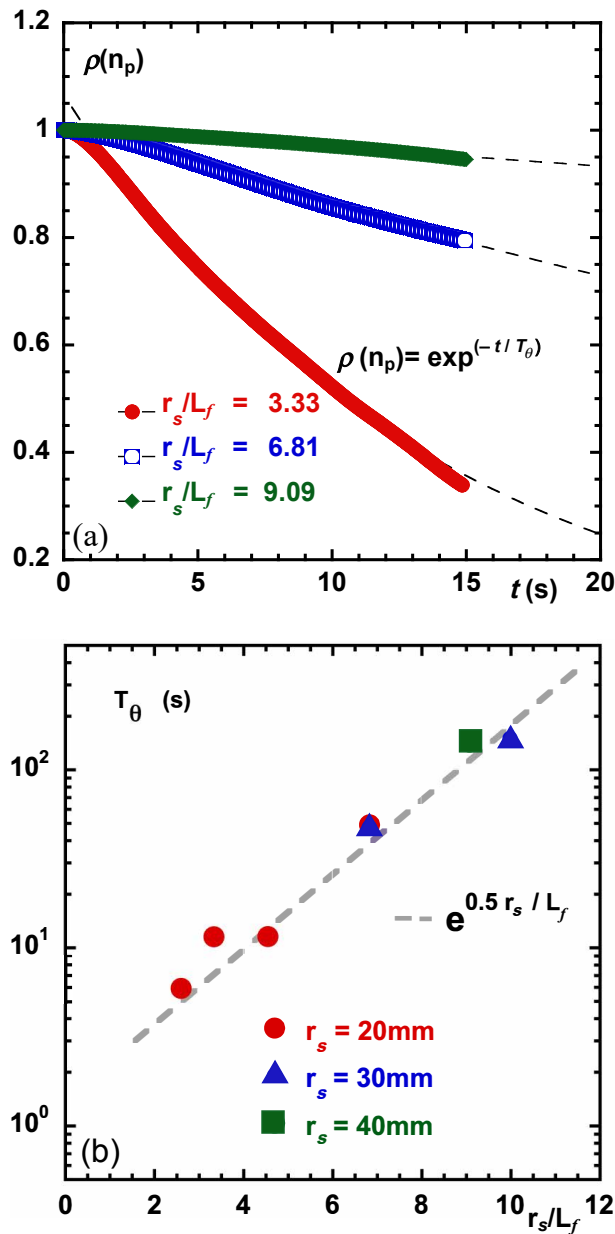
Figure 4.8: (a) Rotational auto-correlation function of the orientational vector $\mathbf{n_p}$ of pacman-shaped particles for the size ratios r_s/L_f = 3.33, 6.81 and 9.09. The dashed lines show the exponential fitting of $\rho(n_p) = e^{(-\Delta t/T_\theta)}$; (b) Rotational characteristic time T_θ with respect to the size ratio r_s/L_f. T_θ characterises the randomisation of the particle's orientation. All experimental data can be fitted by $T_\theta \sim (e^{0.5\,r_s/L_f})$, as indicated by the dashed line.

the rotation. This picture demonstrates the importance of the coupling between translational and rotational motion.
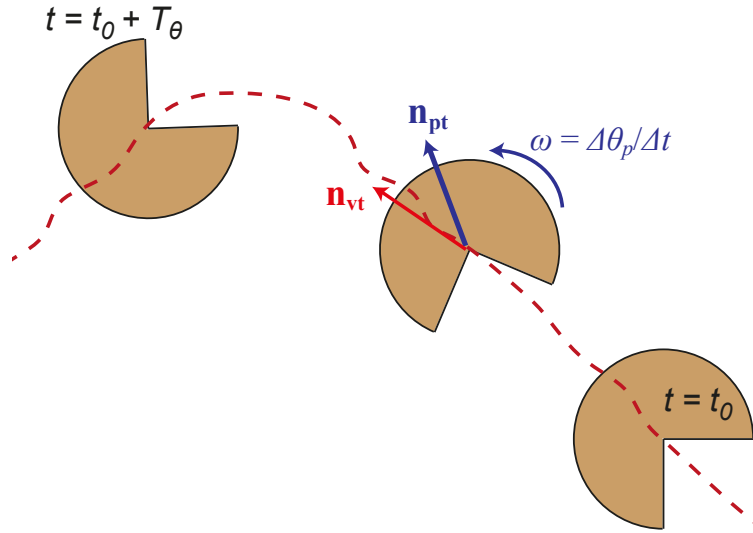
Figure 4.9: The motion of the pacman-shaped particles in 2D turbulence under the impact of translational and rotational dynamics. For the angular coordinate system of a pacman-shaped particle ($\mathbf{n_p}$, $\mathbf{n_v}$): $\mathbf{n_p}$ characterises the particle's orientation, while $\mathbf{n_v}$ characterises the direction of the particle's velocity.

4.4 Coupling between translational and rotational motion

The motion of the pacman-shaped particle is governed by both the translational and rotational motion. In this section, we investigate the coupling between the translation and rotation.

The correlation between the particle's orientation θ_p and the direction of its velocity θ_v is considered. The angle difference between the two directions is referred to as the angle of attack (AOA), which is defined as $\Delta\theta_{pv} = (\theta_p - \theta_v)$, where $\Delta\theta_{pv} \in [-180°, 180°]$. AOA = 0° indicates that the particle's direction of motion is along its orientation, while AOA = 90° means that the particle moves in a direction perpendicular to its orientation (transversely).

Along the trajectories of the pacman-shaped particle, AOA is a random variable with a clear bias due to the anisotropic shape of the particle. This statistical bias can be clearly seen in the probability density function (PDF), as shown in Figure 4.10,

which peaks at AOA = 0°. This bias grows stronger as r_s/L_f becomes larger. All of these results indicate an increased likelihood of alignment between θ_v and θ_p, which leads to directed locomotion. In contrast, the PDF of a circular disc is flat for the entire range, illustrating the absence of correlations between the velocity vector direction and an arbitrary direction marked on the disc.
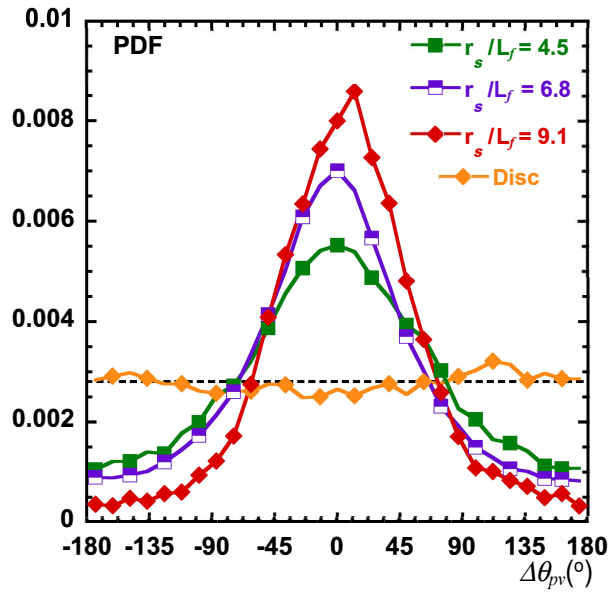
Figure 4.10: Probability density function (PDF) of the angle of attack $\Delta\theta_{pv} = \theta_p - \theta_v$ for a circular disc and pacman-shaped particles with various size ratios r_s/L_f.

With reference to the shape of the PDF, we defined three domains based on the absolute value of AOA and labelled them as $\Delta 1$, $\Delta 2$ and $\Delta 3$, respectively. $\Delta 1$ corresponds to the directional propulsive domain (positively correlated) for which $|\Delta\theta_{pv}| \in [0°, 45°]$; $\Delta 2$ is the random domain (uncorrelated) for which $|\Delta\theta_{pv}| \in [45°, 135°]$; finally $\Delta 3$ is the friction domain (negatively correlated) for which $|\Delta\theta_{pv}| \in [135°, 180°]$. With a fixed particle orientation θ_p, the range of the location for θ_v with respect to each domain is indicated by the shaded areas in Figure 4.11.

The magnitude of the particle velocity modulus $|V_p|$ is found to be dependent on the absolute value of the AOA, $|\Delta\theta_{pv}|$. This effect is studied by computing the average velocity of pacman-shaped particles or circular discs over each angular domain $V_{pi} = |\langle V_p \rangle_{\Delta i}|$, where i is the domain number $i = 1, 2$ and 3. This is referred to
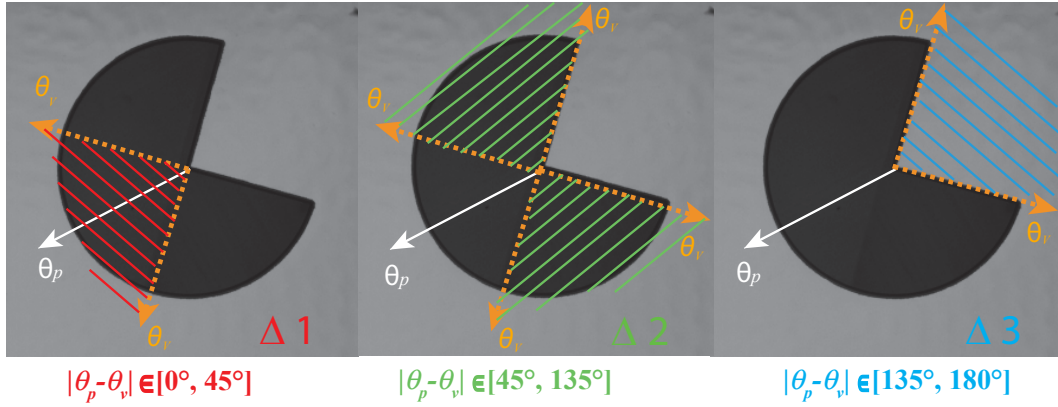
Figure 4.11: Schematics of three domains Δi, i = 1, 2, 3. The directional propulsive domain (positively correlated) is denoted as $\Delta 1$, for which $|\Delta\theta_{pv}| \in [0, +45°]$; the random domain (uncorrelated) is denoted as $\Delta 2$, for which $|\Delta\theta_{pv}| \in [45°, 135°]$; finally the friction domain (negatively correlated) is denoted as $\Delta 3$, for which $|\Delta\theta_{pv}| \in [135°, 180°]$.

as conditional average velocity. Figure 4.12 illustrates the conditional average velocity as a function of the specific domain Δi. For the case of a circular disc, the conditional averaging of the disc speed shows no dependence on the angular domain. For the pacman-shaped particles, V_{pi} is normalised by the average velocity of a circular disc $\langle V_{disc}\rangle$. As the size ratio increases, V_{pi} becomes incrementally larger than $\langle V_{disc}\rangle$. We further note that V_{p1} is persistently larger than V_{p2} and V_{p3}, which means that the pacman-shaped particles have higher translational velocities when they are in the propulsive domain ($\Delta 1$). The above results further confirm that the emergence of the directional motion is related to the size ratio r_s/L_f.

Figure 4.13 (a) shows the r.m.s velocity of the pacman-shaped particle $\langle V_p^2\rangle$ with respect to the size ratio. It is found that $\langle V_p^2\rangle$ is a function that decreases with the increase of r_s/L_f. $\langle V_p^2\rangle$ for a large pacman-shaped particle (r_s/L_f = 10) is almost two orders of magnitude smaller than that of a small pacman-shaped particle (r_s/L_f < 1).

The kinetic energy is calculated as $E_s = M_s \langle V_p^2\rangle$, where M_s is the mass of the particle. Since our particles are passive and the turbulent flow is the only source of power, the kinetic energy of the particle can also be considered as the energy extracted from the chaotic motion of fluid flows. Figure 4.13 (b) reveals that there is no dependence
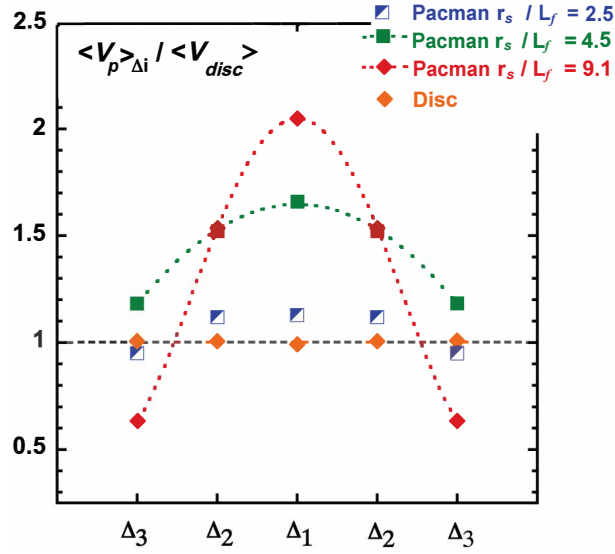
Figure 4.12: Normalised conditional average velocity $V_{pi}/|\langle V_{disc}\rangle|$ as a function of the domain Δi, where V_{pi} is the pacman-shaped particle's velocity modulus conditionally averaged over an angular domain Δi, i =1, 2, 3. $\langle V_{disc}\rangle$ is the averaged velocity modulus of a circular disc with the same size, r = r_s.

of the energy E_s on the size ratio r_s/L_f. It turns out that pacman-shaped particles with $r_s/L_f > 1$ extract the same amount of energy from the turbulent flow. Combined with the data shown in Figure 4.10 and Figure 4.12, we conclude that the main ingredient for the passive propulsion acting on the particle is characterised by the partition of the kinetic energy E_s between the different velocity components V_{pi}.

4.5 Passive propulsion generated by fluid-particle interaction

To gain further insights into the particle's directional propulsion, we defined the effective propulsive velocity as $V_{eff} = p_1 V_{p1} - p_3 V_{p3}$ and the turbulent velocity $V_{turb} = p_2 V_{p2}$, where p_i indicates the probabilities of $|\Delta\theta_{pv}| \in \Delta_i$, i =1, 2, 3. This allows us to compute a propulsion parameter β, defined as:

$$\beta = V_{eff}/V_{turb}, \tag{4.3}$$
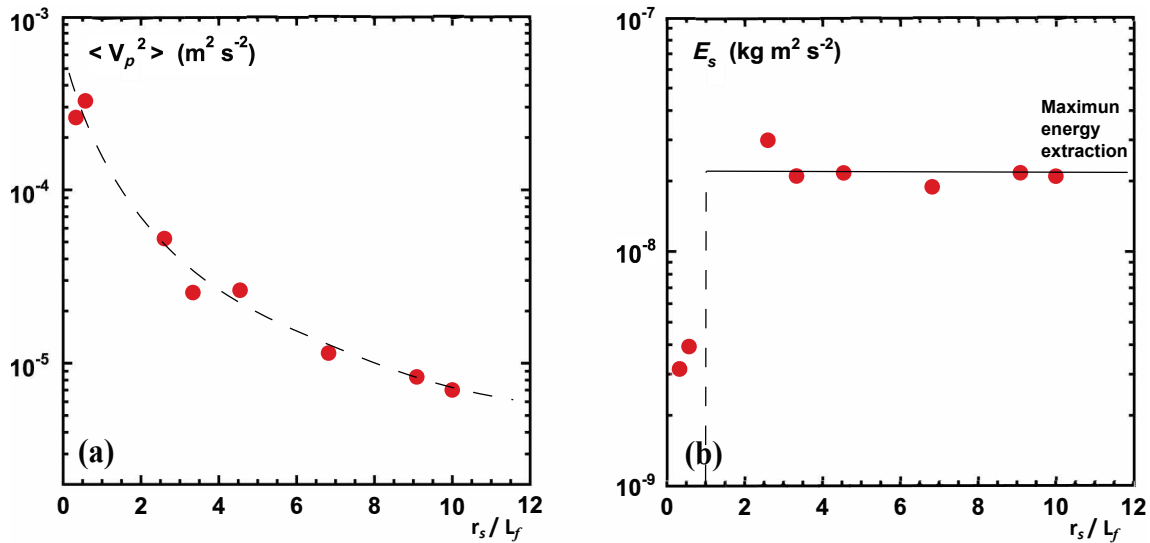
Figure 4.13: (a) r.m.s velocity of pacman-shaped particles $\langle V_p^2 \rangle$ as a function of the size ratio r_s/L_f. (b) Kinetic energy E_s with respect to the size ratio r_s/L_f, where $E_s = M_s \langle V_p^2 \rangle$. Experimental parameter: flow energy $\langle u \rangle = 2.3 \times 10^{-2}$ ms^{-1}, L_f = 3mm to 7.7mm.

The findings reveal β characterises the partition of energy between the effective propulsive (positively and negatively correlated) and random (uncorrelated) components of the pacman-shaped particle's velocity.

A high value of β means that a higher fraction of the kinetic energy contained in the particle (E_s) will be transferred to fuel the directed propulsive motion. This leads to increased efficiency in terms of energy conversion. The dependence of β for pacman-shaped particles and circular discs on the size ratio r_s/L_f is illustrated in Figure 4.14. A circular disc that diffuses randomly in turbulence shows no bias on V_{p2}, V_{p2} and V_{p3}, since there is no propulsion acting on it. As a result, β is close to 0 regardless of the size. For the case of the pacman-shaped particle, no propulsion can be found when the size ratio $r_s/L_f < 1$. Thus, these small particles will behave similarly to the random walk of circular discs. With the increase of the size ratio, $1 < r_s/L_f < 6$, the propulsive parameter (β) increases linearly over the range and reaches about 1.5 at the highest size ratio. When $r_s/L_f > 6$, β saturates at a level, where the effective propulsive velocity (V_{eff}) is 1.5 times higher than the typical velocity component associated with the turbulent agitations in this regime (V_{turb}). The plateau in

β suggests that the size of this protected fluid domain that produces the propulsion cannot exceed 6 L_f.

The main ingredient for the saturation of turbulence-driven propulsion is the confinement (either global or partial) of 2D turbulence. In this experiment, there is a fluid domain in which the river bundles are both protected from the external turbulent fluctuations and guided by the two-sided boundary wall in the vicinity of the particle's cut-out corner (see Figure 4.15). The presence of solid boundaries combined with the existence of underlying coherent structures in the flow might operate in a similar way to the formation of spectral condensation in 2D turbulence. This spectral condensation is one of the most important features of 2D turbulence. It was observed experimentally that the inverse cascade of 2D turbulence transfers energy up to scales in a square boundary box whose size is close to 10 L_f and leads to a single large-scale vortex [121, 35]. This is due to the reason that the protection of the coherent bundles from the turbulent fluctuations will result in an increased correlation length. Once the correlation length is larger than the size of the boundary box, a condensate may form. Compared to the spectral condensation in 2D turbulence, the experiment of particles in the propulsive regime is in an open system (only 2 walls are presented to protect the fluid domain). The correlation time of the fluid bundle with pacman-shaped particle might be different from that of spectral condensation, and other instabilities might develop to shortening the correlation time. This might be the reason behind the difference in the characteristic size ratio in these two cases: 6 L_f of the propulsive mechanism to 10 L_f of the spectral condensation.

As described in previous research [36], the mechanism of propulsion by a Z-shaped rotor is related to the coupling of river-like coherent structures in the wave-driven turbulent flows that interacts with the solid boundary of the object. With such fluid-structure interactions, a rotor has been engineered to rectify turbulent fluctuations in a chaotic environment to fuel its unidirectional rotation. It is of interests to investigate how the underlying fluid flow interacts with the pacman-shaped particles to generate passive propulsion.
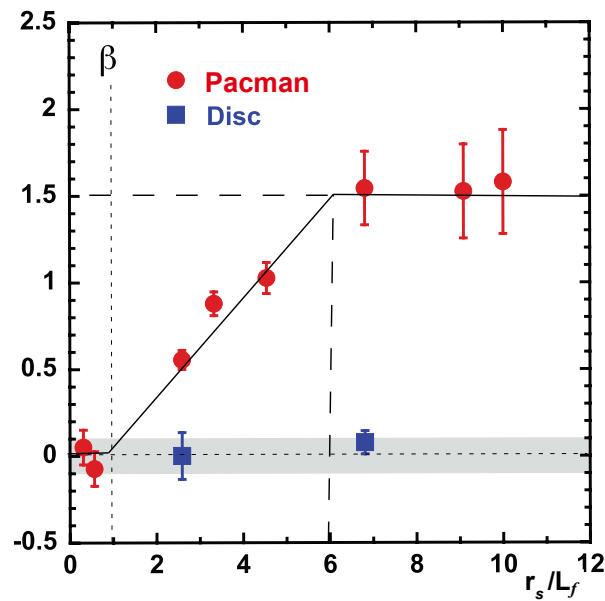
Figure 4.14: Propulsion parameter β versus the scale ratio r_s/L_f. The measured value of β for a circular disc, which should theoretically be zero, is also shown to indicate the noise level (grey area).

In order to visualise this interaction, 50 μm tracer particles are seeded in the turbulent flow in the vicinity of a pacman-shaped particle. The time-averaged image of the fluid motion with the presence of the pacman-shaped particle is shown in Figure 4.15. A coherent Lagrangian bundle structure away from the particle is observed, where the fluid particles in this bundle exhibit non-diverging behaviour for a sufficiently long period of time. This time period is significantly longer than the characteristic time of the flow (T_L). The width of this bundle structure is related to the forcing scale of the flow (L_f). At the pacman's cut-out corner, a fluid bundle interacts with the solid boundary (two-sided wall) such that the momentum of the fluid particles will be rectified and transferred to the pacman-shaped particle. This guiding effect produces a reaction force (propulsion force) that results in the particle's directional locomotion. Our experiments show how such coherent flow structures are both protected from and guided by the external turbulent fluctuations. The propulsive force F_{prop} generated by the fluid-particle interaction is also measure using an optical fibre cantilever. The details of the setup and measurement techniques are shown in Appendix B.
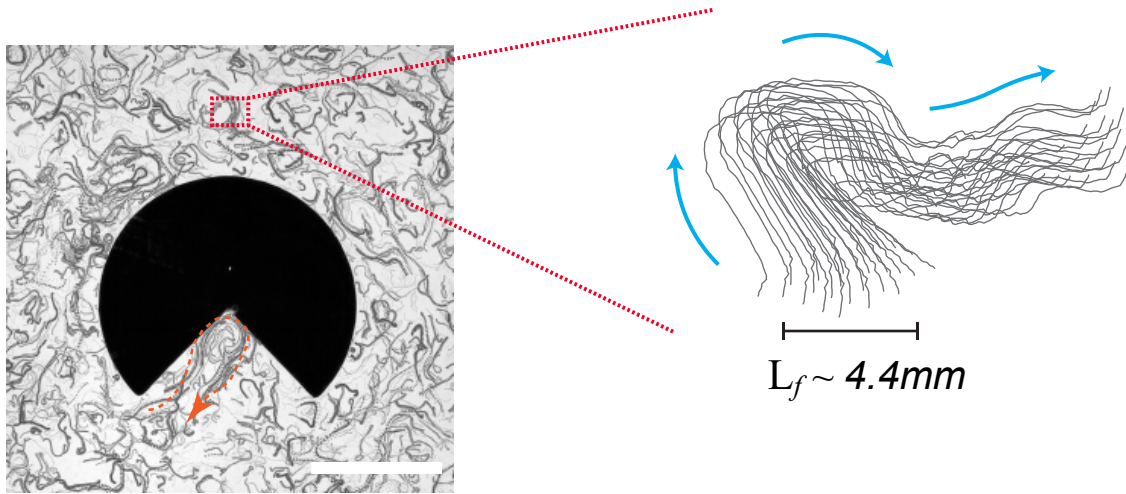
Figure 4.15: The interaction between the underlying coherent structure in 2D turbulence and the cut-out boundary of the pacman-shaped particle that fuels its directed motion. Experimental parameters: r_s = 40 mm, L_f = 4.4 mm. The sizes of tracer particles are 50 μm. Red square area: the schematic of a Lagrangian coherent bundle structure in two-dimensional turbulence away from the pacman-shaped particle. The width of the bundle is close to the forcing scale of the flow, $\sim L_f$ [116]

4.6   Shape optimisation for energy extraction and passive propulsion

The previous results on the propulsion of the pacman-shaped particle were obtained with a cut-out sector $\alpha = 90°$. In terms of passive motion of particles in a fluid environment, it is also important to reduce the friction (drag) and maximise the momentum transfer from the flow to the particle. It is interesting to ask whether an optimal shape for the pacman-shaped particle exists for which both the extracted energy E_s and the propulsion parameter β can be maximised? To address this question, we conducted experiments with pacman-shaped particles by varying the angle of the cut-out sector (α) from 0° (circular disc) to 270° (a quarter of a circular disc). In the experiments, we focus on a sample case of a particle with radius r_s of 40mm, at a fixed turbulent flow energy and forcing scale f = 60 Hz, where L_f = 4.4 mm. The r.m.s velocity of the flow $\langle u \rangle = 2.3 \times 10^{-2}$ ms^{-1}. The corresponding size ratio r_s/L_f of these particles in turbulence equals to 9.09.

The evolution of the particle's kinetic energy E_s over a broad range of angles α is presented in Figure 4.16, where $E_s = M_s \langle V_p^2 \rangle$. The figure reveals the existence of a maximum in the kinetic energy of particles for $\alpha = 90°$. The kinetic energy extracted from turbulence by a pacman-shaped particle with a 90° cut-out sector is two times larger than that extracted by a disc or a wedge ($\alpha = 270$ °) with the same radius. More-over, although the mass of the pacman-shaped particles with $\alpha = 0°$ and $\alpha = 270°$ are completely different, the kinetic energies for both of them are almost equivalent.
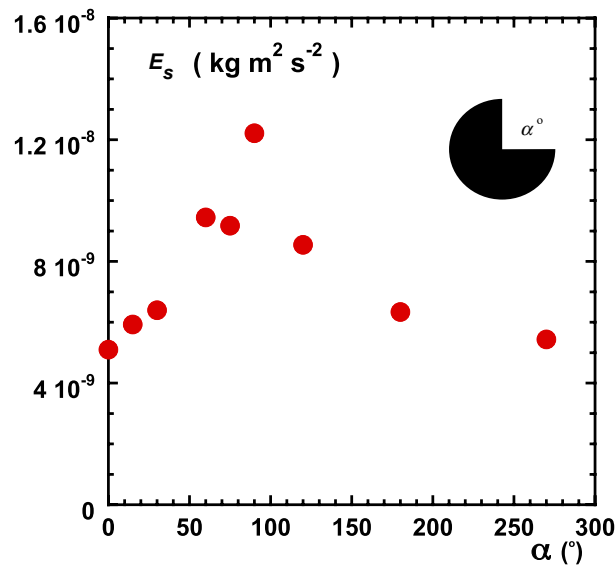
Figure 4.16: Kinetic energy E_s as a function of the cut-out sector α. Experimental parameters: $r_s = 40$ mm, $\langle u \rangle = 2.3 \times 10^{-2}$ms^{-1}, $L_f = 4.4$ mm.

The evolution of the propulsion parameter β as impacted by the shape of the pacman-shaped particle is shown in Figure 4.17. Starting with $\beta = 0$, which indicates no propulsion of a circular disc, β is a non-monotonic function of α. The maximum of β (≈ 1.5) is found for $\alpha = 90°$. When $\alpha > 90$ °, β decreases gradually as the size ratio continues to increase. A pacman-shaped particle with $\alpha = 270°$ shows almost no propulsion ($\beta \approx 0$), similar to a circular disc ($\alpha = 0°$).

These results demonstrate that the geometry of a pacman-shaped particle plays an important role in enhancing the propulsive force and extracting the kinetic energy from the turbulent flow. With the optimal design of $\alpha = 90°$, we are able to both
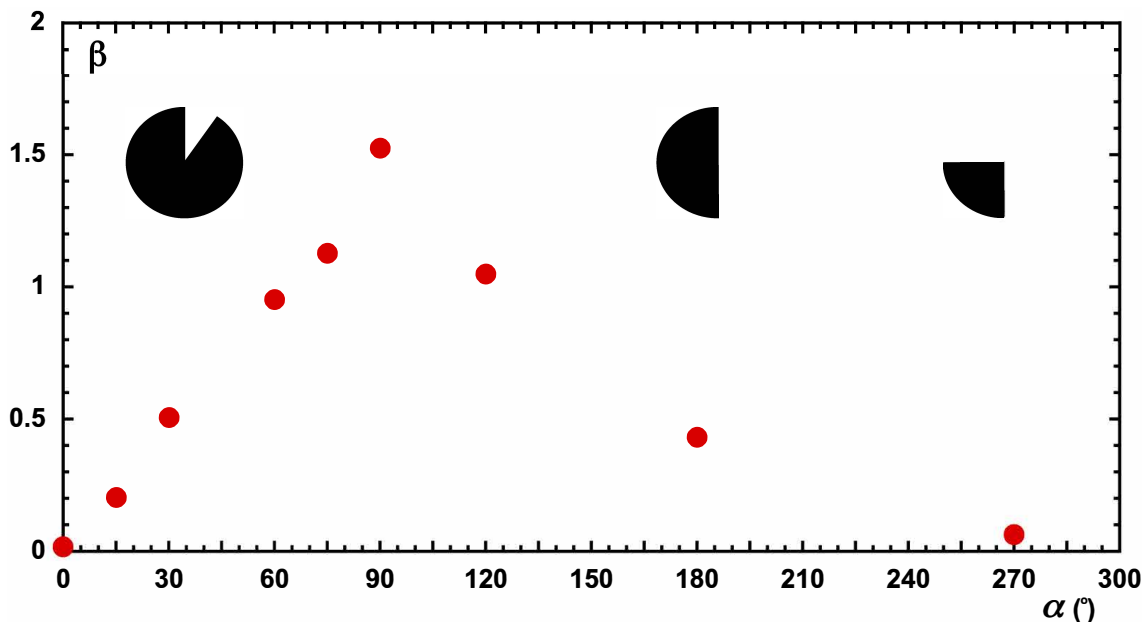
Figure 4.17: Propulsion parameter β as a function of the cut-out sector α. Experimental parameters: $r_s = 40$ mm, $\langle u \rangle = 2.3 \times 10^{-2}$ ms^{-1}, $L_f = 4.4$ mm.

extract the maximum amount of energy (E_s) from the turbulent flow and, at the same time, produce the largest passive propulsion parameter (β).

With reference to the above sections about passive propulsion and shape optimisation, we emphasise that the propulsive parameter β ($\beta = V_{eff}/V_{turb}$) encapsulates two features of the motion of the pacman-shaped particles. The first is the enhanced angular alignment between the particle's velocity direction θ_v and its orientation θ_p; while the second is the characterisation of the particle's ability to tap energy from the turbulent flow.

4.7 Comparison between propulsive and diffusive length scales

A pacman-shaped particle is able to propel itself with an effective propulsive velocity V_{eff} along a direction prescribed by its geometry. It has been shown that this directional motion is subject to turbulent rotational motion, which leads to a coupling

between translation and rotation. In this section, we use a simple minimal model to describe the influence of this coupling on the MSD of a pacman-shaped particle with a 90° cut-out sector.

A key parameter in modelling the behaviour of the pacman-shaped particle is the propulsion length scale $L_\beta = V_{eff}T_\theta$, where V_{eff} is the effective propulsion velocity and T_θ is the characteristic time scale of turbulent rotational diffusion. This represents the average distance travelled by a particle before its orientation is randomly changed. This length scale characterises the coupling between propulsion and rotation. Based on this observation, we propose to model the MSD $\langle \Delta r^2(t) \rangle$ of a pacman-shaped particle as follows:

$$\langle \Delta r^2(t) \rangle = 2D_t \Delta t + \frac{V_{eff}^2 T_\theta^2}{2} \big[\frac{2\Delta t}{T_\theta} + e^{-2\Delta t/T_\theta} - 1 \big] \tag{4.4}$$

where D_t is the translational diffusion coefficient that characterises the turbulent transport, while $\langle \rangle$ denotes statistical averaging.

We note that equation (4.4) is generally found in the modelling of a particle endowed with a directed propulsive mechanism (propulsive component) and subject to a rotational process that randomises the direction of its motion (in our case, the turbulent component). A similar model has been used to characterise the behaviour of self-propelled colloidal particles whose propulsion mechanism relies on asymmetric chemical properties [45]. Equation (4.4) allows us to describe our experimental observation of the transition from turbulent to directed motion, such as the MSDs shown in Figure 4.6 (a).

An interesting aspect of the right-hand side of the equation is that it predicts a transition in the dynamics related to the characteristic time scale T_θ. More precisely (if turbulent diffusion D_t is neglected for simplicity), two regimes can be described:

(i) When $\Delta t < T_\theta$, the dynamics is dominated by $\langle \Delta r^2(t) \rangle \approx L_\beta^2 \Delta t^2 / T_\theta^2 \approx V_{eff}^2 \Delta t^2$; this corresponds to the ballistic propulsive regime.

(ii) At the opposite limit, when $\Delta t > T_\theta$, we have $\langle \Delta r^2(t) \rangle \approx L_\beta^2 \Delta t / T_\theta \approx V_{eff}^2 T_\theta \Delta T$, which corresponds to the enhanced diffusion regime due to the coupling of rotational diffusion and propulsion.

In our experiments, equation (4.4) offers a basis for studying the interplay between three mechanisms: turbulent transport, directed propulsion, and rotational diffusion. The competition between these effects can be studied by comparing two characteristic length scales, namely L_β and a length scale associated with the turbulent transport L_t. The latter one can be associated with the case of a circular disc in a turbulent flow, where no propulsion can be found ($V_{eff} = 0$). The dynamics of a circular disc is only governed by the turbulent transport, such that L_t can be directly determined as $L_t = L_{disc} = 2D_{disc} / V_{disc}$, where V_{disc} is the r.m.s velocity of the circular disc.

The propulsion length scale L_β for the case of the pacman-shaped particles can be estimated using the measurements of the rotational characteristic time scale T_θ and of the effective propulsion velocity V_{eff}, as shown above. The length scale L_β represents the transition from the propulsion-dominated regime to the enhanced diffusion regime. Indeed, for $\Delta t = T_\theta$, the MSD is equal to $\langle \Delta r^2(T_\theta) \rangle = L_\beta^2$. With this in mind, the comparison between L_t and L_β allows us to describe most of our previous observations. In particular, we can now quantitatively discuss the influence of the finite container size on our results.

The evolution of the characteristic length scales L_β and L_t versus the size ratio r_s / L_f is shown in Figure 4.18. For the case of a circular disc, the distance travelled before its motion becomes diffusive (L_t) exhibits a decreasing trend as the size ratio increases. It is also worth noting that L_t is always much smaller than the radius of the container R_c. Therefore, it is possible to observe the transition from the ballistic regime at short time-scale ($\langle \Delta r^2(t) \rangle \sim t^2$, $t < T_{disc}$) to the turbulent diffusive regime
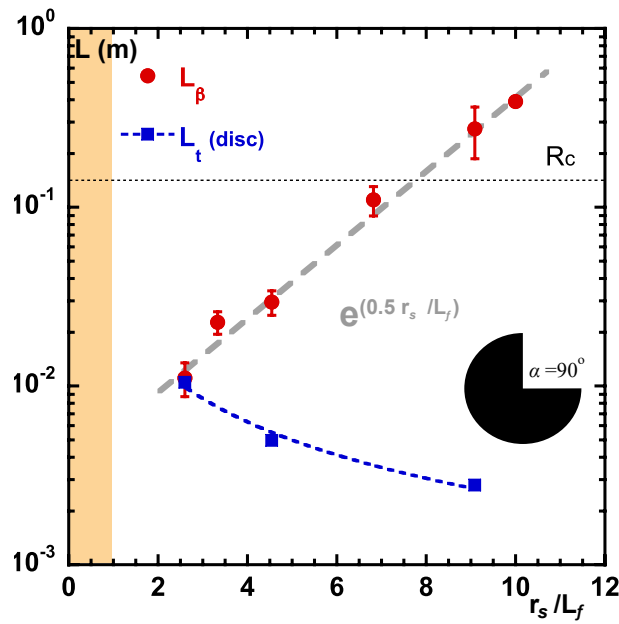
Figure 4.18: Length scales L_β and L_t versus the scale ratio r_s/L_f for a pacman-shaped particle with $90°$ cut-out sectors. The light grey dashed line indicates the exponential growth of L_β versus r_s/L_f. The horizontal dashed line indicates the container radius R_c. Experimental parameters: r_s is in a range of 20 mm to 40 mm. The forcing scale of the flows, L_f, varies from 3 mm to 9 mm.

at long time-scale ($\langle \Delta r^2(t) \rangle \sim t, t > T_{disc}$), regardless of the size of the circular discs.

For the case of the pacman-shaped particle, L_β shows exponential dependence on r_s/L_f, which is inherited from the behaviour of T_θ (as shown in Figure 4.8 (b)). The dynamics can be classified into two groups. (1) When the size ratio $r_s/L_f < 4$, the dynamics of these particles at long time-scale are diffusive. This is because L_β has a comparable magnitude as L_t and both of them are smaller than the radius of the container R_c. As such, it is possible to observe the random motion of the pacman-shaped particle in turbulent flows after a finite time T_θ. In the diffusive regime, the effective diffusion coefficient of the particle is actually composed of two terms, where $D_{eff} = D_t + V_{eff}^2 T_\theta$. (2) When the size ratio is large, $r_s/L_f > 6$, L_β becomes comparable to or larger than R_c and much larger than L_t. It implies that propulsion effects become dominant over the turbulent transport and that only the propulsive ballistic regime $\langle \Delta r^2(t) \rangle \approx L_\beta^2 \Delta t^2 / T_\theta^2$ can be observed due to the finite size of the container. For instance, L_β is 100 times larger than L_t and two times larger than R_c for $r_s/L_f = 9.09$.

An important insight provided by this model is the realisation that even for the pacman-shaped particle with a large size ratio ($r_s/L_f > 6$), the propulsion mechanism will eventually revert to a random walk for times longer than T_θ in an unbounded environment. In this final regime, the effective diffusion coefficient $D_{eff} = V_{eff}^2 T_\theta$ is a strong function of the size ratio r_s/L_f and it can be much higher than the turbulent diffusion coefficient D_t. For example, we find that $D_{eff} = V_{eff}^2 T_\theta \approx 500 D_t$ at $r_s/L_f = 9.09$. The physical mechanisms of the particle's motion with large size ratio can be explained by the interactions between the particle with the fluid bundles. As described previously, the river bundles are both protected from the external turbulent fluctuations and guided by the two-sided boundary wall in the vicinity of the particle's cut-out corner, which affects the correlation time of the fluid bundle significantly. In this state, the particle moves directionally and stays in the "propulsive" regime. Once the correlation time of the fluid bundle is reached, the large size ratio particle will turn into a random walk (diffusive regime) and wait for the interaction with another fluid bundle.

4.8 Discussion

It has been recently reported that a chiral rotor was able to efficiently extract kinetic energy, accumulated in the inertial range of 2D turbulent flow, to fuel its unidirectional rotation [36]. The Lagrangian nature of the physical mechanism of energy conversion has been discussed in detail. In this experiment, we study a different aspect of such locomotion, which is related to the broader topic of passive propulsion generation in a chaotic flow. We demonstrate that anisotropic finite-size particles, referred to as pacman-shaped particles, can efficiently extract energy from turbulent flows to fuel directed locomotion. The results show that the ratio of the particle size to the flow forcing scale r_s/L_f is a key parameter that controls the existence of this type of locomotion. The role played by the forcing scale L_f in the propulsion mechanism is related to the coupling of the anisotropic particle to the underlying river-like structure

of the turbulent flow. This coupling, which has been described in prior research [36], is the fuel of the passive propulsion force F_{prop} acting on the particle. The mechanism relies on momentum transfer from bundles of fluid trajectories with characteristic width L_f to the pacman-shaped particle. The importance of this Lagrangian flow structure is reflected in the dependence of V_{eff} and T_θ on the size ratio r_s/L_f. One of the additional findings is that there is almost no passive propulsion generated ($\beta \approx 0$) when $r_s/L_f < 1$, as shown in Figure 4.14. This might be because the size of the cut-out sector is too small to rectify the motion of the underlying river-like structures. In this situation, these small pacman-shaped particles behave similar to circular discs and undergo a random walk.

This study reveals two key features of passive propulsion in wave-driven turbulence:

(i) The coupling between the translation and rotation of the pacman-shaped particle is a natural consequence of a directed propulsion mechanism prescribed by the particle's anisotropic shape. The characteristic time scale of the propulsion is related to the rotational dynamics T_θ. The motion of the pacman-shaped particle will ultimately revert to a random walk under the action of the turbulent rotational motion in an unbounded fluid domain. In our experiments, T_θ is an exponential function of the size ratio r_s/L_f. This feature gives us the ability to tune the magnitude of the effective diffusion coefficient $D_{eff} = V_{eff}^2 T_\theta$ in a broad range with respect to the turbulent diffusion coefficient D_t.

(ii) The anisotropic shape of the pacman-shaped particle has a strong impact on its locomotion. In these experiments, pacman-shaped particles are sectors of circular discs with two geometric parameters: the radius r_s and the angle of the cut-out sector α. When the radius is varied and α is maintained at $90°$, we find that the particles extract the same amount of energy E_s from the turbulent flow regardless of the size ratio. The propulsion relies on the fraction of this energy that fuels the effective propulsive velocity V_{eff}, which can be characterised by the propulsive parameter β. Generally,

the larger the size ratio, the better the conversion of E_s into directed motion. When the radius of the pacman-shaped particle is fixed ($r_s/L_f > 1$) and α is varied, an optimum shape is identified, when α is equal to $90°$. Pacman-shaped particles with a $90°$ cut-out sector maximise both the kinetic energy harvested from the turbulent flow (E_s) and the fraction of the energy transferred to the directed propulsive motion (β).

The latter point suggests that efficient passive locomotion relies on a trade-off: on one hand, the angle α must be large enough for the particle to interact with the turbulent eddies; on the other hand, a large α substantially lowers the moment of inertia, and will therefore lead to increased angular fluctuations and less efficient propulsion. This trade-off is clearly captured by the behaviour of β versus α shown in Figure 4.17. However, if α exceeds $90°$, the solid boundary of the particle cannot provide proper guidance to the river-like fluid bundle structures, which leads to a deduction in propulsion. The dynamics and the mechanism of energy transfer for these particles may be different.

In the context of exploiting the energy of turbulent flows, one concern is to estimate the range of eddies with different sizes that can efficiently fuel a propulsion mechanism. This question is, for example, of interest for both engineering applications (e.g. propulsion generation by flow-structure coupling) and research in biology (e.g. passive swimming) [1, 4, 90, 68]. In these two domains, an object (or a fish) is always modelled to interact with eddies of comparable size among the hierarchy of turbulent eddies. This assumes that there is some kind of 'localness' of the transfer of energy (here, *local* means that interactions mostly occur between the object and eddies of comparable size). Such a model would predict that a pacman-shaped particle with large size ratio would interact with the most energy-containing eddies and therefore extract more energy from the turbulent flow at this scale. However, our results in Figure 4.16 clearly demonstrate that the extracted energy E_s is constant over a broad range of sizes if $r_s/L_f > 1$.

Our understanding of the flow-particle coupling is based on the characterisation

of the Lagrangian structure in 2D turbulence. More precisely, it was shown that the Kraichnan scaling $k^{-5/3}$ measured in the Eulerian frame can correspond to the interacting river-like structures in the Lagrangian frame. These rivers are elongated structures whose statistical length is much longer than their characteristic width L_f. Indeed, the forcing scale L_f interacts with larger scales to give birth to the river-like structures [116]. The observation also indicates that a level of non-locality might exist in the transfer of energy in the wave-driven turbulence. It also suggests that the coupling of the particle to the flow fabric is also non-local, as these particles are able to extract energy from the entire inertial interval in our experiments.

On a fundamental level, the propulsion mechanism for the pacman-shaped particle may also provide an alternative physical mechanism for spectral condensation in 2D turbulent flow. The energy transfers from small to larger scales in 2D turbulence, which results in a steady-state inertial range and generates a spectral condensate under certain conditions [53, 88, 120]. The mechanism of the 2D inverse cascade and the formation of the condensate, however, remain controversial. Among the most plausible theories are those suggesting that the inverse cascade arises from (1) vortex merger, via the process whereby smaller vortices combine to form larger ones [66], (2) a clustering of like-sign vortices [75], and (3) the elongation and thinning of small-scale vortices by large-scale strain, which weakens their velocity and transfers their energy upscale [17]. As has been discussed before, the formation of the spectral condensation might be a result of the interaction of the solid boundaries and the underlying coherent structures in 2D turbulence.

Summary and future work

In the present work, we have investigated the dispersion of finite-size anisotropic particles in 2D turbulence. It is a surface flow generated by Faraday waves (FWT). A wide range of particle sizes and forcing scales L_f are studied. For the analysis of the particle motion, both of translational and rotational transport dynamics are considered.

First, we present experimental results on the dispersion of ellipsoidal particles in FWT. The turbulent transport of these anisotropic objects is strongly affected by the underlying fabric of the flow. This fabric is made up of a network of coherent river-like structures with a characteristic width close to the turbulent flow forcing scale L_f. By studying the PDF of the angle of attack (AOA) of θ_v and θ_p, it is found that the preferential diffusing direction is highly dependent on the size ratio of the major axis of ellipsoids (aa) to the forcing scale (L_f). *Large* ellipsoids ($aa > L_f$) can interact with many bundles, and consequently diffuse faster in the direction parallel to their major axes. This behaviour is reminiscent of the dynamics of the Brownian motion of an isolated ellipsoidal particle in a thermal bath. By contrast, *small* ellipsoids ($aa < L_f$) diffuse faster in the direction transverse to their major axes. This is due to the effective momentum transfer from the underlying coherent structure to the minor axes of the ellipsoids. Similar behaviour has been reported by introducing an ellipsoidal particle into a active bacterial suspension. The different behaviours of *large* and *small* ellipsoids in this thesis are attributed to the interaction of these anisotropic particles with the structure of 2D turbulent flows, containing meandering coherent bundles. A coupling between the translational and rotational motion of the ellipsoidal particles

is also observed.

To utilise the interaction of the coherent bundles and passive particles, we designed a pacman-shaped particle, which is a circular disc with a cut-out sector. Such model anisotropic particle is suitable for capturing the essential features of their interaction with the underlying turbulence. It is found that the pacman-shaped particle can modify the flow around, and divert the motion of fluid particles within the coherent river-like structures. Through the fluid-particle interaction, a passive propulsion force is generated, thus affecting the motion of the particles. Pacman-shaped particles with large size ratios (for example r_s/L_f = 9.09) exhibit highly directional motion, while particles with small size ratios (for example r_s/L_f = 2.5) shows random motion with erratic trajectories. The dispersion of the pacman-shaped particle depends on the coupling between translational motion and rotational motion, which can be tuned by altering the particle shape and its size relative to the characteristic scale of the underlying turbulence. The results show that the behaviours of pacman-shaped particles are due to a competition between (1) the propulsive events, where the two orientations θ_v and θ_p are strongly aligned (domain $\Delta 1$) and (2) the rotational dynamics, which are governed by the rotational characteristic time T_θ. The dynamics of the pacman-shaped particle can be understood with reference to the frames of active particles with self-propelling ability. By analysing the impact of shapes with different cut-out sectors α, both the passive propulsion generated and the kinetic energy extracted from the turbulent flows can be maximised. The optimal shape is identified as $\alpha = 90°$.

The results of both experiments demonstrate that the ratio between the characteristic scale of the particle and the forcing scale of the flow is a trigger for several different behaviours. We have shown that the normalised particle size aa/L_f is a critical parameter for preferential diffusion direction of ellipsoidal particles. Also, by changing the particle size ratio r_s/L_f, the propulsive lengths of the pacman-shaped particles are affected significantly. This result is consistent with the previous findings regarding finite-size isotropic particles where the diffusion coefficients of circular discs under-

went a sharp decrease when the particle size was close to the forcing scale. We further find that the transport of anisotropic finite-size particles in 2D turbulence is determined by the efficient interaction of its geometric shape with the fabric of turbulent flow. This interaction leads to a translation-rotation coupling that either defines the preferential diffusing direction or gives rise to strong propulsive events. Similar coupling effects have only been reported in certain cases, such as active particles that are able to generate propulsion, finite-size particles with lift force, and passive particles in active suspensions [6, 45, 129, 79, 5].

Current studies can be further explored and extended in different directions, such as:

(1) The turbulence-driven locomotion of different anisotropic objects in order to get a universal model describing the macroscopic consequences of particles with different shapes [36, 49]. For example, the passive swimming mechanism of aquatic organisms relies on structural components of the body, which are anisotropic. New insights into passive propulsion by different shapes of particles in a turbulent flow can be exploited to promote the development of advanced propulsive technologies, as well as the understanding of aquatic propulsion [4, 31].

(2) The collective dynamics of multiple particles in turbulence. Aggregation phenomena (flocculation, coagulation and/or coalescence) often have a profound effect on the properties of the dispersion of particles in many natural and industrial flows. Turbulence, for example, can enhance the encounter rates between different species of microorganisms, either swimming or passively advected by the flow. Even in the absence of turbulence, elongated particles collide frequently by virtue of their orientation-dependent velocity [92]. Further experimental measurements of the collective dynamics of multiple particles in turbulent flows may help to facilitate a better understanding of these phenomena.

Our experiments bring us a step closer to an understanding of the transport of

finite-size anisotropic particles in 2D turbulent flows. In addition to the dynamics of particles during their dispersion in turbulence, the fundamental research presented in this project may also have potential implications for sorting inertial particles in microfluidics [22], industrial process such as papermaking [60], search and rescue optimal planning [104], and understanding the drift of sea ice [39] or ocean buoys [105].

Appendix

Appendix A:
Tracking of pacman-shaped particles

In order to track the orientation of a pacman-shaped particle, two important geometric parameters of a particle are identified: centre of mass (COM) and centre of geometry (COG). The COM and COG positions for different particles are shown in Figure 6.1. For a pacman-shaped particle, the COM is located at the bisector of the particle (grey dot), while the COG is defined as the apex of the cut-out sector (black dot). For a circular disc, COM and COG are coincident and located in the centre. For the convenience of further analysis, a quarter of the circular disc is shaded in grey, such that they can be treated as pacman-shaped particles using the same analysis framework and image analysis algorithms.
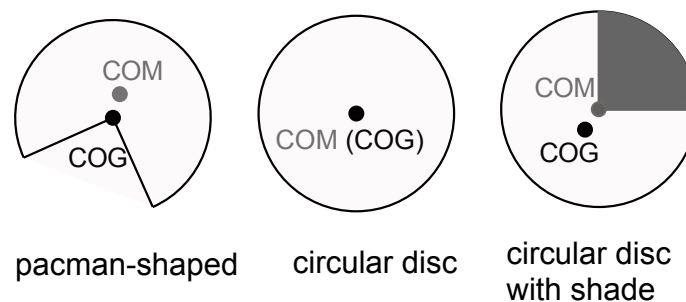
Figure 6.1: Definition of centre of mass (COM) and centre of geometry (COG) for both pacman-shaped particle and circular disc (w/o shade)
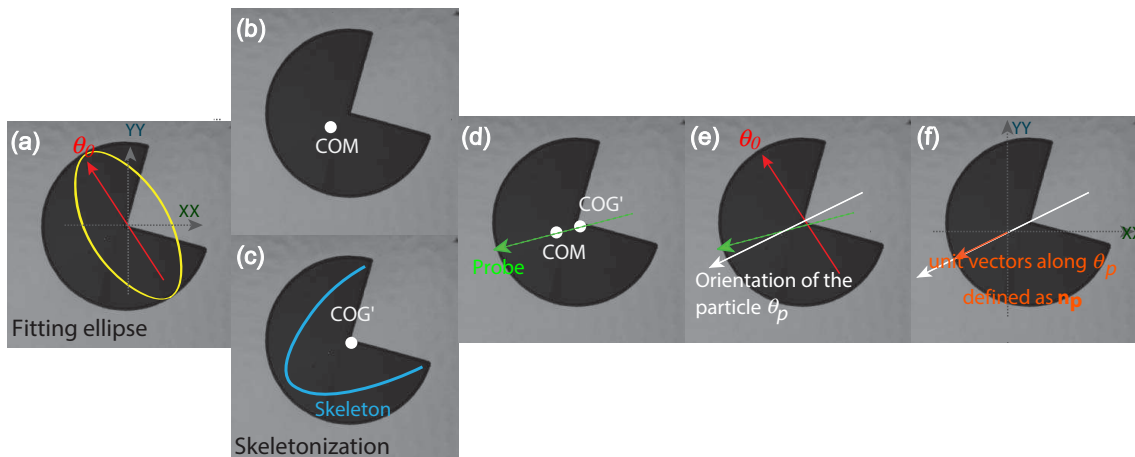
Figure 6.2: The approach of tracking the orientation of the floaters θ_p and the deposited unit vectors

The orientation of a pacman-shaped particle, θ_p, is the direction starting from the COG and moving towards the COM. It is defined as the angle between the bisector direction of the particle and the XX axis in the Cartesian coordinate.

Several steps are needed to obtain the orientation of the particle θ_p as follows:

(1) Getting the raw orientation of the particle. As shown in Figure 6.2 (a), fitting an ellipse to the pacman-shaped particle will give us θ_0, which is the orientation of major axis along the fitted ellipsoid. However, this direction points to the side wings of the pacman-shaped particle, while the true orientation of the particle θ_p faces orthogonal to θ_0 as $\theta_p = \theta_0 \pm 90\,°$. A further analysis step is required to identify the orientation of the particle.

(2) Getting the COM and COG positions of the pacman. By applying the 'Centre of Mass' module to the pacman, COM is easy to access, as shown in Figure 6.2 (b). However, there is no direct tool for use in obtaining the COG position. Thus, the 'Skeletonisation' function in ImageJ is first applied to the pacman particle, which gives us the skeleton of the particle, as shown in blue in Figure 6.2 (c). By applying the 'Centre of Mass' module to the skeleton, one is able to get a position that is very close to the COG, denoted as COG'. Due to distortion during recording and pre-processing

of the raw movies, COG and COG$'$ do not coincide.

(3) Taking the direction from COG$'$ to COM. The illustration of analysis step is listed in Figure 6.2 (d). With this additional vector information, one can determine the side wing of the pacman-shaped particle on which the raw orientation θ_0 is located. The true orientation of pacman θ_p is now defined as $\theta_0 + 90°$ in Figure 6.2 (d).

After obtaining the true orientation θ_p, we define the unit vectors along the orientation of the particle as $\mathbf{n_p}$, as illustrated in Figure 6.2 (f). For other shapes of pacman particles for which $\alpha \neq 90°$ and for circular discs with shaded areas, similar procedures are applied.

Appendix B:
The measurement of propulsion force of pacman-shaped particles

(Disclaimer: This work is done in collaboration with Mahdi Davoodianidalik, who developed the force measurement technique.)

When the propulsion effect is strong ($r_s/L_f > 6$), a pacman-shaped particle moves predominantly in a directed locomotion. The direction of this motion is prescribed by its asymmetry of the anisotropic shape. The mechanism of propulsion generated by pacman-shaped particles is identical to the one that fuels the turbulence-driven rotor which has been reported recently [36]. In our experiment, we demonstrate that the main component of the propulsion force acts along the bisector of the particle's corner and pushes the pacman-shaped particle forward. Moreover, it is shown that the key to the extraction of useful work from wave-driven 2D turbulence is the efficient coupling of the particle to coherent, yet transient structures presented in the flow.

In the wave-driven turbulence, a large number of fluid particles travel in a correlated manner along transient river-like structures (bundle) whose statistical widths are close to L_f. Far from wall boundaries, these bundles of fluid particle trajectories execute a complex collective motion, being constantly and randomly bent by the surrounding turbulent flow. In the vicinity of a wall, these bundles are guided by the solid boundary (wall) of the particle. Bundles experience a sharp change of direction inside the cut-out sector. In response to the centripetal acceleration experienced by the bundle, a reaction force F_{prop} acts along the bisector of the pacman's cut-out sector as the passive propulsion force, as seen in the schematic Figure 6.3. This is how coherent fluid bundles transfer their momentum to the aisotropic shapes of finite-size pacmans.

For the case of the rotating rotor, a model was proposed for the propulsive force exerted on a rotor in the wave-driven turbulent flows [36]. This model predicted a

mean propulsive force $\langle F_{prop} \rangle \sim \langle u \rangle$, where $\langle u \rangle$ is the r.m.s turbulent flow velocity. This dependence was only tested indirectly by measuring the angular velocity of the rotor.
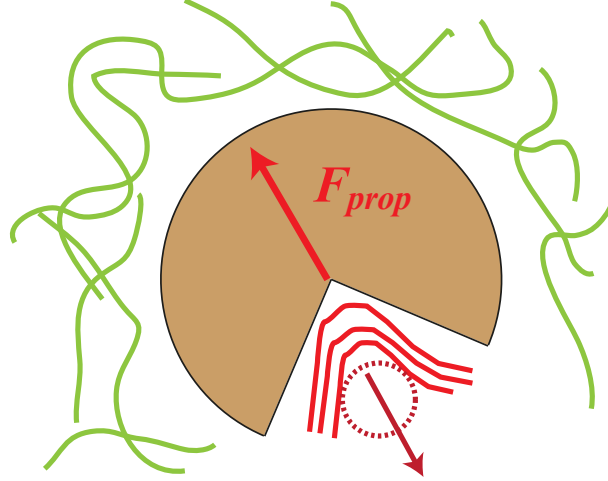
Figure 6.3: Schematics illustrating the propulsion force F_{prop} generated by the bending of a fluid bundle (red trajectories) inside the corner shaped edge of the pacman-shaped particles. The trajectories of fluid particles (in green) in the outer domain are not guided and behave randomly.

In this experiment, we use an optical fibre cantilever as a force probe to measure the hydrodynamic forces exerted on a circular disc or a pacman by 2D turbulence. The optical fibre cantilever has been used as a velocimetry probe in turbulent soap film channels [50]. Later, it was extended as a force probe in the context of microscale rheology of flowing polymer solutions [33, 32]. A schematic of the force measurement set-up is shown in Figure 6.4. The glass fibre is 10 cm long and has a diameter D_f of 80 μm. It is fixed to a syringe needle at one of its end while its other end passes through a hole which is located close to the centre of the disc or the apex of the particle's cut-out sector. In this configuration, the fibre can slide within the hole when the floating particle moves away from its initial position. This ensures that the fibre applies no vertical force on the particle and that the friction force between the fibre and the particle is minimal.

The fibre deflection d is measured in time, which gives us the access to calculate

the elastic force F_e exerted on the fibre cantilever by our finite-size particles. Typically the deflection is in the range $1 < d < 20$ mm and is measured with a spatial resolution of 0.2 mm. The hydrodynamics forces exerted by the flow on the particles are measured which are typically in the range of (1-100) μN.
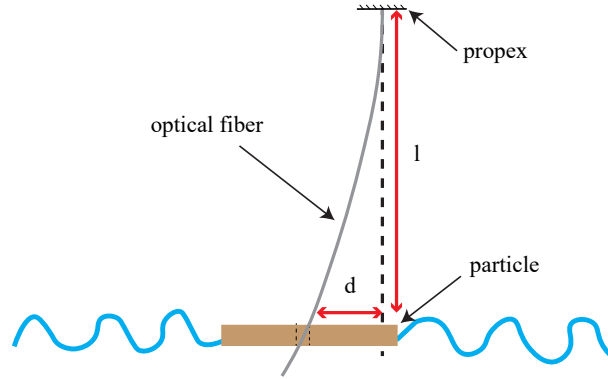
Figure 6.4: Schematics illustrating the force measurement method based on the optical fibre cantilever. The measurement of the deflection d of the fibre gives the hydrodynamic force exerted by the turbulent flows on the pacman-shaped particles.

Since the deflection is much smaller than the fibre length, we use Hooke's law to derive the force:

$$F = \frac{3\pi E (D_f)^4 d}{64 L^3} \tag{6.1}$$

with the Young modulus of glass $E = 90$ GPa and $L = 10$ cm the fibre length. We have selected this length because it provides a high resolution for the force measurements while making sure that the inverse of the fibre resonance frequency is smaller than the average time scale of the hydrodynamics fluctuations. In this condition, the fibre inertia can be neglected.

The principle of the measurement is that the elastic force F_e balances the hydrodynamic force acting on the floating finite-size particle. In the case of a pacman, the force balance can be written as $F_e = F_{turb} + F_{prop}$, where the hydrodynamic force has been split into two components: F_{turb} is the *fast* non-propulsive component of the force exerted by the turbulent flow fluctuations. While F_{prop} is the propulsive force with a *slow* dynamics. Here the *fast* and *slow* dynamics are presented by the Lagrangian

velocity auto correlation functions shown before. To ensure reliable measurements of these two components, forces are measured at a 10 Hz sampling rate for 10 minutes.
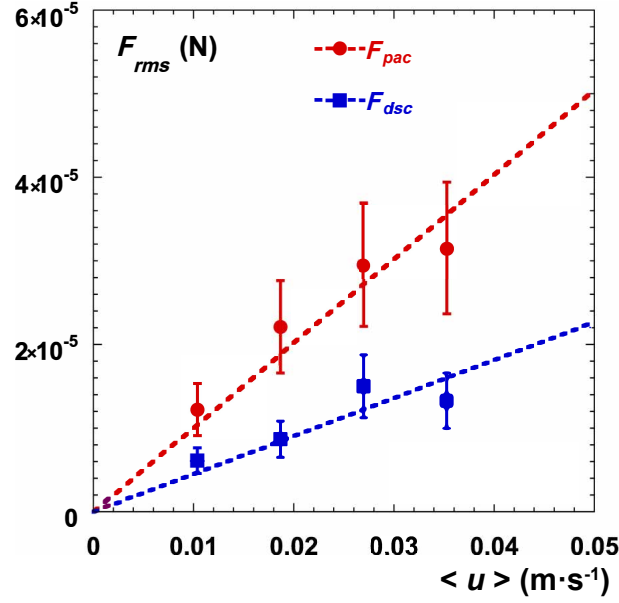
Figure 6.5: F_{pac} and F_{disc} versus the flow r.m.s velocity $\langle u \rangle$ for $r_s/L_f = 6.18$ and $L_f = 4.4$ mm. F_{disc} is the averaged r.m.s force measured in the case of a disc, while $F_{prop} = F_{pac} - F_{disc}$ with F_{pac} the averaged r.m.s force measured in the case of a pacman-shaped particle.

Figure 6.5 shows the r.m.s value of the elastic force measured for a disc and a pacman of the same size for various r.m.s flow velocity $\langle u \rangle$. To distinguish the two cases, the r.m.s value of the elastic forces are called F_{disc} and F_{pac} respectively. It shows that the force exerted by the turbulent flow on a pacman is larger than the one acting on a disc, $F_{pac} > F_{disc}$. Both F_{disc} and F_{pac} increase linearly with the higher level of turbulent velocity fluctuations $\langle u \rangle$. In the case of the disc, the elastic force measurements give the turbulent non-propulsive force $F_{disc} = \langle F_{turb} \rangle$, where $\langle \rangle$ denotes r.m.s and statistical averaging. If we assume that $\langle F_{turb} \rangle$ is similar for a disc and a pacman with identical size, then the r.m.s propulsive force can be computed as $\langle F_{prop} \rangle = F_{pac} - F_{disc}$ and we find that $\langle F_{prop} \rangle \sim \langle u \rangle$, which shows good agreement with the model proposed in the rotating rotor in wave-driven turbulence [36].

Appendix C: Nomenclature

All the variables and abbreviations presented in this thesis are listed as follows.

1. Alphabetic letters

aa and *bb*: major and minor sizes of ellipsoidal particle

a: vertical acceleration

a_v: linear velocity dissipation rate

a_{th}: critical acceleration threshold

C and *Cı*: dimensionless Kolmogorov constants

$C(t)$: mixed cross-correlation function

d: fibre deflection

d_{12}: initial distance between two different fluid particles

D: diffusion coefficient

D_{aa} and D_{bb}: diffusion coefficient in the body frame of references of ellipsoidal particle

D_θ: rotational diffusion coefficient

D_t: diffusion coefficient of turbulent transport

D_{eff}: effective diffusion coefficient

D_f: diameter of the glass fibre

E: Young modulus of glass

E_k: wave number spectra of the kinetic energy

E_s: kinetic energy of pacman-shaped particle

f: forcing frequency of fluid flow

F_{prop}: propulsive force

F_{turb}: force exert by turbulent flow fluctuations

F_e: elastic force

F_{pac}: root mean square value of elastic force of pacman-shaped particle

F_{pac}: root mean square value of elastic force of pacman-shaped particle

g: gravity acceleration

k: wave number

k_f: wave number of forcing scale

k_v: wave number of the dissipative scale

l: length of the glass fibre

L: bounded domain size

L_d: dissipative scale

L_f: forcing scale of the flow

L_β: propulsive length

L_t: turbulent transport

M_s: mass of pacman-shaped particle

$\mathbf{n_p}$: unit vector along the orientation of the pacman-shaped particle

$\mathbf{n_{px}}$ and n_{py} decomposed components of n_p

$\mathbf{n_v}$: unit vector along the velocity orientation of the pacman-shaped particle

r_p: object size

r: radius of circular disc

r_s: radius of pacman-shaped particle

R_c: radius of the container

Δr total displacement of particle

Δr_x and Δr_y: displacements of particle in the lab frame of reference

Δr_{aa} and Δr_{bb}: displacements of particle in the body frame of reference

$\langle r^2 \rangle$: mean-squared displacement

t: time

Δt: time interval

T_L and T_{12}: Lagrangian characteristic time scales

T_m: typical time of a measurement

T_f: characteristic time scales of fluid flows

T_{disc}: characteristic time scale of circular disc

T_{aa} and T_{bb}: characteristic time scales of ellipsoidal particle in the body frame of reference

T_ω: rotational characteristic time of angular velocity

T_θ: rotational characteristic time of orientational unit vector

u: characteristic velocity of fluid particles

$\langle u^2 \rangle$: variance of the turbulent velocity fluctuations

v_x: v_y and u_x: u_y, velocity components of fluid particles

$v_r ms$: root mean square velocity of particle

$\langle v_{aa}^2 \rangle$ and $\langle v_{bb}^2 \rangle$: kinetic energy of ellipsoid particle in the body frame of reference

$|V_p|$: particle velocity modulus

$\langle V_p^2 \rangle$: root mean square of pacman-shaped particle

V_{p1}: V_{p2} and V_{p3}, average velocity of particles in angular domains $\Delta 1$, $\Delta 2$ and $\Delta 3$

V_{disc}: average velocity of circular disc

V_{eff}: effective propulsive velocity

V_{turb}: velocity of turbulent flow

(x_t, y_t): location coordinate of the particle at time t

XX and YY: axes of lab frame of reference

X_{aa} and X_{bb}: axes of body frame of reference

2. Greek letters

α: angle of cut-out sector of the pacman-shaped particle

β: propulsive parameter

$\Delta 1$, $\Delta 2$ and $\Delta 3$: angular domains

η and ϵ: flux of the energy and the enstrophy

γ: aspect ratio of ellipsoidal particle

λ: Faraday wavelength

ω: angular frequency of liner waves

ω_t: angular velocity of particle

ρ: density of the fluid

ρ_{11}: auto-correlation function of the same fluid particle

ρ_{12}: directional cross-correlation function of different fluid particles

$\rho(t)$: auto-correlation function of Lagrangian velocity

$\rho(\omega)$: auto-correlation function of angular velocity

$\rho(n_p)$: auto-correlation function of orientational unit vector

σ: surface tention

σ^2: velocity variance

τ: period of time

θ_0: initial orientation of particle

θ_{aa}: orientation of ellipsoidal particle

θ_p: orientation of the pacman-shaped particle

θ_v: orientation of particle velocity

$\Delta\theta$: angular difference between θ_{aa} and θ_v of ellipsoidal particle $\Delta\theta_p$: angular difference of pacman-shaped particle in a time interval

$\Delta\theta_{pv}$: angle difference between θ_p and θ_v of pacman-shaped particle

$\langle\Delta\theta^2\rangle$: mean-squared angular displacement

ξ_{aa} and ξ_{bb}: friction factors of ellipsoidal particle in the body frame of reference

3. Abbreviations

2D: two-dimensional

AOA: angle of attack

ACF: auto-correlation function

COM: centre of mass

COG: centre of geometry

EMT: electromagnetically driven turbulence

FWT: Faraday wave driven turbulence

IDL: Interactive data language

MSD: mean-squared displacement

MSAD: mean-squared angular displacement

MCC: mixed cross-correlation function

PDF: probably density function

PIV: particle image velocimetry

PTV: particle tracking velocimetry

SBT: slender body theory

Bibliography

1. Allen, J. J. and Smits, A. J. (2001). Energy harvesting eel. *Journal of Fluids and Structures*, 15(3):629–640.

2. Alméras, E., Mathai, V., Sun, C., and Lohse, D. (2019). Mixing induced by a bubble swarm rising through incident turbulence. *International Journal of Multiphase Flow*, 114:316–322.

3. Batchelor, G. (1970). Slender-body theory for particles of arbitrary cross-section in stokes flow. *Journal of Fluid Mechanics*, 44(3):419–440.

4. Beal, D., Hover, F., Triantafyllou, M., Liao, J., and Lauder, G. V. (2006). Passive propulsion in vortex wakes. *Journal of Fluid Mechanics*, 549:385–402.

5. Bechinger, C., Di Leonardo, R., Löwen, H., Reichhardt, C., Volpe, G., and Volpe, G. (2016). Active particles in complex and crowded environments. *Reviews of Modern Physics*, 88(4):045006.

6. Berg, H. C. (1993). *Random walks in biology*. Princeton, New Jersey, United States, Princeton University Press.

7. Beron-Vera, F. J., Olascoaga, M. J., and Miron, P. (2019). Building a maxey–riley framework for surface ocean inertial particle dynamics. *Physics of Fluids*, 31(9):096602.

8. Bian, X., Kim, C., and Karniadakis, G. E. (2016). 111 years of brownian motion. *Soft Matter*, 12(30):6331–6346.

9. Boffetta, G. and Ecke, R. E. (2012). Two-dimensional turbulence. *Annual Review of Fluid Mechanics*, 44:427–451.

10. Boffetta, G. and Sokolov, I. M. (2002). Statistics of two-particle dispersion in two-dimensional turbulence. *Physics of Fluids*, 14(9):3224–3232.

11. Bourgoin, M., Ouellette, N. T., Xu, H., Berg, J., and Bodenschatz, E. (2006). The role of pair dispersion in turbulent flow. *Science*, 311(5762):835–838.

12. Brown, R. D., Warhaft, Z., and Voth, G. A. (2009). Acceleration statistics of neutrally buoyant spherical particles in intense turbulence. *Physical Review Letters*, 103(19):194501.

13. Burgers, J. M. (1938). On the motion of small particles of elongated form suspended in a viscous liquid. *Kon. Ned. Akad. Wet. Verhand.(Eerste Sectie)*, 16:113–184.

14. Byron, M., Einarsson, J., Gustavsson, K., Voth, G., Mehlig, B., and Variano, E. (2015). Shape-dependence of particle rotation in isotropic turbulence. *Physics of Fluids*, 27(3):035101.

15. Calzavarini, E., Jiang, L., and Sun, C. (2020). Anisotropic particles in two-dimensional convective turbulence. *Physics of Fluids*, 32(2):023305.

16. Calzavarini, E., Volk, R., Bourgoin, M., Lévêque, E., Pinton, J.-F., and Toschi, F. (2009). Acceleration statistics of finite-sized particles in turbulent flow: The role of faxén forces. *Journal of Fluid Mechanics*, 630:179–189.

17. Chen, S., Ecke, R. E., Eyink, G. L., Rivera, M., Wan, M., and Xiao, Z. (2006). Physical mechanism of the two-dimensional inverse energy cascade. *Physical Review Letters*, 96(8):084502.

18. Chertkov, M., Connaughton, C., Kolokolov, I., and Lebedev, V. (2007). Dynamics of energy condensation in two-dimensional turbulence. *Physical Review Letters*, 99(8):084501.

19. Cox, R. (1970). The motion of long slender bodies in a viscous fluid part 1. general theory. *Journal of Fluid Mechanics*, 44(4):791–810.

20. Cox, R. (1971). The motion of long slender bodies in a viscous fluid part 2. shear flow. *Journal of Fluid Mechanics*, 45(4):625–657.

21. Crowe, C., Gore, R., and Troutt, T. (1985). Particle dispersion by coherent structures in free shear flows. *Particulate Science and Technology*, 3(3-4):149–158.

22. Di Carlo, D. (2009). Inertial microfluidics. *Lab on a Chip*, 9(21):3038–3046.

23. Dombrowski, C., Cisneros, L., Chatkaew, S., Goldstein, R. E., and Kessler, J. O. (2004). Self-concentration and large-scale coherence in bacterial dynamics. *Physical Review Letters*, 93(9):098103.

24. Dunkel, J., Heidenreich, S., Drescher, K., Wensink, H. H., Bär, M., and Goldstein, R. E. (2013). Fluid dynamics of bacterial turbulence. *Physical Review Letters*, 110(22):228102.

25. Einstein, A. (1905). Über die von der molekularkinetischen theorie der wärme geforderte bewegung von in ruhenden flüssigkeiten suspendierten teilchen. *Annalen der Physik*, 322(8):549–560.

26. Einstein, A. (1906). Eine neue bestimmung der moleküldimensionen. *Annalen der Physik*, 324(2):289–306.

27. Einstein, A. (1956). *Investigations on the theory of the Brownian movement*. Chelmsford, MA, United States, Courier Corporation.

28. Falkovich, G., Boffetta, G., Shats, M., and Lanotte, A. (2017). Introduction to focus issue: Two-dimensional turbulence. *Physics of Fluids*, 29(11):110901.

29. Falkovich, G., Fouxon, A., and Stepanov, M. (2002). Acceleration of rain initiation by cloud turbulence. *Nature*, 419(6903):151–154.

30. Faxén, H. (1922). Der widerstand gegen die bewegung einer starren kugel in einer zähen flüssigkeit, die zwischen zwei parallelen ebenen wänden eingeschlossen ist. *Annalen der Physik*, 373(10):89–119.

31. Fish, F. and Lauder, G. V. (2006). Passive and active flow control by swimming fishes and mammals. *Annual Review of Fluid Mechanics*, 38:193–224.

32. Francois, N., Amarouchene, Y., Lounis, B., and Kellay, H. (2009). Polymer conformations and hysteretic stresses in nonstationary flows of polymer solutions. *EPL (Europhysics Letters)*, 86(3):34002.

33. Francois, N., Lasne, D., Amarouchene, Y., Lounis, B., and Kellay, H. (2008). Drag enhancement with polymers. *Physical Review Letters*, 100(1):018302.

34. Francois, N., Xia, H., Punzmann, H., Ramsden, S., and Shats, M. (2014). Three-dimensional fluid motion in faraday waves: Creation of vorticity and generation of two-dimensional turbulence. *Physical Review X*, 4(2):021021.

35. Francois, N., Xia, H., Punzmann, H., and Shats, M. (2013). Inverse energy cascade and emergence of large coherent vortices in turbulence driven by faraday waves. *Physical Review Letters*, 110(19):194501.

36. Francois, N., Xia, H., Punzmann, H., and Shats, M. (2018). Rectification of chaotic fluid motion in two-dimensional turbulence. *Physical Review Fluids*, 3(12):124602.

37. Gatignol, R. (1983). The faxén formulae for a rigid particle in an unsteady non-uniform stokes flow. *Journal de Mécanique Théorique et Appliqué*, 1:143–160.

38. Gerashchenko, S., Sharp, N., Neuscamman, S., and Warhaft, Z. (2008). Lagrangian measurements of inertial particle accelerations in a turbulent boundary layer. *Journal of Fluid Mechanics*, 617:255.

39. Gherardi, M. and Lagomarsino, M. C. (2015). Characterizing the size and shape of sea ice floes. *Scientific Reports*, 5:10226.

40. Green, M. S. (1954). Markoff random processes and the statistical mechanics of time-dependent phenomena part ii. irreversible processes in fluids. *The Journal of Chemical Physics*, 22(3):398–413.

41. Han, Y., Alsayed, A., Nobili, M., and Yodh, A. G. (2009). Quasi-two-dimensional diffusion of single ellipsoids: Aspect ratio and confinement effects. *Physical Review E*, 80(1):011403.

42. Han, Y., Alsayed, A., Nobili, M., Zhang, J., Lubensky, T. C., and Yodh, A. G. (2006). Brownian motion of an ellipsoid. *Science*, 314(5799):626–630.

43. Hänggi, P. and Marchesoni, F. (2009). Artificial brownian motors: Controlling transport on the nanoscale. *Reviews of Modern Physics*, 81(1):387.

44. Hossain, M., Matthaeus, W. H., and Montgomery, D. (1983). Long-time states of inverse cascades in the presence of a maximum length scale. *Journal of Plasma Physics*, 30(3):479–493.

45. Howse, J. R., Jones, R. A., Ryan, A. J., Gough, T., Vafabakhsh, R., and Golestanian, R. (2007). Self-motile colloidal particles: From directed propulsion to random walk. *Physical Review Letters*, 99(4):048102.

46. Huang, R., Chavez, I., Taute, K. M., Lukić, B., Jeney, S., Raizen, M. G., and Florin, E.-L. (2011). Direct observation of the full transition from ballistic to diffusive brownian motion in a liquid. *Nature Physics*, 7(7):576–580.

47. Huang, Y., Ou, W., Chen, M., Lu, Z., Jiang, N., Liu, Y., Qiu, X., and Zhou, Q. (2017). Taylor dispersion in two-dimensional bacterial turbulence. *Physics of Fluids*, 29(5):051901.

48. Jeffery, G. B. (1922). The motion of ellipsoidal particles immersed in a viscous fluid. *Proceedings of the Royal Society of London. Series A, Containing Papers of a Mathematical and Physical Character*, 102(715):161–179.

49. Jo, I., Huang, Y., Zimmermann, W., and Kanso, E. (2016). Passive swimming in viscous oscillatory flows. *Physical Review E*, 94(6):063116.

50. Kellay, H., Wu, X., and Goldburg, W. (1995). Experiments with turbulent soap films. *Physical Review Letters*, 74(20):3975.

51. Kheifets, S., Simha, A., Melin, K., Li, T., and Raizen, M. G. (2014). Observation of brownian motion in liquids at short times: instantaneous velocity and memory loss. *Science*, 343(6178):1493–1496.

52. Kraichnan, R. H. (1967). Inertial ranges in two-dimensional turbulence. *The Physics of Fluids*, 10(7):1417–1423.

53. Kraichnan, R. H. and Montgomery, D. (1980). Two-dimensional turbulence. *Reports on Progress in Physics*, 43(5):547.

54. Kubo, R. (1957). Statistical-mechanical theory of irreversible processes part i. general theory and simple applications to magnetic and conduction problems. *Journal of the Physical Society of Japan*, 12(6):570–586.

55. Langevins, P. (1908). Sur la théorie du mouvement brownien [on the theory of brownian motion]. *Comptes rendus de l'Académie des Sciences*, 146:530–533.

56. Lauga, E. and Powers, T. R. (2009). The hydrodynamics of swimming microorganisms. *Reports on Progress in Physics*, 72(9):096601.

57. Li, T., Kheifets, S., Medellin, D., and Raizen, M. G. (2010). Measurement of the instantaneous velocity of a brownian particle. *Science*, 328(5986):1673–1675.

58. Li, T. and Raizen, M. G. (2013). Brownian motion at short time scales. *Annalen der Physik*, 525(4):281–295.

59. Lindner, A. and Shelley, M. (2015). *Elastic fibers in flows*. London, United Kingdom, Royal Society of Chemistry.

60. Lundell, F., Söderberg, L. D., and Alfredsson, P. H. (2011). Fluid mechanics of papermaking. *Annual Review of Fluid Mechanics*, 43:195–217.

61. Marcus, G. G., Parsa, S., Kramel, S., Ni, R., and Voth, G. A. (2014). Measurements of the solid-body rotation of anisotropic particles in 3d turbulence. *New Journal of Physics*, 16(10):102001.

62. Masuda, H., Higashitani, K., and Yoshida, H. (2006). *Powder technology: Fundamentals of particles, powder beds, and particle generation*. Cleveland, OH, United States, CRC press.

63. Mathai, V., Huisman, S. G., Sun, C., Lohse, D., and Bourgoin, M. (2018). Dispersion of air bubbles in isotropic turbulence. *Physical Review Letters*, 121(5):054501.

64. Mathai, V., Neut, M. W., van der Poel, E. P., and Sun, C. (2016). Translational and rotational dynamics of a large buoyant sphere in turbulence. *Experiments in Fluids*, 57(4):51.

65. Maxey, M. R. and Riley, J. J. (1983). Equation of motion for a small rigid sphere in a nonuniform flow. *The Physics of Fluids*, 26(4):883–889.

66. McWilliams, J. C. (1990). The vortices of two-dimensional turbulence. *Journal of Fluid mechanics*, 219:361–385.

67. Mendelson, N. H., Bourque, A., Wilkening, K., Anderson, K. R., and Watkins, J. C. (1999). Organized cell swimming motions in bacillus subtilis colonies: Patterns of short-lived whirls and jets. *Journal of Bacteriology*, 181(2):600–609.

68. Michelin, S. and Doaré, O. (2013). Energy harvesting efficiency of piezoelectric flags in axial flows. *Journal of Fluid Mechanics*, 714:489–504.

69. Monin, A. S. and Yaglom, A. M. (1971). *Statistical fluid mechanics, volumes. I and II*. Cambridge, Ma, United States, The MIT Press.

70. Mordant, N., Metz, P., Michel, O., and Pinton, J.-F. (2001). Measurement of lagrangian velocity in fully developed turbulence. *Physical Review Letters*, 87(21):214501.

71. Nathan, R., Katul, G. G., Horn, H. S., Thomas, S. M., Oren, R., Avissar, R., Pacala, S. W., and Levin, S. A. (2002). Mechanisms of long-distance dispersal of seeds by wind. *Nature*, 418(6896):409–413.

72. Ni, R., Kramel, S., Ouellette, N. T., and Voth, G. A. (2015). Measurements of the coupling between the tumbling of rods and the velocity gradient tensor in turbulence. *Journal of Fluid Mechanics*, 766:202–225.

73. Ni, R., Ouellette, N. T., and Voth, G. A. (2014). Alignment of vorticity and rods with lagrangian fluid stretching in turbulence. *Journal of Fluid Mechanics*, 743:R3.

74. Ouellette, N. T., O'Malley, P., and Gollub, J. P. (2008). Transport of finite-sized particles in chaotic flow. *Physical Review Letters*, 101(17):174504.

75. Paret, J. and Tabeling, P. (1997). Experimental observation of the two-dimensional inverse energy cascade. *Physical Review Letters*, 79(21):4162.

76. Paret, J. and Tabeling, P. (1998). Intermittency in the two-dimensional inverse cascade of energy: Experimental observations. *Physics of Fluids*, 10(12):3126–3136.

77. Parsa, S., Calzavarini, E., Toschi, F., and Voth, G. A. (2012). Rotation rate of rods in turbulent fluid flow. *Physical Review Letters*, 109(13):134501.

78. Parsa, S., Guasto, J. S., Kishore, M., Ouellette, N. T., Gollub, J., and Voth, G. A. (2011). Rotation and alignment of rods in two-dimensional chaotic flow. *Physics of Fluids*, 23(4):043302.

79. Peng, Y., Lai, L., Tai, Y.-S., Zhang, K., Xu, X., and Cheng, X. (2016a). Diffusion of ellipsoids in bacterial suspensions. *Physical Review Letters*, 116(6):068303.

80. Peng, Y., Lai, L., Tai, Y.-S., Zhang, K., Xu, X., and Cheng, X. (2016b). Diffusion of ellipsoids in bacterial suspensions [supplementary material]. *Physical Review Letters*, 116(6):068303.

81. Perrin, F. (1934). Brownian motion of an ellipsoid-i. dielectric dispersion for ellipsoidal molecules. *Journal de Physique et le Radium*, 5(10):497–511.

82. Perrin, J. (1914). *Les atomes*. New York, New York, United States, Van Nostrand Company.

83. Pumir, A. and Wilkinson, M. (2011). Orientation statistics of small particles in turbulence. *New Journal of Physics*, 13(9):093030.

84. Qureshi, N. M., Bourgoin, M., Baudet, C., Cartellier, A., and Gagne, Y. (2007). Turbulent transport of material particles: An experimental study of finite size effects. *Physical Review Letters*, 99(18):184502.

85. Raju, N. and Meiburg, E. (1997). Dynamics of small, spherical particles in vortical and stagnation point flow fields. *Physics of Fluids*, 9(2):299–314.

86. Romanczuk, P. and Schimansky-Geier, L. (2011). Brownian motion with active fluctuations. *Physical Review Letters*, 106(23):230601.

87. Scott, A. (2006). *Encyclopedia of Nonlinear Science*. London, United Kingdom, Routledge.

88. Shats, M., Xia, H., and Punzmann, H. (2005). Spectral condensation of turbulence in plasmas and fluids and its role in low-to-high phase transitions in toroidal plasma. *Physical Review E*, 71(4):046409.

89. Shats, M., Xia, H., and Punzmann, H. (2012). Parametrically excited water surface ripples as ensembles of oscillons. *Physical Review Letters*, 108(3):034502.

90. Shelley, M. J. and Zhang, J. (2011). Flapping and bending bodies interacting with fluid flows. *Annual Review of Fluid Mechanics*, 43:449–465.

91. Shin, M. and Koch, D. L. (2005). Rotational and translational dispersion of fibres in isotropic turbulent flows. *Journal of Fluid Mechanics*, 540:143–173.

92. Słomka, J. and Stocker, R. (2020). On the collision of rods in a quiescent fluid. *Proceedings of the National Academy of Sciences*, 117(7):3372–3374.

93. Smith, L. M. and Yakhot, V. (1993). Bose condensation and small-scale structure generation in a random force driven 2d turbulence. *Physical Review Letters*, 71(3):352.

94. Sokolov, A. and Aranson, I. S. (2012). Physical properties of collective motion in suspensions of bacteria. *Physical Review Letters*, 109(24):248109.

95. Sokolov, I. M. and Reigada, R. (1999). Dispersion of passive particles by a quasi-two-dimensional turbulent flow. *Physical Review E*, 59(5):5412.

96. Sommeria, J. (1986). Experimental study of the two-dimensional inverse energy cascade in a square box. *Journal of Fluid Mechanics*, 170:139–168.

97. Spagnolie, S. (2019). Dropping slender-body theory into the mud. *Journal of Fluid Mechanics*, 862:1–4.

98. Stokes, G. G. (1851). *On the effect of the internal friction of fluids on the motion of pendulums*, volume 9. Pitt Press Cambridge.

99. Taylor, G. I. (1922). Diffusion by continuous movements. *Proceedings of the London Mathematical Society*, 2(1):196–212.

100. Taylor, G. I. (1923). The motion of ellipsoidal particles in a viscous fluid. *Proceedings of the Royal Society of London. Series A, Containing Papers of a Mathematical and Physical Character*, 103(720):58–61.

101. Taylor, G. I. (1954). The dispersion of matter in turbulent flow through a pipe. *Proceedings of the Royal Society of London. Series A. Mathematical and Physical Sciences*, 223(1155):446–468.

102. Toschi, F. and Bodenschatz, E. (2009). Lagrangian properties of particles in turbulence. *Annual Review of Fluid Mechanics*, 41:375–404.

103. Tuck, E. (1964). Some methods for flows past blunt slender bodies. *Journal of Fluid Mechanics*, 18(4):619–635.

104. Ullman, D. S., O'Donnell, J., Kohut, J., Fake, T., and Allen, A. (2006). Trajectory prediction using hf radar surface currents: Monte carlo simulations of prediction uncertainties. *Journal of Geophysical Research: Oceans*, 111(C12).

105. Veras Guimarães, P., Ardhuin, F., Sutherland, P., Accensi, M., Hamon, M., Pérignon, Y., Thomson, J., Benetazzo, A., and Ferrant, P. (2018). A surface kinematics buoy (skib) for wave–current interaction studies. *Ocean Science*, 14(6):1449–1460.

106. Vicsek, T. and Zafeiris, A. (2012). Collective motion. *Physics reports*, 517(3-4):71–140.

107. Volk, R., Calzavarini, E., Leveque, E., and Pinton, J.-F. (2011). Dynamics of inertial particles in a turbulent von kármán flow. *Journal of Fluid Mechanics*, 668:223–235.

108. Volk, R., Calzavarini, E., Verhille, G., Lohse, D., Mordant, N., Pinton, J.-F., and Toschi, F. (2008). Acceleration of heavy and light particles in turbulence: Comparison between experiments and direct numerical simulations. *Physica D: Nonlinear Phenomena*, 237(14-17):2084–2089.

109. Von Kameke, A., Huhn, F., Fernández-García, G., Munuzuri, A., and Pérez-Muñuzuri, V. (2011). Double cascade turbulence and richardson dispersion in a horizontal fluid flow induced by faraday waves. *Physical Review Letters*, 107(7):074502.

110. Voth, G. A., la Porta, A., Crawford, A. M., Alexander, J., and Bodenschatz, E. (2002). Measurement of particle accelerations in fully developed turbulence. *Journal of Fluid Mechanics*, 469:121–160.

111. Voth, G. A. and Soldati, A. (2017). Anisotropic particles in turbulence. *Annual Review of Fluid Mechanics*, 49:249–276.

112. Wensink, H. H., Dunkel, J., Heidenreich, S., Drescher, K., Goldstein, R. E., Löwen, H., and Yeomans, J. M. (2012). Meso-scale turbulence in living fluids. *Proceedings of the National Academy of Sciences*, 109(36):14308–14313.

113. Westerweel, J., Elsinga, G. E., and Adrian, R. J. (2013). Particle image velocimetry for complex and turbulent flows. *Annual Review of Fluid Mechanics*, 45:409–436.

114. Wheeler, J. D., Secchi, E., Rusconi, R., and Stocker, R. (2019). Not just going with the flow: The effects of fluid flow on bacteria and plankton. *Annual Review of Cell and Developmental Biology*, 35:213–237.

115. Xia, H., Byrne, D., Falkovich, G., and Shats, M. (2011). Upscale energy transfer in thick turbulent fluid layers. *Nature Physics*, 7(4):321.

116. Xia, H., Francois, N., Faber, B., Punzmann, H., and Shats, M. (2019a). Local anisotropy of laboratory two-dimensional turbulence affects pair dispersion. *Physics of Fluids*, 31(2):025111.

117. Xia, H., Francois, N., Punzmann, H., and Shats, M. (2013). Lagrangian scale of particle dispersion in turbulence. *Nature Communications*, 4(2013).

118. Xia, H., Francois, N., Punzmann, H., and Shats, M. (2014). Taylor particle dispersion during transition to fully developed two-dimensional turbulence. *Physical Review Letters*, 112(10):104501.

119. Xia, H., Francois, N., Punzmann, H., and Shats, M. (2019b). Tunable diffusion in wave-driven two-dimensional turbulence. *Journal of Fluid Mechanics*, 865:811–830.

120. Xia, H., Punzmann, H., Falkovich, G., and Shats, M. (2008). Turbulence-condensate interaction in two dimensions. *Physical Review Letters*, 101(19):194504.

121. Xia, H., Shats, M., and Falkovich, G. (2009). Spectrally condensed turbulence in thin layers. *Physics of Fluids*, 21(12):125101.

122. Xu, H. and Bodenschatz, E. (2008). Motion of inertial particles with size larger than kolmogorov scale in turbulent flows. *Physica D: Nonlinear Phenomena*, 237(14-17):2095–2100.

123. Xu, H., Pumir, A., Falkovich, G., Bodenschatz, E., Shats, M., Xia, H., Francois, N., and Boffetta, G. (2014). Flight–crash events in turbulence. *Proceedings of the National Academy of Sciences*, 111(21):7558–7563.

124. Yang, J., Davoodianidalik, M., Xia, H., Punzmann, H., Shats, M., and Francois, N. (2019a). Passive propulsion in turbulent flows. *Physical Review Fluids*, 4(10):104608.

125. Yang, J., Francois, N., Punzmann, H., Shats, M., and Xia, H. (2019b). Diffusion of ellipsoids in laboratory two-dimensional turbulent flow. *Physics of Fluids*, 31(8):085116.

126. Yang, O., Peng, Y., Liu, Z., Tang, C., Xu, X., and Cheng, X. (2016). Dynamics of ellipsoidal tracers in swimming algal suspensions. *Physical Review E*, 94(4):042601.

127. Zhao, L. and Andersson, H. I. (2016). Why spheroids orient preferentially in near-wall turbulence. *Journal of Fluid Mechanics*, 807:221–234.

128. Zheng, Z. and Han, Y. (2010). Self-diffusion in two-dimensional hard ellipsoid suspensions. *The Journal of Chemical Physics*, 133(12):124509.

129. Zimmermann, R., Gasteuil, Y., Bourgoin, M., Volk, R., Pumir, A., and Pinton, J.-F. (2011). Rotational intermittency and turbulence induced lift experienced by large particles in a turbulent flow. *Physical Review Letters*, 106(15):154501.

130. Zwanzig, R. (2001). *Nonequilibrium statistical mechanics*. Oxford, United Kingdom, Oxford University Press.